Impurity Production and Transport in the Prototype Material Plasma Exposure eXperiment

A Dissertation Presented for the

Doctor of Philosophy

Degree

The University of Tennessee, Knoxville

Clyde Joshua Beers

December 2021

© by Clyde Joshua Beers, 2021
All Rights Reserved.

This dissertation is dedicated to my Lord and Savior Jesus Christ for through Him all things are possible, my parents Clyde and Sue, my brother Matthew, and my loving wife Brianne.

Acknowledgments

It really does take a village to raise a child. This dissertation would not be possible without the help of some great people.

Thank you to Gwen Shaw for taking me under her wing when I first started. Her many hours with me and willingness to always check my MATLAB scripts for problems has benefited me substantially. Gwen and her husband, Mark, have been great friends to my wife and I outside of work also. Always a fun couple to be with.

Thank you to my peers Juan Caneses, Elizabeth Lindquist, Nischal Kafle Pawel Piotrowicz, and Holly Ray for our many hours being together during Proto-MPEX operations. They have both taught me a lot about the machine with their prior experimental knowledge on how to run it and been a shoulder to lean on in hard times. Control area conversations have made the days go by more smoothly and often offered hope when the data was questionable.

Thank you to the staff of ORNL's Fusion Energy Division: Ted Biewer, Tim Bigelow, John Caughman, Ralph Isler, Rick Goulding, Elijah Martin, and Zeke Unterberg for always being willing to offer their time and expertise. They have remarkably sped up the learning curve that I had entering a new subject area.

Thank you to Cornwall Lau and Tim Younkin for being patient with me and always providing modeling support when I knew little initially about the codes. This work wouldn't have been possible without them.

Thank you to my ORNL mentor Juergen Rapp for his vast knowledge in the field, his patience (which I know I've tried at times), and always having me look at the bigger picture. His guidance has been invaluable to me during this process. The funding allotted to me for my work would not have been possible without him and for this I am grateful.

Thank you to my advisor Steve Zinkle for being an anchor in this work. He has always been the stable resource to confer with and a voice of reason. His questioning personality always lead me to perform better data analysis and look for the underlying causes. He has always been a guide for me throughout this process.

Thank you to my parents Clyde and Sue and my brother Matthew for always supporting me and being someone I can call weekly with updates. I would not be where I am without them and I wish my Dad was here to see me finish this chapter in my life. I'm sure he would be smiling ear to ear.

Thank you to thank my wife, Brianne, for being in this process with me all the way. We have had to be pillars for each other during our schooling and have both grown so much from it. I am thankful for everyday with you.

Lastly, but mostly I would like to thank my Lord Jesus Christ. Everyday he gives me strength to carry on in this world of hardships. I am excited to see what he has in-store for me next.

Abstract

The Prototype Material Plasma Exposure eXperiment (Proto-MPEX) is a linear pulse plasma device at Oak Ridge National Laboratory with the purpose of doing the research and development for the heating concepts on the planned full MPEX device. The goal of MPEX is to perform material studies at fusion relevant conditions. To understand the conditions at the material target for performing plasma-material interaction studies the ion temperature and density, the electron temperature and density, and the particle flux and fluence must be known. Impurities within Proto-MPEX can alter the desired conditions at the material target and need to be understood for PMI studies to come in MPEX. This dissertation aims to quantify the target conditions, the impurity generation location and quantities, and the impurity transport within Proto-MPEX.

The radio-frequency (RF) helicon antenna used as the ionization source on Proto-MPEX creates a rectified RF sheath on the aluminum nitride ceramic RF window that is the vacuum boundary for the helicon. Experiments on Proto-MPEX revealed Al and O impurities on target which were found to come from the helicon window. Experiments with capacitive probe measurements showed the start-up low density phase of the plasma pulse contributing to a high RF sheath potential leading to enhanced sputtering. Fluence scans also showed that more impurities made their way to the target from the beginning of the pulse but the higher density steady state time period of the pulse was not negligible. The impurities were found to be centrally peaked in the plasma core following classical radial convection. Electron cyclotron heating was found to reduce the impurities on the target due to temperature screening and introducing Kr gas to the plasma further reduced the impurities on the target by sputtering deposited material.

A dielectric layer within a COMSOL simulation was used to model the RF sheath and get the 3D mapping of the sheath potentials for the start-up and steady state time periods of the plasma pulse. The potentials were found to be high enough to give ions impacting the helicon window more energy than the displacement threshold needed for physical sputtering of the helicon window. To track the window material that becomes impurities and is transported through Proto-MPEX a Global Impurity TRansport (GITR) simulation was performed. The impurity deposition profiles on the helicon window and at the target were obtained and were found to have good agreement with experiments.

Table of Contents

1 Introduction **1**

1.1 Growing Energy Demands 1

1.2 Fusion Energy 1

1.3 Material Challenges 6

1.4 This Work 8

2 Background **9**

2.1 Plasma Facing Components 9

2.1.1 Reactor Conditions 9

2.2 Plasma Material Interactions 10

2.2.1 Plasma pre-sheath and sheath 10

2.2.2 Physical Erosion 14

2.2.3 Chemical erosion 17

2.3 Plasma Transport 21

2.4 Impurity Transport 27

3 Experimental Set-up **29**

3.1 Proto-MPEX 29

3.1.1 Linear Plasma Device - MPEX 29

3.1.2 Proto-MPEX for R&D of MPEX 31

3.2 Proto-MPEX's Geometry 31

3.2.1 Material Targets of Proto-MPEX 35

3.2.2 Material Analysis and Particle Probe on Proto-MPEX 37

3.3 Proto-MPEX Diagnostics . . . 44
3.3.1 Double Langmuir Probes . . . 44
3.3.2 Mach Probe . . . 45
3.3.3 Capacitive Probe . . . 45
3.3.4 Thomson Scattering . . . 45
3.3.5 Visible Spectroscopy . . . 46
3.3.6 Infrared Camera Measurements . . . 47
3.4 Proto-MPEX's Operating Space . . . 48
3.4.1 Electron Density and Temperature . . . 48
3.4.2 Ion Flux . . . 48
3.4.3 Ion Temperature . . . 50
3.4.4 Heat Fluxes and Target Temperature . . . 52
3.5 Surface Characterization Diagnostics . . . 53
3.5.1 Profilometry . . . 53
3.5.2 Scanning Electron Microscopes . . . 53
3.5.3 X-ray Photoelectron spectroscopy . . . 54

4 Experimental Characterization of Impurity Generation, Transport, and Deposition in Proto-MPEX 55

4.1 Proto-MPEX Impurity Deposition on Target Observations . . . 55
4.1.1 W coated Mo Exposure . . . 57
4.1.2 Helicon Window Observations . . . 60
4.1.3 Pure W Samples . . . 60
4.2 Impurity Production Location . . . 60
4.2.1 Helicon Region . . . 60
4.3 Experiments on Impurity Source Characterization . . . 70
4.3.1 Temporal Evolution . . . 70
4.3.2 Proto-MPEX Baking . . . 72
4.3.3 ECH and Krypton Gas Addition and Tilted Target . . . 76
4.4 ICH Window Impurity Generation, Transport, and Deposition . . . 79

5 Helicon Erosion and Redeposition Modeling **81**

5.1 Model Overview . . . 81

5.2 COMSOL Model . . . 82

5.3 Sheath Model . . . 88

5.3.1 COMSOL and Sheath Model Coupling . . . 92

5.3.2 Mesh Study . . . 96

5.3.3 Role of Power on Sheath Potential . . . 99

5.3.4 Role of Density on Sheath Potential . . . 99

5.4 GITR Model . . . 99

5.4.1 COMSOL and GITR Coupling . . . 105

5.4.2 GITR Mesh and Particle Scan . . . 107

5.4.3 Role of Impact Angle on Sputtering Yield . . . 114

5.4.4 Role of Mach Number on Impurity Transport . . . 114

5.4.5 Role of Oxygen on Experiments . . . 114

5.5 Full Device GITR Model . . . 117

6 Discussion and Conclusions **131**

6.1 Impurity Characterization . . . 132

6.1.1 Helicon Window Material . . . 132

6.1.2 Pulsed Operations . . . 133

6.1.3 Density and Temperature Sensitivity . . . 134

6.1.4 Limiter Operations . . . 135

6.1.5 Role of Oxygen Content . . . 135

6.1.6 Baking Operations . . . 135

6.2 Target Impurity Flux . . . 136

6.2.1 Helicon Window Deposition Profile . . . 139

6.2.2 Radial Scan . . . 141

6.2.3 Role of Temperature Screening . . . 143

6.2.4 Exposures with Kr . . . 143

6.3 Conclusions . . . 143

6.4 Implications for MPEX 146
6.5 Future Work 147

Bibliography **149**

Appendix **163**

A McPherson Spectrometer Calibrations 164
B Fiber Optic Periscope Alignment 166
C MAPP Scope of Work 167
D COMSOL and Sheath Model Validation 168

Vita **172**

List of Tables

3.1 Proto-MPEX Operational Space 49

4.1 Mo exposure EDS results 56
4.2 Sample conditions for the limiting location experiment 63
4.3 Sample conditions for exposures with the Si_3N_4 window 66
4.4 Sample conditions for the shutter experiment 73
4.5 Sample conditions for the ECH+Kr experiment 77
4.6 Sample conditions for the ICH impurity experiment 80

5.1 COMSOL Mesh Scan 98

6.1 The Al ion impurity flux and fluence at the target for the modeled conditions. 138
6.2 The Al ion impurity flux and fluence at the target with O as the sputtering species for the modeled conditions. 138

List of Figures

1.1 World energy consumption by energy source from 1999-2015 and energy consumption projection from 2015-2040. 2
1.2 Average mass per nucleon versus atomic mass number, A. 2
1.3 Reaction rates for the three main fusion candidates. 4
1.4 Deisgn of ITER and the W divertor cassettes. 5

2.1 ITER divertor cassette design 11
2.2 Cartoon of the two point model 13
2.3 Cartoon of the plasma sheath 13
2.4 Depiction of the angle between the **B** and the surface normal 15
2.5 Redeposition Mechanisms 18
2.6 C, Si, and SiC mass spectra during chemical erosion 20
2.7 Si chemical erosion yield dependence on temperature 20

3.1 MPEX Design 30
3.2 Proto-MPEX 12 magnet coils configuration 32
3.3 Proto-MPEX 13-magnet coils configuration 32
3.4 Proto-MPEX helicon 34
3.5 Internal ICH antenna 36
3.6 External ICH antenna 36
3.7 MAPP CAD file with labeled ports 38
3.8 MAPP CAD cross-section with port angles 40
3.9 MAPP on Proto-MPEX and Target Holder 41
3.10 Target Designs for use in MAPP 43

3.11 Shielding Pieces for MAPP 43

4.1 Exposed Mo sample for impurity collection and locations of EDS 56
4.2 Exposed W coated Mo and locations of SEM analysis 59
4.3 SEM images of the W coated Mo sample 59
4.4 The AlN helicon window with depositions 61
4.5 Limiting locations in the Proto-MPEX helicon region 61
4.6 Exposed W sample and XPS region 63
4.7 XPS data from limiting locations experiment 64
4.8 XPS data from the Si_3N_4 helicon window 66
4.9 Exposed AlN helicon window pattern 68
4.10 XPS data from the AlN helicon window 69
4.11 Profilometry data from the AlN helicon window 69
4.12 Capacitive probe RF potential 71
4.13 Fluence scan impurity thickness result 71
4.14 XPS data from the target shutter experiment 74
4.15 Impurity thickness pre and post-baking 75
4.16 XPS data from the ECH+Kr shutter experiment 78
4.17 XPS data from the ICH experiment 80

5.1 Modeling Flow Chart 83
5.2 Proto-MPEX modeled magnetic profile 84
5.3 Modeled Helicon Geometry 84
5.4 Helicon Antenna Model 85
5.5 COMSOL and Sheath Layer Mesh 87
5.6 Sheath model diagram 93
5.7 Low-Density sheath model convergence 95
5.8 High-Density sheath model convergence 95
5.9 Electrical Field on the Helicon Window 97
5.10 Unrolled converged electric field for the four modeled cases 98
5.11 COMSOL low power results 100

5.12 COMSOL increased density results . . . 100
5.13 F-TRIDYN D onto Al sputtering yields . . . 101
5.14 Electron density and temperature profiles used in GITR . . . 104
5.15 F-TRIDYN Al onto Al sputtering yields . . . 106
5.16 Flow chart for the GITR simulations . . . 106
5.17 Low-density unmagnetized GITR results . . . 108
5.18 Low-density magnetized GITR results . . . 109
5.19 High-density unmagnetized GITR results . . . 110
5.20 High-density magnetized GITR results . . . 111
5.21 GITR particle scan results . . . 112
5.22 GITR mesh scan results . . . 113
5.23 Role of impact angle . . . 115
5.24 Mach number GITR scan . . . 116
5.25 F-TRIDYN O onto Al sputtering yields . . . 118
5.26 Axial Mach number profile used in the GITR full device simulations . . . 119
5.27 Axial particle distribution . . . 121
5.28 Particle deposition locations . . . 122
5.29 Low-density unmagnetized full device GITR results . . . 123
5.30 Low-density magnetized full device GITR results . . . 124
5.31 High-density unmagnetized full device GITR results . . . 125
5.32 High-density magnetized full device GITR results . . . 126
5.33 Oxygen low-density unmagnetized full device GITR results . . . 127
5.34 Oxygen low-density magnetized full device GITR results . . . 128
5.35 Oxygen high-density unmagnetized full device GITR results . . . 129
5.36 Oxygen high-density magnetized full device GITR results . . . 130

6.1 (a) The helicon window deposition pattern with helicon overlay in magenta, (b) the low-density magnetized case's net deposition with helicon pattern shown in dark blue, and (c) the high-density magnetized case's net deposition with helicon pattern shown in dark blue. The points X (deposition), Y (no deposition), and Z (location between the feed and ground connections on the helicon antenna) indicate regions from the model that match the pattern on the helicon window. 140
6.2 The normalized impurity layer thickness with the Si_3N_4 helicon window at the normalized locations for the plasma center, one cm off-axis, and two cm off-axis along with the normalized GITR radial ionized Al impurity density 1 cm in front of the target location. 142
6.3 Classical Impurity Convection Velocity 144
4 MAPP Scope of Work 167
5 The $Im(E_{\|}$ plots for (a) the Kohno 2017 paper data (reproduced from [90]) and (b) the COMSOL simulation within this work. 169
6 The maximum voltage in the layer for the $1kA/m$ case for the Kohno 2017 Fits, the Myra 2017 Fits, and the data from the Kohno 2017 work. 170
7 The maximum voltage in the layer for the $3kA/m$ case for the Kohno 2017 Fits, the Myra 2017 Fits, and the data from the Kohno 2017 work. 170
8 The maximum real and imaginary components of the sheath impedance, $\hat{z}$, in the layer for $1kA/m$ case for the Kohno 2017 Fits, the Myra 2017 Fits, and the data from the Kohno 2017 work. 171
9 The maximum real and imaginary components of the sheath impedance, $\hat{z}$, in the layer for $3kA/m$ case for the Kohno 2017 Fits, the Myra 2017 Fits, and the data from the Kohno 2017 work. 171

Chapter 1

Introduction

1.1 Growing Energy Demands

Energy demand is tied to a nation's economy and as more countries are become wealthier the world energy demand grows [1]. There has been a steady rise in the total world energy usage and as of 2015 it is expected to increase by 28% by 2040 [2]. Figure 1.1 shows this projected increase and the breakdown of the expected energy sources to meet this growth. Fossil fuels are the largest contributor to the energy production, but this is a large contributor to the rise in greenhouse gasses. Carbon dioxide, one of the leading greenhouse gasses, is currently at an all-time high [3]. This carbon dioxide increase is expected to cause a world temperature rise leading to an increase in severe weather. By switching to greener energy supplies the carbon footprint can be greatly reduced. Many forms of green energy exist and are being improved through additional research: hydro, wind, solar, and nuclear, namely nuclear fusion.

1.2 Fusion Energy

Nuclear fusion energy (fusion) is the ideal green energy with the potential to have clean and safe production with an unlimited supply. This energy source can also be available for everyone due to the availability of the fuel being hydrogen isotopes. Figure 1.2 shows the driver behind fusion energy with the greater the average mass per nucleon the higher the

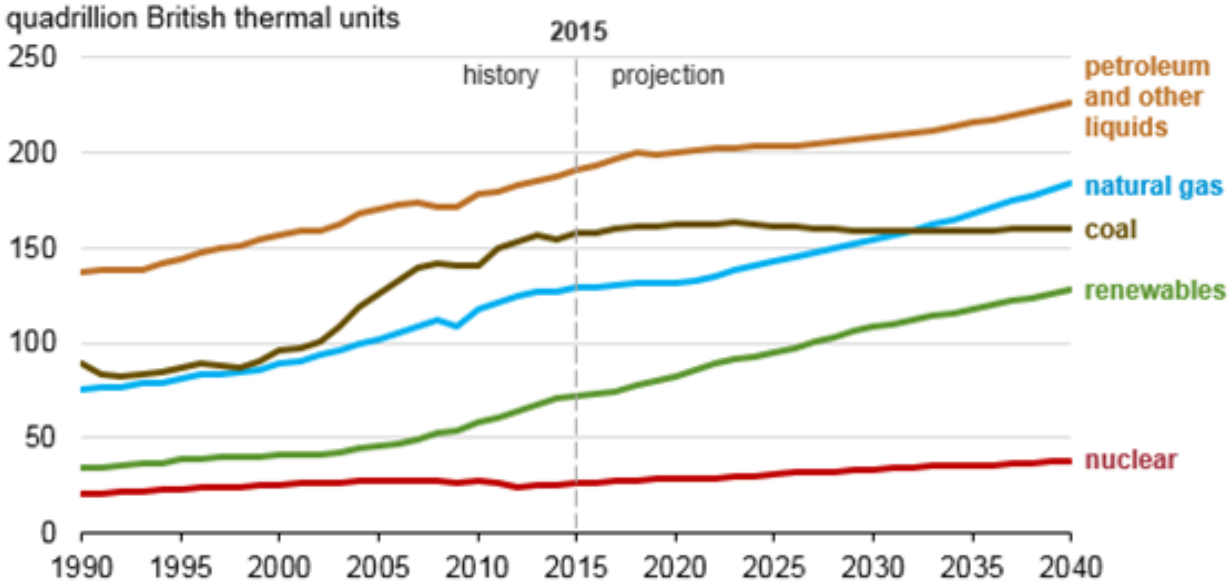


Figure 1.1: World energy consumption by energy source from 1999-2015 and energy consumption projection from 2015-2040. Reproduced from [2].

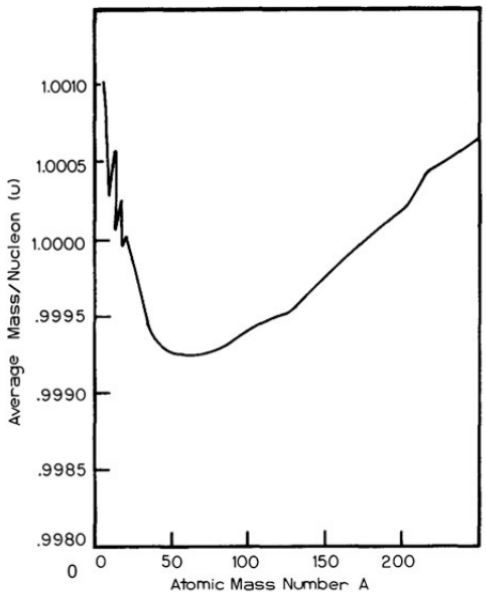


Figure 1.2: Average mass per nucleon versus atomic mass number A where the minimum is around Fe (A=56) and the maximum is at H (A=1). Reproduced from [4].

energy that is released from the reaction which comes from $E = \Delta mc^2$. The energy released from nuclear fission with uranium (A=235) is going to be less than fusion of hydrogen (A=1) leading to higher energy output from fusion over fission.

To produce fusion takes a huge engineering feat that has been ongoing for many years. One can image the difficulty of containing the sun in a box. The high temperatures required to enable the fusion prcoess lead to a fully ionized hydrogen plasma with temperatures of millions of degrees. While this seems scary or impossible, on Earth, magnets can hold the plasma (confinement). The electromagnetic force behind magnets is stronger than that of the gravitational force which the Sun uses for fusion. Many donut-like shaped devices (tokamaks and stellarators) are currently using magnetic confinement to run ^2H (deuterium, D) plasmas to study how close to the fusion condition they can reach. The ^2H - ^3H (tritium, T) (D-T) reaction is the reaction of choice due to its higher cross-section rates at lower energies as seen in Figure 1.3. D-T will be used for fusion power plants but due to the similarities between the hydrogen isotopes the physics for getting to the D-T reaction can be studied with pure deuterium plasmas. Tritium is also a short-lived radioactive isotope, so working with deuterium is easier for many facilities. The D-T reactions produces ^4He (helium, He), a neutron (n), and energy in the reaction:

$$^2H +^3 H =^4 He + n + 17.6MeV \tag{1.1}$$

where the neutron gets 14.1 MeV of the energy.

The next device that is currently expected to be completed in 2025 is ITER. ITER is a tokamak style device that is a joint experiment between China, the European Union, India, Japan, Korea, Russia and the United States. The top part of Figure 1.4 shows ITER. ITER is expected to produce fusion power and demonstrate the technologies are in place for fusion power. After ITER the Demonstration Power Plant (DEMO) is to show that the fusion power plant can provide electricity to the grid.

ITER will need to be able to exhaust the fusion ash, He, in the exhaust system. This exhaust is needed because as the fusion ash moves through the device, they move outward and eventually leave the plasma. To control where these particles are exhausted the magnetic

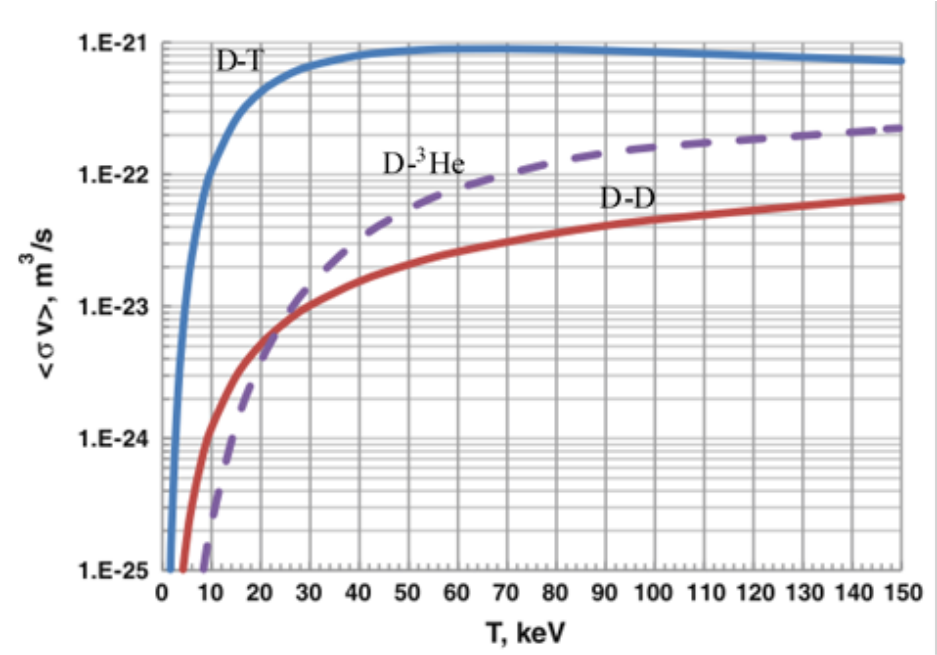


Figure 1.3: Reaction rates for the three main fusion candidates; D-D, D-T, and D-^{3}He. Reproduced from [4].

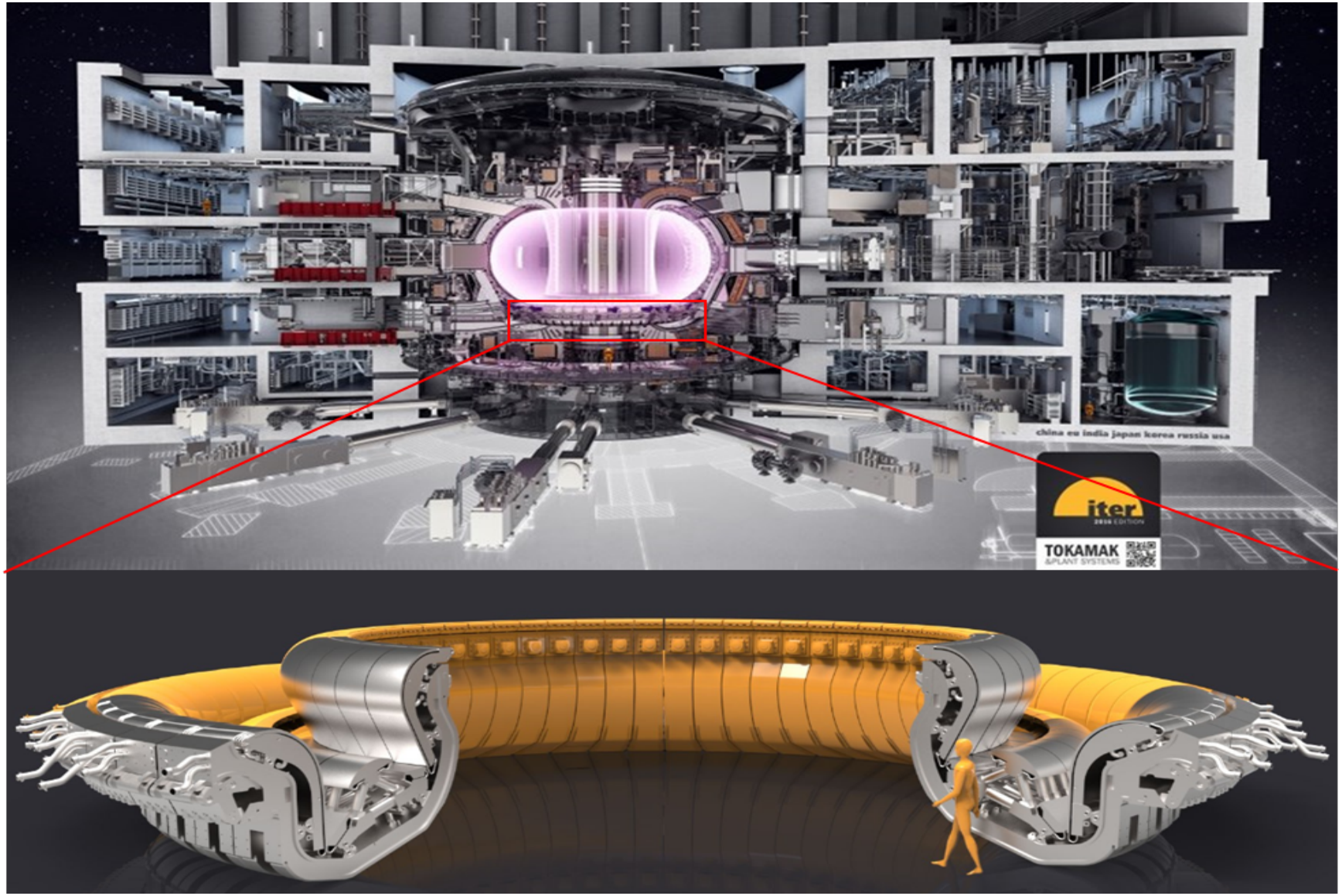


Figure 1.4: Deisgn of ITER and the W divertor cassettes. Reproduced from [5].

fields in the device direct them towards a divertor. The divertor for ITER will be tungsten (W) cassettes that form a ring at the base of the device. The bottom of Figure 1.4 shows the divertor concept for ITER. Thinking back to the Sun in a box idea, being able to handle the escaped particle and heat flux to the "box" is one of the main engineering challenges that fusion faces.

1.3 Material Challenges

The plasma facing component(s) (PFC(s)) are the materials that will directly receive the heat and particle flux (ions and electrons) that escapes the plasma confinement. In ITER the PFCs will consist of the divertor and the first wall which consist of many components (breeding blankets, beam and particle injectors, cyclotron heating launchers, mirrors for diagnostics, and more). The divertor lifetime before needing replaced is a large part in making fusion energy economic. Material choices have many factors that need to be considered. The materials used for the PFC will need to be non-magnetic due to being inside a magnetic field as well as need to be radiation resistant due to the 14.1 MeV neutrons. Since neutrons do not have a charge the magnetic fields will not hold them and thus the entirety of the PFCs will have neutron damage which leads to needing materials that will have radiation resistance (maintaining desired material properties under radiation exposure). Neutron irradiation will also lead to element and isotope transmutation so the materials will need to have the absence of long-lived radioactive transmutation particles to reduce the total plant radioactivity. Nuclear fission cannot avoid this issue due to the fuel used having very long-lived radioactive particles being produced as the fuel is used. Fusion produces He as T is used up, as shown in Eq. 1.1, which is not radioactive but to maintain fusion, lithium (Li) breeding blankets will be used to create tritium. On top of the neutron damage, the high heat and particle flux can lead to sputtering, surface modification, and melting. All of these surface effects can produce freed material that can locally or globally redeposit. Sputtered material may also enter the plasma and with enough concentration can lead to, in the worst case, the plasma being cooled by radiation and a loss of the fusion reaction. Higher atomic number (Z) elements are worse than smaller ones because of the number of electrons

available to take energy from the plasma. Tungsten was chosen as ITER's divertor because of its low sputtering yield, high melting temperature (3695 K), and low tritium retention. Minimizing the number of high-Z atoms in the plasma is an important materials problem to balance with plasma performance.

Tritium retention is a concern for carbon based PFCs because of the total allowable tritium inventory. Carbon based PFCs have been used for many years in tokamaks (some still used it) because of its high working temperature, low-Z status, and no surface melting. When the T retention properties were studied in carbon it was found that they were too high to be acceptable [6]. Graphite components also have an increased sputtering rate when exposed to lower temperature ions due to chemical sputtering which can be a problem for component lifetime. An alternative to pure graphite is silicon carbide (SiC) which was found to have far less tritium retention and have desirable structural properties [7]. Tungsten also has a much lower tritium retention but it is still a high-Z material that can lead to radiative cooling while carbon based PFCs that enter the plasma cannot allow the effective Z value (Z_{eff}) to be above 1.7, else the plasma is diluted [8]. The divertor's shape can help to eliminate some W reaching the main plasma but plasma instabilities such as edge localized modes (ELMs) can release a large amount of power to the PFCs. The heat and particle flux increase causes an increase in surface modification which can lead to an increase in W released to the plasma. The surface modification of W is still an ongoing area of research.

Linear devices have an easier time than tokamaks and stellarators at doing materials research. In tokamaks and stellarators, a large amount of power is injected which results in a small fraction of it on the divertor (a good thing for reactors) but linear devices can have a higher fraction of the input power going to the target. Linear devices also typically have easier diagnostic access. Linear devices are thus constructed to do plasma material interaction (PMI) studies. These devices use far less power (kW vs. MW) to study the material changes under plasma exposure in an accelerated manner. Linear devices also offer a wider range of divertor plasma condition variability. They can alter the ion flux, ion energy, plasma electron density and temperature, and the heat flux to the target. This variability leads to faster turnaround for material studies. In a linear plasma device the

plasma transport is akin to transport within the scrape-off layer of a tokamak which also lends itself to plasma and impurity transport studies [9].

To study the fusion reactor material problems the Material Plasma Exposure eXperiment (MPEX) is planned. MPEX will be a steady state linear plasma device that will exposure *a-priori* neutron irradiated materials to fusion relevant plasmas.

1.4 This Work

The Prototype Material Plasma Exposure eXperiment (Proto-MPEX) is a linear device at Oak Ridge National Laboratory (ORNL) that is performing the research and development for the planned MPEX device. All experiments for this work are performed using Proto-MPEX. The ITER conditions, expected material behavior, and plasma transport is the focus of Chapter 2. The geometry and conditions of Proto-MPEX are discussed in detail in Chapter 3. First experiments and impurity findings are discussed in Chapter 4. Modeling of the impurity movement within Proto-MPEx is given in Chapter 5. Chapter 6 gives a comparison of the modeling and experiments of the work, the conclusions, and future work.

Chapter 2

Background

2.1 Plasma Facing Components

2.1.1 Reactor Conditions

While the hope is to keep particles confined in the plasma some will inevitably escape to the scrape-off layer and will be purposely guided to the divertor. As plasma parameters change, so too will the particles entering the scrape-off layer. The divertor of a tokamak or target in a linear device will be subject to a wide range of particle fluxes based on the temperature and density. In a tokamak a high particle flux to the divertor of up to $10^{24}\ m^{-2}s^{-1}$ will be present [10]. To reduce the heat and particle flux to the divertor radiation cooling is used which can lead to the plasma current to the PFC being dramatically reduced (detachment). The semi-detached divertor in fusion devices are expected to have ion energies of a few to tens of eV. There will also be MeV neutron fluxes on the order of $10^{18}\ m^{-2}s^{-1}$ to the PFCs [11].

Much of the first wall will be the Be first wall panels, which is only rated to have power handling capabilities of $2 - 4.7\ MWm^{-2}$ [12]. The original plan to use W and a carbon fiber composite (CFC) for the divertor material [13] has changed to an entire W director due to tritium inventory issues with CFCs [14]. Tungsten has the highest melting point of any metal at 3695 K and CFCs are high operating temperature materials. Tungsten monoblocks with Cu interfaces to CuCrZr coolant channels have been chosen as the whole ITER divertor

material. These monoblocks are rated for 10 MWm^{-2} in steady state and for slow transients on the order of up to seconds for 20 MWm^{-2} [15]. Figure 2.1 shows the ITER divertor design and the individual W monoblocks that will be used. These heat flux design values are of importance as to avoid melting of the tungsten. However, if the plasma temporarily attaches to the divertor then a peak perpendicular power flux of 40 $MW\ m^{-2}$ can be delivered, which can only be sustained for a few seconds before melting or heat reaching the coolant tubes leading to possible coolant leaks [13]. Short transient events have to deliver power loads at or above 50 $MWm^{-2}s^{1/2}$ for W and 28 $MWm^{-2}s^{1/2}$ for Be to melt without cooling [16].

The edge localized mode(s) (ELM(s)), transient events due to plasma instabilities, can lead to an increased particle (1-2 orders of magnitude) and heat flux (several orders of magnitude) being exposed to the first wall and divertor. ELMs can give a few GW m^{-2} for sub-ms time scales at a frequency of 1 Hz which can lead to large impurity production and/or melting [11]. The impurity release into the plasma can lead to plasma radiation cooling resulting in a loss of fusion or further increased sputtering rates from self-sputtering lead to a reduction in the lifetime of the PFCs.

2.2 Plasma Material Interactions

2.2.1 Plasma pre-sheath and sheath

When a plasmas has an edge boundary region near a material surface a plasma sheath will form. The sheath is not quasineutral due to the wall taking more electrons than ions which means it creates a potential which repels electrons and accelerates ions to the surface. The sheath controlling the flow of ions to the surface directly affects the main plasma density and temperature and the heat flux to the wall [17, 18].

Particles that enter the scrape-off layer (an open plasma field line that ends at the wall or target for a linear device) will bring particles towards the sheath. The two-point model is the simplest fluid model which can be used with experimental or simulation results to get a relationship between the upstream plasma (plasma closer to the ionization source) and those at the target or divertor. The equations for the two-point model are:

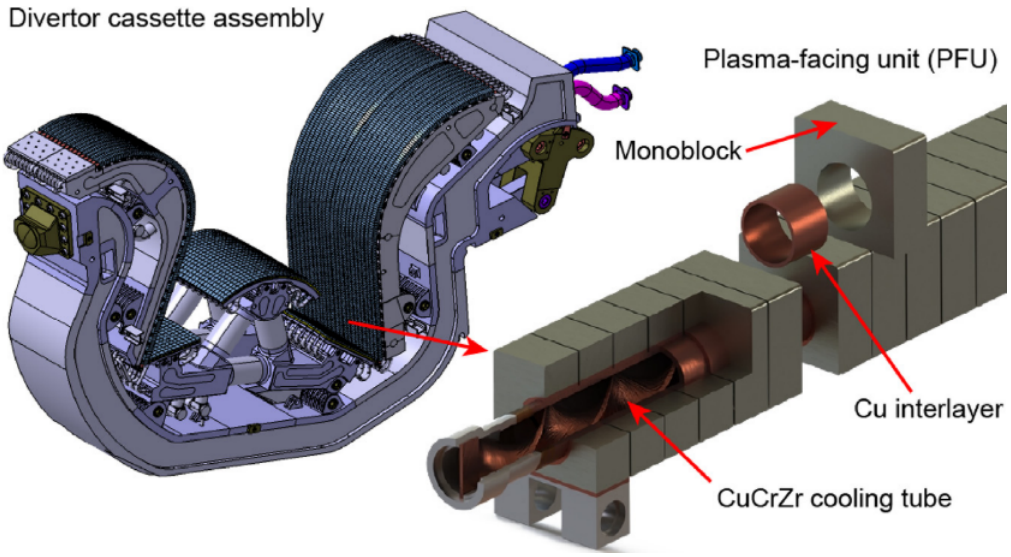


Figure 2.1: CAD image of the ITER divertor cassette assembly which is comprised of W PFCs in the form of monoblocks that have CuCrZr twisted tape designed cooling channels running through them. Reproduced from [15].

$$2 * n_t * T_t = n_u * T_u \tag{2.1}$$

$$T_u^{\frac{7}{2}} = T_t^{\frac{7}{2}} + \frac{7 * q_{\parallel} * L}{2 * \kappa_{0e}} \tag{2.2}$$

$$q_{\parallel} = \gamma * n_t * T_t * c_{st} \tag{2.3}$$

where n_t is the density at the target, n_u is the density upstream, T_t is the target temperature, T_u is the upstream temperature, L is the length of the system, k_{0e} is the electron parallel conductivity coefficient, γ is the sheath heat transmission coefficient, $q_{\parallel}$ is the parallel heat flux, and c_{st} is the sound speed of particles at the target (see Equation 2.16 for more on the sound speed) [9]. Figure 2.2 shows a simple scrape-off layer which has the main plasma enter it upstream and flow towards the target.

The particle density in front of the target can also be obtained from the two-point model:

$$n_t = \frac{n_u^3}{q_{\parallel}^2} * \left(\frac{7 * q_{\parallel} * L}{2 * k_{0e}}\right)^{6/7} * \frac{\gamma^2 * e^3}{4 * m_i} \tag{2.4}$$

where e is the charge of an electron and m_i is the mass of the ion [9].

The sheath is described in two sections; the Chodura pre-sheath, also called the magnetic pre-sheath (MPS), and the Debye sheath, which collectively is simply called the sheath. Figure 2.3 shows the regions of the sheath with a cartoon of the potential's change within those regions. In this potential change region, the electrons are repelled and the ion flux is what makes its way to the wall. One thing that defines the edge of the sheath is the Bohm criterion which is the ions enter the sheath with a drift kinetic energy that is higher than their thermal energy. Equation 2.5 gives the relationship for the ion velocity at the sheath edge which is the Bohm speed:

$$V_{Bohm} \geq \sqrt{\frac{k_b * T_e}{m_i}} \tag{2.5}$$

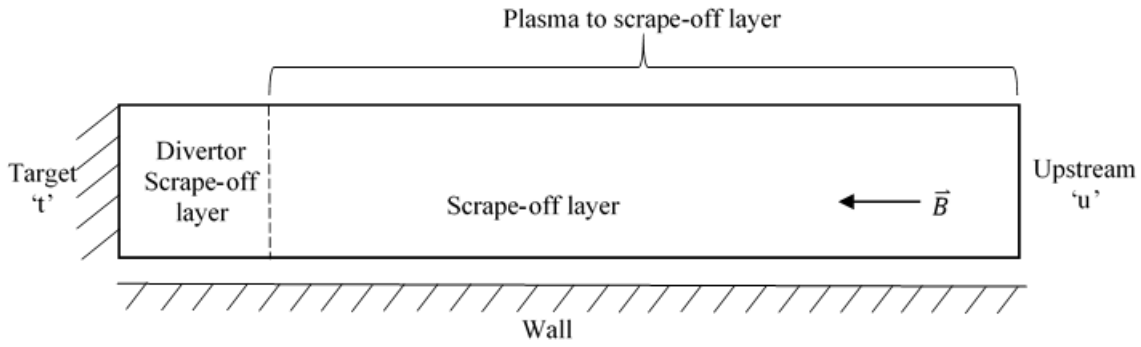


Figure 2.2: Cartoon showing the two point model where the plasma enters the scrape-off layer upstream and flows to the target.

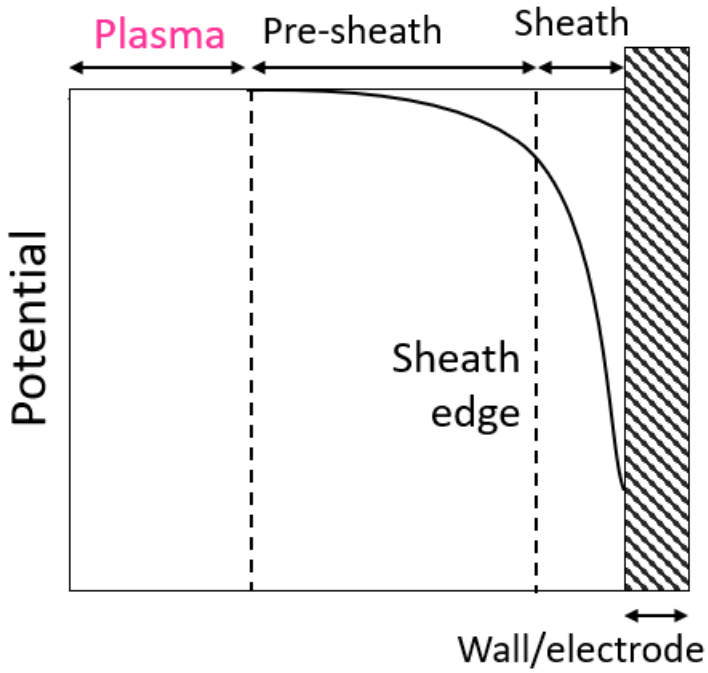


Figure 2.3: Cartoon showing the potential change from the plasma to the pre-sheath and from the pre-sheath to the sheath edge which then increases in potential drop until the wall.

where V_{Bohm} is the Bohm velocity, k_b is the Boltzmann constant, T_e is the electron temperature, and m_i is the mass of the ion.

The MPS thickness is given by:

$$L_{PS} = \sqrt{6} * \frac{c_s}{\omega_{ci}} * sin(\Psi) \tag{2.6}$$

where c_s is the plasma sound speed, ω_{ci} is the cyclotron frequency of the ion, and Ψ is the angle of between the incoming magnetic field to the surface and the surface normal [9]. Figure 2.4 shows a cartoon of the angle Ψ. This leads to a large pre-sheath as glancing magnetic angles. The potential of the MPS is given by:

$$\frac{eV_{MPS}}{k_b * T_e} = \ln cos(\Psi) \tag{2.7}$$

The Debye sheath thickness is given by:

$$L_{DS} = \sqrt{\frac{\epsilon_0 * T_e}{N_e * e^2}} \tag{2.8}$$

where ϵ_0 is the permittivity of free space, N_e is the electron density, and e is the elementary charge [19]. The Debye sheath thickness is typically very thin for edge conditions in plasma devices. The sheath electric field is:

$$E_{sheath} = \frac{k_b * T_e}{e * L_{DS}} \tag{2.9}$$

where L_{DS} is the Debye sheath thickness. This gives rise to the Bohm criterion, where the velocity of the ions must be greater than the plasma sound speed [9]. This is important because the sheath potential increases the energy of the ions that impact the PFCs.

2.2.2 Physical Erosion

As particles bombard the PFCs physical sputtering and erosion can occur. Only a reference to ions will be given hence forward as neutron interactions produce orders of magnitude lower surface sputtering compared to plasma ions. Physical erosion is the act

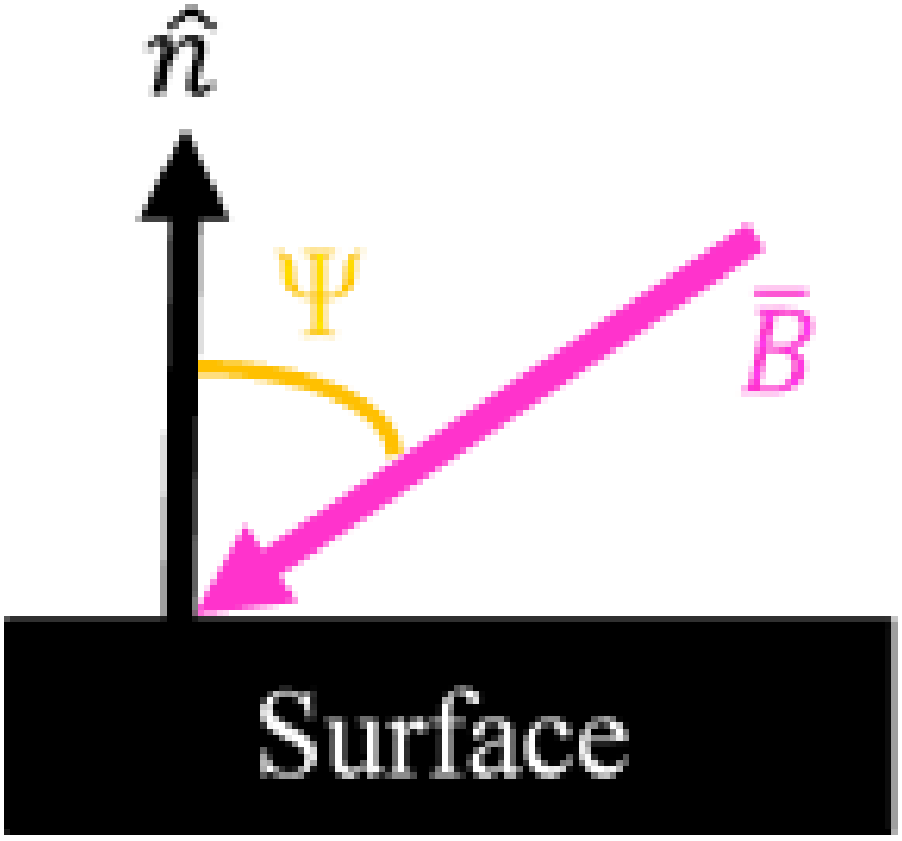


Figure 2.4: Cartoon showing the angle, Ψ, between the magnetic field, **B** and the surface normal, $\hat{n}$.

of a particle with high enough energy to physically knock other atom(s) from their lattice sites. The displacement energy, E_d, of the material is the minimum energy needed to remove an atom from its lattice site. However, surface sputtering is less than the displacement energy because less atomic bonds are present for surface atoms when compared to the bulk. The first particle that is displaced is called the primary knock-on atom (pka) and can also lead to a displacement cascade on top of knocking an atom(s) back into the scrape-off layer. The average number of times an atom has been removed from their lattice position is given in displacements per atom (dpa), where 1 dpa would mean that on average each atom has been knocked out of its lattice point one time. The size of the cascade is dependent on the incident particle's energy and the bulk material's stopping power, both electronic and nuclear. The atom species themselves, starting energy, and impact angle will determine the path of the pka and the size of the cascade. When looking at the bulk the energy that is transferred to the first pka, E_T is given by:

$$E_T = \frac{\gamma}{2}(E_{impact} - cos(\Psi)) \tag{2.10}$$

where

$$\gamma = \frac{4 * m_1 * m_2}{(m_1 * m_2)^2} \tag{2.11}$$

where γ is the transferred energy ratio, m_1 is the mass of the incoming ion, m_2 is the mass of the atom being hit, and E_i is the impact energy of the indecent particle [20]. When the angle is equal to the surface normal the maximum energy is transferred and the energy transferred decreases for glancing angles. The impact energy for a non-biased target is given by:

$$E_{impact} = 2k_bT_i \ + \ 3Zk_bT_e \tag{2.12}$$

where E_{impact} is the impact energy of the ions on the surface, T_i is the ion temperature in eV, and Z is the atomic number of the incoming particle(s) [9]. The ion impact energy for a negatively biased target is the plasma potential [V_p] minus the bias voltage [V_b] [21].

For surface atoms the sputtering rate is maximized at glancing angles [22–25]. Also for lower energy ions such as those at the divertor PFCs the ions can lose all energy due to

one collision and no cascade is formed [22]. The sputtering yields have been given by many works as a function of the masses, incoming energy, angle of incidence, sublimation energy (taken as the displacement energy needed for surface atoms), and the lattice parameters of the target material [26].

When an eroded particle is ionized close to the surface it gyrates back towards the surface which it was eroded from or if it is ionized within the MPS it is accelerated back to the surface by the sheath potential. If the ion does not complete one gyration before being redeposited on the surface this is called local redeposition. Prompt redeposition is a subset of local redeposition which is when the ion does not leave the Debye sheath before being redeposited [27]. Ions that complete at least one full gyroradius and are deposited elsewhere within the device undergo global device transport and global redeposition. It is also possible that these ions which travel globally are transported at a local or prompt location, but this is difficult to determine. The direction of the sputtered particle (either away or towards the direction of the magnetic field lines) can determine which redeposition mechanism happens along with the ionization mean free path. Figure 2.5 shows the local or global redeposition phenomena. Material that is not ionized (as could be the case in low ion energy devices) can stream as neutrals to locations within the device to appear as redeposition or to be entrained in the plasma and transported via friction forces to elsewhere within the device.

The act of particles coming off of the target surface, being re-ionized, and hitting the surface again can lead to a phenomena called recycling which increases the total flux that the target is receiving. Linear devices can make use of this recycling (conduction-limited regime) to maintain a high flux without needing additional particle flux given the upstream plasma.

2.2.3 Chemical erosion

Chemical erosion occurs when the plasma species interacts chemically with the surface leading to higher erosion rates than from physical sputtering alone. The process can occur from an incoming ion having enough energy to break a chemical bond but not enough to

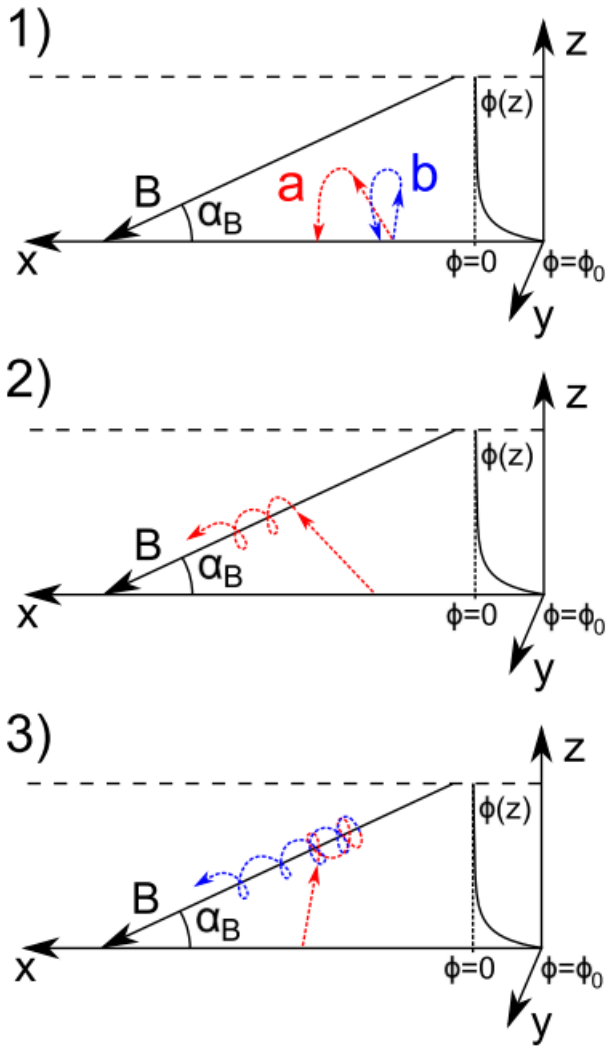


Figure 2.5: Phenomena in redeposition: 1) local redeposition which includes prompt redeposition, 2) global or long range redeposition with the particle moving along the magnetic field line before ionization, and 3) global redeposition with the particle moving initially opposite of the magnetic field line before ionization which causes it to turn around. Red is the direction of the sputtered particle and blue is the direction of the ionized particle. Reproduced from [28]

displace an atom. Another incoming ion can then more easily remove the atoms with the broken bonds. This process can occur when it is more thermodynamically favorable to form a volatile product with the incoming ion than to be bound to the surface. This effect has a dependence on sample surface temperature, ion species, ion impact energy, ion impact angle, and ion flux (derived from plasma density and temperature) [29–36]. Here Si and Al along with some of their compounds (i.e. Si_3N_4, AlN, Al_2O_3) will be the focus.

Figure 2.6 shows the mass spectra taken during 20 eV D exposures on to C, silicon (Si), and silicon carbide (SiC) for surface temperatures of 300 K, 570 K, and 300 K, respectively. The mass spectra data indicates a wide variety of processes that occur with chemical erosion and the types of compounds that are formed.

The role of surface temperature and ion impact energy on the total chemical erosion yield for D^+ of 20, 100, and 300 eV onto Si and C for reference is shown in Figure 2.7. A peak in chemical erosion yield for the 20 eV D^+ ions is seen at 350 K which falls off at higher temperatures. The yield for pure Si is also 3-10x lower than that of C. The yield increases for increasing ion impact energy, but this moves into physical sputtering at the higher ion impact energies.

Plasma etching experiments of a hydrogen plasma onto Si, SiO_2, and Si_3N_4 showed that the etch rate of Si was 30x greater than that of the SiO_2 and Si_3N_4 [37]. No incident H energy was given so reactive ion beam etching was performed using 100 eV to 1 keV H ions to understand the underlying processes of the hydrogen plasma etching experiment. By comparing the measured sputtering yield to physical sputtering yields it was found that physical sputtering alone was not the cause for the etching rate [38]. It was also found that the surface will enrich with Si as the etching process goes on. Work with H onto Si with a modulated molecular beam shows that H_2 and SiH_4 were the only reactions produces produced [39]. It was stated that H can react with SiH_2 to produce SiH_4 but only a small fraction ($\sim$ 3%) was measured. In another plasma etching experiment with CF_4 gas onto Si_3N_4 it was found that the addition of O_2 to the gas mixture increases the etch rate by up to a factor of 2 [40]. It was concluded that the N-O molecule plays an important role in Si_3N_4 etching.

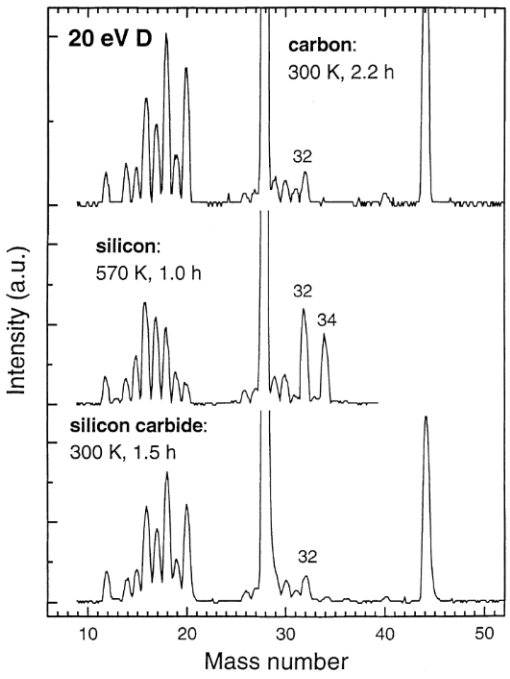


Figure 2.6: Mass spectra taken during 20 eV D exposure to a) C, b) Si, and c) SiC at the shown target surface temperature. Reproduced from [29].

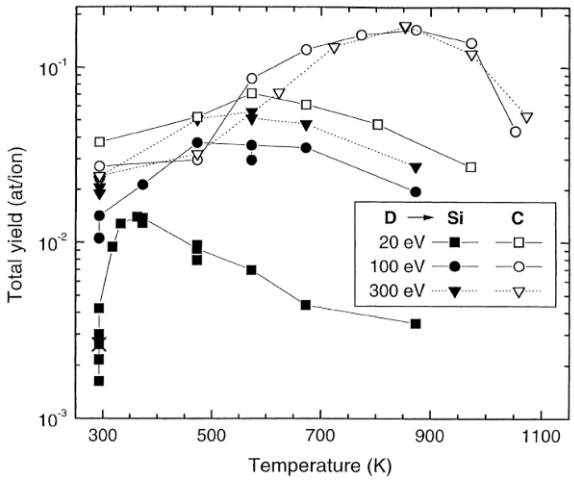


Figure 2.7: Total chemical erosion yield for D^+ ions of 20, 100, adn 300 eV onto Si and C at various surface temperatures. Reproduced from [29].

Al itself does not undergo chemical sputtering but physical sputtering while few studies of chemical erosion have been done on its compounds. Exposures of deuterium and helium plasmas onto the ceramics aluminum oxide, Al_2O_3, and aluminum nitride, AlN, have not found evidence of chemical erosion, making them viable PFCs [41]. The plasma fluxes used here were much lower than what is expected in a fusion device's divertor, so any role of chemical sputtering is expected to be further reduced.

2.3 Plasma Transport

To understand the plasma fluxes on the target the transport of the majority D ions and electrons needs to be understood. To describe the plasma transport, fluid equations will be used to describe the plasma of a single temperature that follows a group gyration motion along a magnetic field line. Kinetic equations describe an individual particle species with their own temperature and motion but only the starting details will be given here as the full kinetic approach is behind the scope of this work.

In a magnetized plasma the ions and electrons follow the magnetic field lines in a gyration motion with a gyroradius (also called the Lamor radius), r_c, and a gyrofrequency (also called the cyclotron frequency), ω_c. The Lamor radius is given by:

$$r_{cs} = \frac{v_s * T_s}{\omega_{cs}} \tag{2.13}$$

and ω_{cs} is given by:

$$\omega_{cs} = \frac{|Z * e| * B}{m_s} \tag{2.14}$$

where s denotes the species for an electron or of the ion, e is the charge, Z is the charge state of the species (always 1 for an electron), B is the magnetic field magnitude, m is the mass of the species, T_s is the species temperature, and v_c is the instantaneous charged particle velocity perpendicular to the magnetic field. The charged particle velocity is given by:

$$v_s = \sqrt{\frac{Z * k_b * T_s}{m_s}} \tag{2.15}$$

where Z is again 1 for electrons.

The plasma sound speed, c_s, comes from ion and electron oscillations in the plasma and is given by:

$$c_s = \sqrt{\frac{\gamma_e * Z_i * k_b * T_e + \gamma_i * k_b * T_i}{m_i}} \tag{2.16}$$

where γ_e is the adiabatic flow for electrons (usually set as 1 due to isothermal flow), Z_i is the charge state of the ions, γ_i is the adiabatic flow of the ions (set as 3 for 1D flow).

Each particle having the same energy gives way to the Maxwell-Boltzmann distribution, giving a spread of velocities for a plasma in thermal equilibrium. For an infinitesimal sized 3D space with velocity vector v the distribution is given by [19, 42]:

$$f(v)d_3v = (\frac{m}{2 * \pi * k_b * T_e})^{\frac{3}{2}} * e^{-\frac{m*v^2}{2*k_b*T_e}} d^3v \tag{2.17}$$

The velocity then related to the temperature yields the root mean squared (rms) thermal speed, v_{rms}, given by:

$$v_{rms} = \sqrt{\frac{3 * k_b * T}{m}} \tag{2.18}$$

The rms thermal speed is similar in form to that of the charged particle velocity but is 3x due to being 3D versus 1D [19, 42].

Assuming a two species plasma three types of collisions may occur: electron-electron, ion-ion, and electron-ion/ion-electron. However, there will always be neutral particles present in a plasma device which give rise to electron-neutral and ion-neutral collisions. These collisions are what allow the ion acoustic wave to propagate. The quasineutral plasma collision frequencies are given by [43]:

$$\nu_{ee} = n_e * \frac{e^4}{(4 * \pi * \epsilon_0)^2} * \frac{8 * \pi}{m_e^2 * v_e^3} * \ln \Lambda \tag{2.19}$$

$$\nu_{ei} = n_i * \frac{Z^2 * e^4}{(4 * \pi * \epsilon_0)^2} * \frac{8 * \pi}{m_e * m_i * v_e^3} * \ln \Lambda \tag{2.20}$$

$$\nu_{ii} = n_i * \frac{Z^2 * e^4}{(4 * \pi * \epsilon_0)^2} * \frac{8 * \pi}{m_i^2 * v_i^3} * \ln \Lambda \tag{2.21}$$

$$\nu_{ie} = n_e * \frac{Z^* 2e^4}{(4 * \pi * \epsilon_0)^2} * \frac{8 * \pi}{m_i * m_e * v_i^3} * \ln \Lambda_c \tag{2.22}$$

where n_i=n_e is the plasma density, ϵ_0 is the permittivity of free space, and $ln\Lambda$ is the Coulomb logarithm given by:

$$\Lambda_c = \frac{4 * \pi * \epsilon^{3/2}}{3 * e^3} * \frac{T_e^{3/2}}{n_e^{1/2}} \tag{2.23}$$

Here the plasma parameter, Λ is assumed to be equal to the Coulomb logarithm. The collision time is the inverse of the collision frequency:

$$\tau_{12} = \frac{1}{\nu_{12}} \tag{2.24}$$

where 12 denote the two species being calculated (i or e). The mean free path before a collision is [44]:

$$\lambda_{mfp12} = v_{12} * \tau_{12} \tag{2.25}$$

Majority D ion or minority impurity - neutral collisions can lead to charge exchange with ions and plasma damping effects. Electron - neutral collisions knocks out an electron to either excite the neutral or to remove an electron which ionizes the neutral. The collision rate with neutrals is given in the same method as for plasma species:

$$\nu_{sn} = n_s * \sigma_{sn} * v_s \tag{2.26}$$

where the subscript sn means the species-neutral collision, n_s is the species density, σ_{sn} is the cross section of the species-neutral collision, and v_s is the velocity of the species. The cross-section of the interactions usually comes from modeling or experimental data.

The plasma ions and electrons move together like a fluid within the magnetic field. For the kinetics approach the Boltzmann equation give the states for particles not at

equilibrium. This can describe how heat, momentum, and energy are transferred in a fluid. The Boltzmann equation is given as [19]:

$$f_c(\overrightarrow{v}) = \frac{\partial f(\overrightarrow{x},\overrightarrow{v})}{\partial t} + \overrightarrow{v} * \frac{\partial f(\overrightarrow{x},\overrightarrow{v})}{\partial \overrightarrow{x}} + \frac{q}{m} * [\overrightarrow{E}(\overrightarrow{x},t) + \frac{\overrightarrow{v}}{c} \times \overrightarrow{B}(\overrightarrow{x},t)] * \frac{\partial f(\overrightarrow{x},\overrightarrow{v})}{\partial \overrightarrow{v}} \quad (2.27)$$

The collisionless treatment of the Boltzmann equation leads to the Vlasov equations and the Fokker-Planck equation can be used to simplify the collisional integral in the Boltzmann equation. The kinetic approach will lead to a more accurate result that will catch more phenomena such as Landau damping but the fluid approach allows for simplification of the problem and will suffice for this work. The fluid equation for the continuity for species, s, is given by:

$$\frac{\partial n_s}{\partial t} + \nabla \cdot (n_s * v_s) = 0 \quad (2.28)$$

where n is the density [19]. The fluid equation for momentum of species, s, is given by:

$$m_s * n_s = [\frac{\partial \overrightarrow{v}_s}{\partial t} + (\overrightarrow{v}_s \cdot \nabla) * \overrightarrow{v}_s] = n_s * q_s(\overrightarrow{E} + \overrightarrow{v}_s \times \overrightarrow{B}) - \nabla p_j + F_{st} \quad (2.29)$$

where m is the mass of the species and F_{st} is the rate of momentum density loss by collisions, also called the friction force, which is defined as:

$$F_{st} = \nu_{st} * n_s * m_1(\overrightarrow{v}_s - \overrightarrow{v}_t) \quad (2.30)$$

where s is again the first species, t is the second species, ν_{st} is the collisionality of the two species [45]. The equation of state must also be satisfied for the fluid equations which is given by:

$$p_j * n_j^{-\gamma} = constant \quad (2.31)$$

where p is the pressure and γ is defined by the heat flux assumption and on the isotropy of the energy distribution [19]. γ is 1 for isothermal, 5/3 for adiabatic and isotropic with 3 degrees of freedom, 3 for 1 degree of freedom, and 2 for 2 degrees of freedom.

While particles are traveling additional forces can alter their path such as electromagnetic forces acting on a particle with charge q is given by:

$$m * \frac{dv}{dt} = q * \overrightarrow{E} + q * (\overrightarrow{v} \times \overrightarrow{B}) + \overrightarrow{F} \tag{2.32}$$

where m is the mass, q is the charge of the particle, $\overrightarrow{E}$ is the electric field, $\overrightarrow{v}$ is the velocity, $\overrightarrow{B}$ is the magnetic field, and $\overrightarrow{F}$ is all other forces acting on the particle [44, 46]. This force is also called the Lorentz force and gives the equation of motion for a single particle and electric and magnetic field. Other equations of importance are the Maxwell equations which describe a linear movement in electromagnetic fields:

$$\overrightarrow{\nabla} \cdot \overrightarrow{E} = \frac{\rho}{\epsilon_0} \tag{2.33}$$

$$\overrightarrow{\nabla} \cdot \overrightarrow{B} = 0 \tag{2.34}$$

$$\overrightarrow{\nabla} \times \overrightarrow{E} = \frac{\partial \overrightarrow{B}}{\partial t} \tag{2.35}$$

$$\overrightarrow{\nabla} \times \overrightarrow{B} = \mu_0 * \overrightarrow{J} + \mu_0 * \epsilon_0 * \frac{\partial \overrightarrow{E}}{\partial t} \tag{2.36}$$

where ρ is the charge density, ϵ_0 is the electric permittivity of free space, μ_0 is the magnetic permeability of free space, and $\overrightarrow{J}$ is the electric current density [19, 46, 47]. Equation 2.33 is Coulomb's Law, Equation 2.34 is Gauss's Law, Equation 2.35 is Faraday's Law, and Equation 2.36 is Ampere's Law which together make the Maxwell equations. Maxwell's equations and the Lorentz force make up the classical electromagnetism foundation.

From Equation 2.32 looking at the other forces term which affects the transport of the plasma by changing the guiding center. These forces come in the form of particle drifts due to magnetic, $\overrightarrow{B}$, and electric, $\overrightarrow{E}$, field affects. The $\overrightarrow{E} \times \overrightarrow{B}$ drifts are given by [19]:

$$\mathbf{v}_{\overrightarrow{E}\times\overrightarrow{B}} = \frac{\overrightarrow{E}\times\overrightarrow{B}}{B^2} \tag{2.37}$$

Other drift cases to note come from a nonuniform $\overrightarrow{E}$, a gravitational field, a gradient $\overrightarrow{B}$ drift, a curved vacuum field, a polarization drift, and a curvature drift given by the following equations.

Nonuniform $\overrightarrow{E}$:

$$\mathbf{v}_{\overrightarrow{E}} = (\,1 + \frac{1}{4} * r_L^2 * \nabla^2)\,\frac{\overrightarrow{E}\times\overrightarrow{B}}{B^2} \tag{2.38}$$

Gravitational field:

$$\mathbf{v}_{\overrightarrow{g}} = \frac{m}{q} * \frac{\overrightarrow{g}\times\overrightarrow{B}}{B^2} \tag{2.39}$$

Gradient $\overrightarrow{B}$, also called grad B drifts:

$$\mathbf{v}_{\nabla\overrightarrow{B}} = \pm\frac{1}{2} * \nu_\perp * r_L * \frac{\overrightarrow{B}\times\nabla\overrightarrow{B}}{B^2} \tag{2.40}$$

Polarization drift:

$$\mathbf{v}_{\overrightarrow{p}} = \pm\frac{1}{\omega_{cs} * \overrightarrow{B}} * \frac{d\overrightarrow{E}}{dt} \tag{2.41}$$

Curved vacuum field:

$$\mathbf{v}_{\overrightarrow{R}} + \mathbf{v}_{\nabla\overrightarrow{B}} = \frac{m}{q} * (\,v_\parallel^2 + \frac{1}{2} * v_\perp^2) \; * \frac{\overrightarrow{R}_c \times B}{R_c^2 * B^2} \tag{2.42}$$

Curvature drift:

$$\mathbf{v}_{\overrightarrow{R}} = \frac{m * v_\parallel^2}{q} * \frac{\overrightarrow{R}_c \times B}{R_c^2 * B^2} \tag{2.43}$$

Diamagnetic Drift:

$$\mathbf{v}_{\overrightarrow{D}} = \frac{-\nabla p \times \overrightarrow{B}}{q * n * B^2} \tag{2.44}$$

Where **v** is the velocity of the drift in question, r_L is the Lamor radius, $\overrightarrow{g}$ is the gravitational force, $\nu_{\|}$ is the parallel velocity of the particle, $\nu_{\perp}$ is the perpendicular velocity of the particle, R_c is the radius of curvature of the force in question, n is the density, and p is the pressure [46]. The diamagnetic current is the sum of the $\overrightarrow{E} \times \overrightarrow{B}$ drift and the diamagnetic drift and is dependent on the particle charge.

2.4 Impurity Transport

Thus far the transport has been described for a single ion and electron plasma. Here a minority impurity species transport within a plasma is considered. To understand understand the impurity transport the impurity drift velocity is derived and compared to the diffusion coefficient. Starting with the total radial impurity flux density, $\Gamma_r(r,t)$, normalized by the density, n, given by [45]:

$$\frac{\Gamma_r(r,t)}{n(r,t)} = -D(r) * \frac{1}{n(r,t)} * \frac{\partial n(r,t)}{\partial r} + v(r) \tag{2.45}$$

where r is the radius, t is time, D is the diffusion coefficient and v is the drift velocity. For the steady state case, $\Gamma_r = 0$, which yields:

$$v(r) = D(r) * \frac{1}{n(r)} * \frac{\partial n(r)}{\partial r} \tag{2.46}$$

The general case drift velocity can then be compared to the diffusion coefficient for an infinitely long cylinder from:

$$\frac{v(r)}{D(r)} = \frac{1}{n(r)} * \frac{\partial n(r)}{\partial r} \tag{2.47}$$

Next, the classical diffusion coefficient and classical drift velocity are derived to calculate the v/D. Considering the transport from friction forces perpendicular to ∇p_s and $\overrightarrow{B}$ gives the classical impurity transport. A shifted Maxwellian approximation is applied with $F_{\perp,st}$ in Equation 2.30 having zero order velocities $(\overrightarrow{v}^0_s - \overrightarrow{v}^0_t)$. The only difference in the diamagnetic velocities leads to the different fluid frictions. The perpendicular velocity of the plasma species, $v_{\perp,s}$, is then given by:

$$v_{\perp,s} = \frac{m_s}{q_s * B^2} \sum_{t \neq s} \nu_{st} * (\frac{\nabla p_t}{q_t * n_t} - \frac{\nabla p_s}{q_s * n_s}) \tag{2.48}$$

The first order velocity is in the direction of the pressure gradients. The pressure being a function of temperature and density can be split into those respective terms to get a term proportional to ∇n_s. Impurities that enter the plasma from erosion of the PFCs can lead to increased sputtering or impurity accumulation at flux-line end points. The minority impurity species are assumed to flow with the background plasma species and the radial impurity flows can a cause impurities to move from the edge plasma to the core due to diffusion or convective flows. These effects can lead to impurity gradients causing additional impurity movement. The classical diffusion coefficient, D_{CL}, is the proportionality factor from the pressure gradient, and is given by:

$$D^y_{CL} = \sum_{x \neq y} D^{yx}_{CL} = \frac{4 * \sqrt{2 * \pi}}{3(4 * \pi * \epsilon_0)^2 * \sqrt{k_b * T_e} * B^2} * \sum_{y \neq x} \sqrt{m_{yx}} * ln\Lambda_{yx} * q_x^2 * n_x \tag{2.49}$$

where y is now the impurity species, x is the plasma fluid species, and m_{yx} is the reduced mass ($m_y m_x/(m_y + m_x)$). Here the friction with electrons is negligible due to its mass. The classical diffusion term can be used to get the classical impurity drift velocity, $\overrightarrow{\nu}_{CL}$ given by:

$$\overrightarrow{v}^y_{CL} = \sum_{x \neq y} D^{yx}_{CL} * \frac{q_y}{q_x} * [\frac{\nabla n_x}{n_x} - \frac{\nabla T_e}{T_e}(\frac{3 * m_{yx}}{2 * m_x} - 1 - \frac{q_x}{q_y}(\frac{3 * m_{yx}}{2 * m_y} - 1))] \tag{2.50}$$

where ∇n_x is the density gradient and ∇T_e is the temperature gradient. The temperature gradient drives heavier impurities to the plasma edge which is called temperature screening [45, 48]. Now looking at the v/D the diffusion coefficient falls out.

The Bohm diffusion coefficient can be compared to the classical diffusion coefficient and when doing so has found good agreement in modeling [49]. The Bohm diffusion is given by:

$$D^{Bohm}_{\perp} = \frac{1}{16} \frac{k_b * T_e}{e * B} \tag{2.51}$$

Chapter 3

Experimental Set-up

3.1 Proto-MPEX

3.1.1 Linear Plasma Device - MPEX

Tokamaks in their current state leave gaps in the material science research on fusion materials. There is lack of data for ITER, DEMO, or beyond which utilize relevant fluxes, fluences, and divertor plasma conditions. Neutron damaged materials exposed to a plasma also have little to no data on them. A new device that can fulfill these research gaps and aid in finding new materials that perform in these situations is needed. This need has been recognized by the U.S. Department of Energy (DOE) and the fusion community. A new project has gotten federal budget approval; the Material Plasma Exposure eXperiment (MPEX) device [50].

MPEX is designed to be a steady state linear plasma device that will have independent ion and electron temperature control and have the capability of imparting a high ion flux to a tiltable target that can be neutron irradiated *a-priori*. These capabilities are designed to meet the fusion relevant plasma conditions to answer key questions on the materials to be used in future reactors [51]. The site for this project will be at Oak Ridge National Laboratory to make use of their material science expertise and access to the high flux isotope reactor for use of neutron irradiations. The design of MPEX is given in Figure 3.1. MPEX's design has a set of 21 superconducting magnets in seven cryostats to achieve

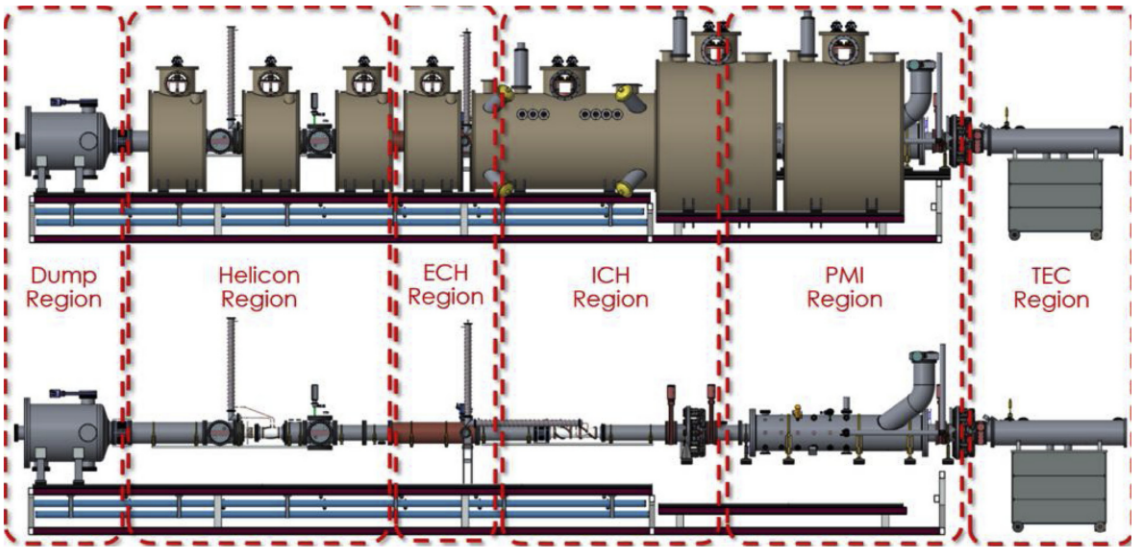


Figure 3.1: The conceptual design of MPEX. Reproduced from [52].

the desired magnetic field profile [52]. MPEX will use a helicon antenna as its primary ionization source, Electron Bernstein Wave heating for the electron heating, and ion cyclotron heating for ion heating. The PMI region is designed to detach via auto-couplers to protect workers from the irradiated samples and for automated transport to the surface analysis station.

3.1.2 Proto-MPEX for R&D of MPEX

The Prototype-Material Plasma Exposure eXperiment (Proto-MPEX) is the plasma source R&D device for the MPEX project [53]. Proto-MPEX's goal is to demonstrate the parameter space, ion and electron heating schemes, and the magnetic profile shape that MPEX will need as predicted by modeling [54]. Plasma and impurity transport, heat flux to various components, radiation shielding, and diagnostic needs are also in the research and development scope of Proto-MPEX.

3.2 Proto-MPEX's Geometry

Proto-MPEX has had two geometry conditions from 2016 to 2020. The first one being a 12 magnet coil configuration that was used until the summer of 2018 and the second one being an upgraded 13-magnet coil configuration from the late summer of 2018 till mid 2020 as described in Ref. 55. Figure 3.2 shows the configuration used with the 12 magnet coils and the associated typical magnet field case. This field was used to provide the correct magnetic field for the helicon RF antenna, electron cyclotron heating, ion cyclotron heating, and target magnetic field strength. The 13-magnet coils setup was also used for further optimization of the plasma heating schemes. Figure 3.3 shows the plasma radius and magnetic field profile used with the 13-magnet coils. The coils are pancake Helmholtz coils with 30 winds of copper and are water cooled. The locations between coils are called spools (i.e. spool 6.5 is between coils 6 and 7) and are the location of diagnostics and access to heating sources.

A helicon antenna is used because of its high ionization efficiency and ability to produce a high-denity plasma. The helicon produces a right-handed whistler wave at 13.56 MHz that can propagate into a high-denity plasma [56]. This antenna is operated with an FRT-

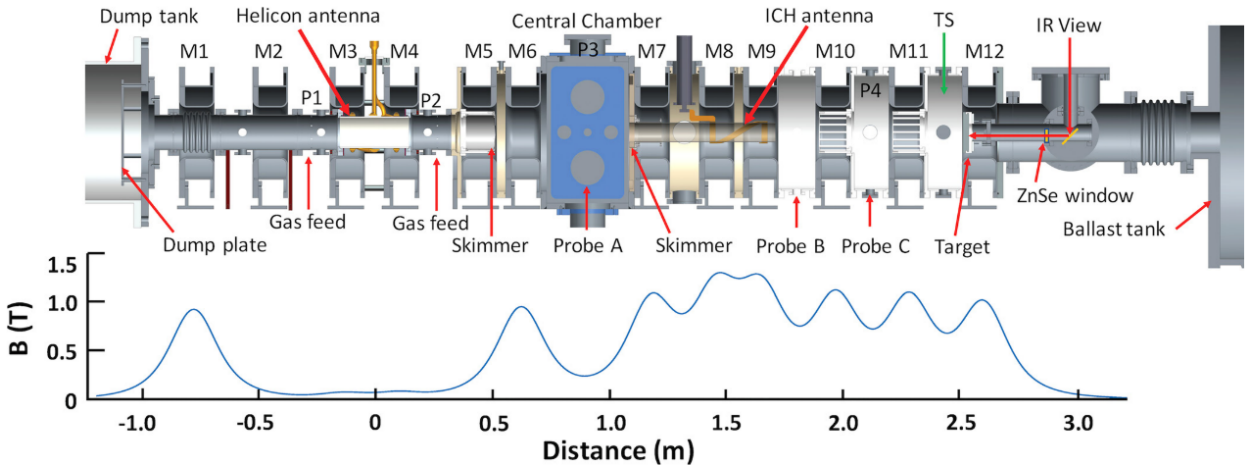


Figure 3.2: Proto-MPEX 12 magnet coils configuration and associated typical magnetic field profile. M1-M12 represent the magnet locations with the space between them noted as spools 1.5 to 11.5. Reproduced from [53].

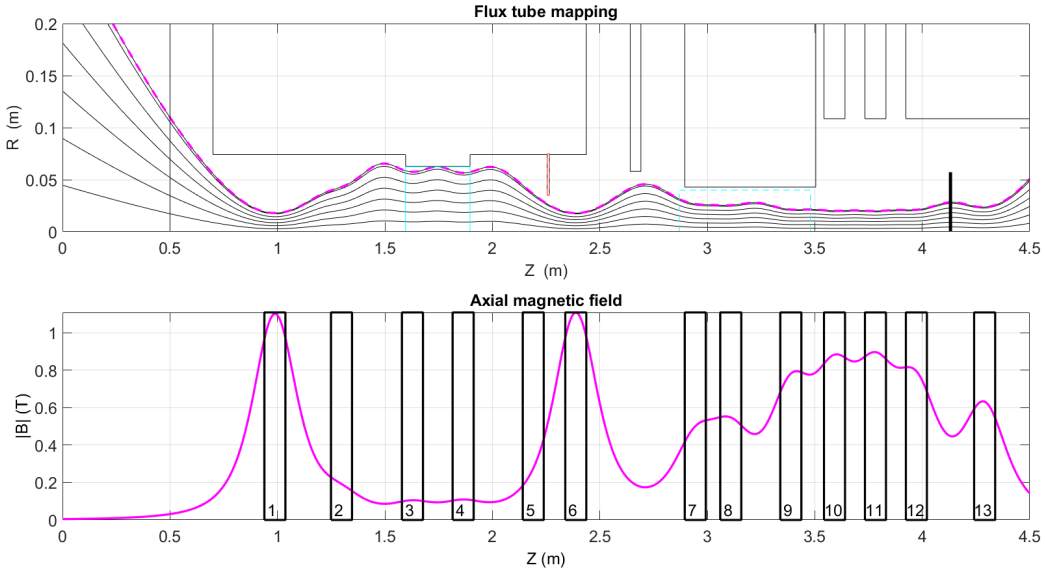


Figure 3.3: Proto-MPEX 13-magnet coils typical magnetic field profile and plasma radius size. The black numbered boxes indicate the magnets and the space between them is referred to as spool 1.5 to 12.5. Here, Z=0 m is the dump plate location of Figure 3.2.

86 and/or a newer Sairem RF transmitter [57] that outputs 100 kW per transmitter which produces typical densities when using a single transmitter of $1 - 6 * 10^{19}\ m^{-3}$ based on the magnetic field used. The helicon launches in a lower magnet field section of the machine, namely under magnet coils 3 and 4. It launches both towards the target, referred to as downstream, and towards the dump plate which is technically another target but often referred to as the upstream side of the machine. The helicon region, however, is the upstream location within the two-point model. An AlN ceramic sleeve is used as the vacuum boundary inside the helicon antenna and is an RF window allowing the RF wave to ionize to the injected gas. The helicon antenna and AlN window are shown in Figure 3.4. The AlN ceramic sleeve will be referred to as the helicon window within this work. The helicon window is not actively cooled on Proto-MPEX but will be on MPEX. The helicon window's safety limit is 373 K and a pulse length of greater than 1.5 seconds reaches this limit. Most pulses are 500 ms for R&D campaigns and either 500 or 1000 ms for material exposures. To prevent the helicon window from ratcheting in temperature usually 3 minutes per 500 ms pulse length is used to allow to the helicon window to cool. This sets the pulse repetition rate and defines the number of plasma shots taken within a day.

Proto-MPEX in its most current state also makes use of a stainless-steel limiter that is between coils 4 and 6. This limiter is to move the last uninterrupted flux surface (LUFS) from the helicon window to the limiter by altering the magnetic field under the helicon antenna. This is the design for MPEX with purpose of reducing the heat flux on the helicon window. Proto-MPEX also makes use of a skimmer plate under magnet 5 which helps to eliminate neutrals moving towards the target region during the gas puff just before plasma ignition. The skimmer plate at magnet 5 along with another one after magnet 6 also allows for differential pumping which maintains a high vacuum near the target while having a much higher pressure during the gas puff at the helicon region.

The electron cyclotron heating (ECH) has been used in the form of a 28 GHz gyrotron and a 105 GHz gyrotron. The gyrotron passes the microwaves through a mode convertor tank and passes through a mirror to be focused into the plasma core. The primary goal is for O to X to Electron Bernstein Wave launch (EBW) [58–60]. The EBW waves have no cut off density and thus should work well with the high-denity helicon plasma [53]. The

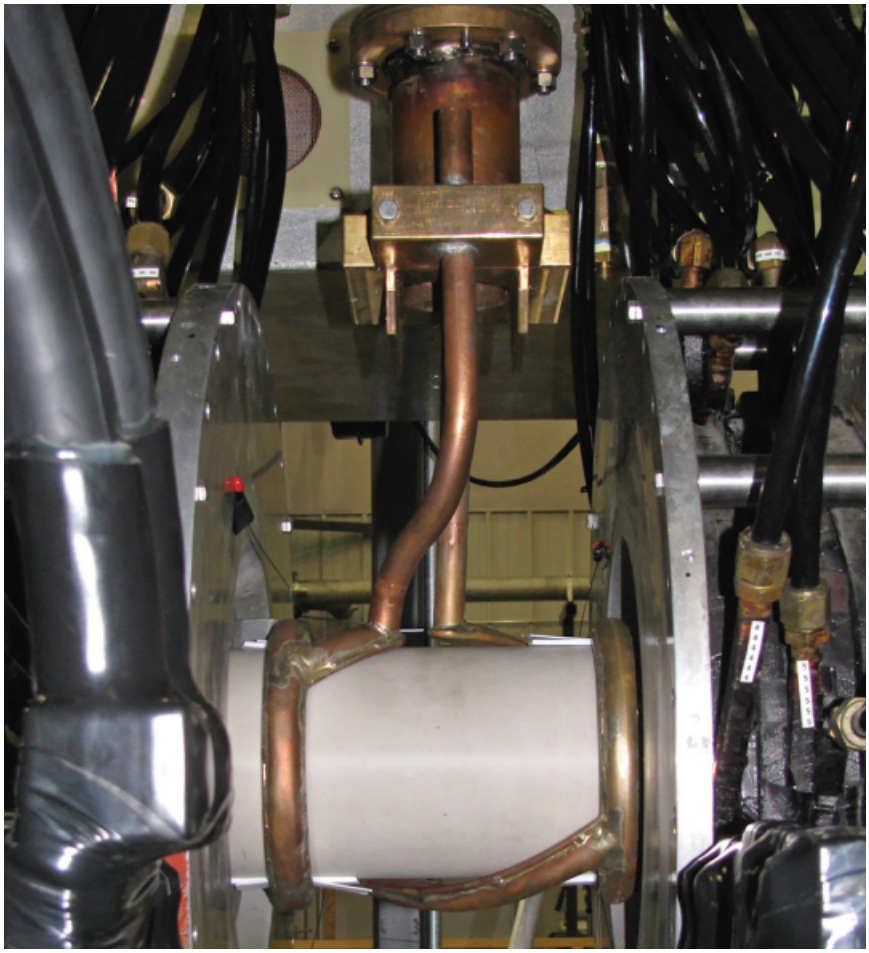


Figure 3.4: The installed Proto-MPEX copper helicon antenna and aluminum nitride ceramic window. Reproduced from [53].

launching location has been tried at multiple spots between spool 6.5 and the target at spool 12.5. The primary location after the upgrade has been at spool 8.5 because of the magnetic field at this location. The 28 GHz microwave system usually has pulses much shorter than the helicon pulse length, on the order of up to 100 ms but has gone up to 500 ms.

The ion cyclotron heating (ICH) has taken two forms, the first being as an internal 25 cm ICH antenna that operated with left-handed wave that was launched at the ion frequency of 7-9 MHz and the second being installed after the summer 2018 upgrade where an external 30 cm ICH antenna that launches at 6-9 MHz was used. A quartz sleeve sits inside the ICH antenna similarly to the helicon design. Figure 3.5 shows the internal ICH antenna used both outside and inside Proto-MPEX at spool 7.5 to spool 8.5. Figure 3.6 shows the external ICH antenna along with the quartz sleeve inside of the antenna used at launching location spool 8.5. The ICH pulse is $\sim$ 250 ms in length at 35 kW input power from an FRT-85 transmitter.

3.2.1 Material Targets of Proto-MPEX

Proto-MPEX has had multiple targets at the spool 12.5 target location as shown in 3.2 since June 2016. Beers et al. [61] describes in more detail many of the targets used in the recent Proto-MPEX campaigns. The first target at this target spool location was a thin stainless-steel target that had a bead roughened surface. The bead roughening is to help with infrared (IR) imaging of the target.

The stainless-steel target was changed out for a graphite target in June 2017. The graphite target included five embedded probes: four double Langmuir Probes and one ion flux collecting probe. The probes and their results are discussed in a later section, but the purpose of this target was to measure the plasma conditions directly at the target face.

The graphite target was changed out for a 1/16" thick heated water blasted stainless-steel target in April 2018. The heating element consisted of a resistive wire that was bolted to the stainless-steel plate and a power supply. The heated target was used to calibrate the IR imaging in between shots as the first thin stainless-steel target was damaged from the plasma exposures and changed the emissivity of the targets.

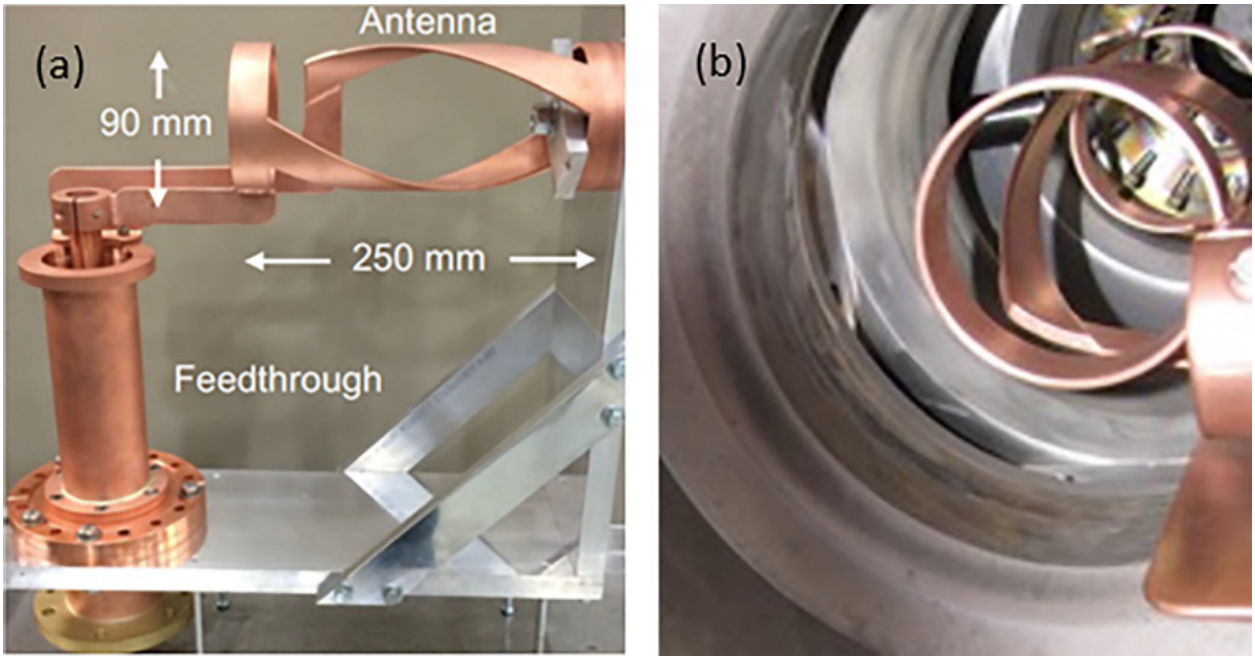


Figure 3.5: The internal ICH antenna on (a) outside the machine and (b) installed inside the machine. Reproduced from [62].

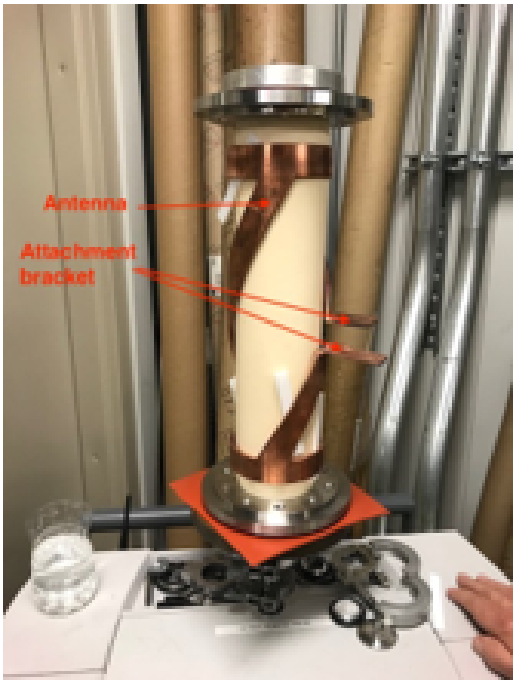


Figure 3.6: The external ICH antenna and internal quartz sleeve used after the summer 2018 Proto-MPEX upgrade.

For April 2018 - May 2018 a heated SiC target was used. This target had a stainless-steel holder with a lip over the SiC edge to maintain an unexposed SiC section so post exposure analysis could be done to compare to the plasma exposed surface. The SiC was a 3" disc that was 1/4" thick and had a resistive heating wire in that was encased in two stainless-steel pieces to provide better heat transfer that had a graphine layer between the stainless-steel and the SiC. This target setup was on an internal pair of bellows to provide target movement along the z-axis of the machine.

From late May 2018 - September 2018 Proto-MPEX was under way with its upgrade to the 13-magnet coil configuration after which from September 2018 - March 2019 a thin stainless-steel target attached via a support rod on a short bellows external to the machine was used to provide z-axis movement of the target as well as some x and y movement.

3.2.2 Material Analysis and Particle Probe on Proto-MPEX

From March 2019 onwards a target exchange system was used on Proto-MPEX which was part of the Proto-MPEX Material Analysis and Particle Probe (MAPP) (Proto-MPEX MAPP). The target exchange chamber is comprised of a Lesker MultiCentre Analytical Stage [63] and a custom vacuum chamber. The target stage is a heated target holder with a 1000 mm bellow stroke that is used to move the target into the target chamber of Proto-MPEX and then back out for exchange. The heater on the target can heat targets to 1273 K at steady state. This is in the range of surface temperatures of interest for PMI experiments. The target holder allows for tilting of the target to from -180° to 180° with a 1° accuracy and a hard stop at 6 o'clock to prevent twisting of internal wires. The target moves through a Proto-MPEX MAPP custom built ultra-high vacuum (UHV) chamber. The MAPP chamber was built by Nor-Cal Products [64] and was designed by collaboration between the University of Illinois: Urbana-Champaign (UIUC) and Oak Ridge National Laboratory (ORNL). The Proto-MPEX MAPP system is designed in the same fashion as the original MAPP on NSTX-U [65]. The port locations along with a computer aided design (CAD) file of the MAPP are shown in Figure 3.7. This chamber has ports that support the diagnostics of X-ray photoelectron spectroscopy (XPS) [54.7°], residual gas analyzer (RGA) which can be used for thermal desorption spectroscopy (TDS) [150°], Raman spectroscopy [90°], forward

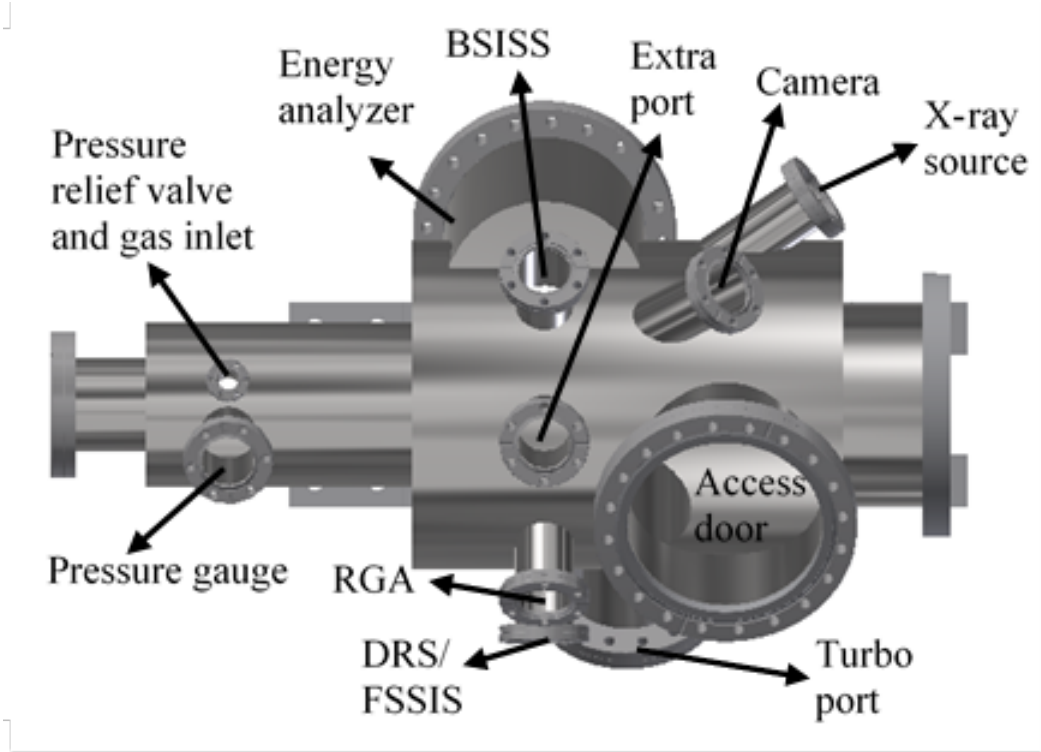


Figure 3.7: The port allocations of the MAPP vacuum chamber. Reproduced from [66].

scattering ion scattering spectroscopy (FSISS) [18°], back scattering ion scattering spectroscopy (BSISS) [135°], and direct recoil spectroscopy (DRS) [18°]. All of the diagnostic port angles given are designed such that their angle from the energy analyzer port will allow for maximum signal collected. Figure 3.8 shows the angles of the diagnostics from a cross-section of the CAD model except for the x-ray source which is on a different plane at 54.7°. The scope of work document with all of the angles, tolerances, wall thicknesses, and design specifications for the MAPP chamber that was built by Nor-Cal are given in Appendix 4.

Proto-MPEX is currently using the a digital RGA from the ITER project which can be used on the MAPP chamber. The XPS and energy analyzer used on the NSTX's MAPP chamber are used again on the Proto-MPEX MAPP. A 15 kW PSP Vacuum CTX400 x-ray source is used as the x-ray source. The XPS measurements are taken with a Comstock AC-901B hemispherical energy analyzer. The target is aligned via the target stage to a working distance of 5-10 mm from the energy analyzer which is dependent on the x-ray alignment to the target center. The MAPP chamber has the other diagnostic ports blanked off due to lack of funding at this time.

Figure 3.9 shows the MAPP chamber and bellows as it is installed on Proto-MPEX along with the target holder. The MAPP had many space requirements to meet in its design: the section that attaches to the gate valve on Proto-MPEX needed to fit between two of the magnet coil leads and the length of the main chamber along with the bellows also needed to fit between Proto-MPEX and the wall. The design was made such that it fits between two magnet leads for magnets 12 and 13. The bunny ears for ports 9 and 10 had to be set to the angle of 34° to fit between the magnet leads and other diagnostics on the target spool. The tubing that ports 9 and 10 connect to and that leads to the 4.5" conflat flange that connects to the Proto-MPEX target region had to have the outer diameter reduced from 5" to 4" to allow for more clearance between the two magnet leads. The sample retrieval door was repositioned many times during the design of the MAPP due to wanting the door to be outside of the magnet safety zone, be above the horizontal mid plane of the chamber to make sample retrieval easier, and to be on the side of the MAPP facing an open area for easy access. The gate valve is there for isolation of the MAPP chamber to either increase the vacuum levels for diagnostic operations or to vent the system via air or nitrogen without

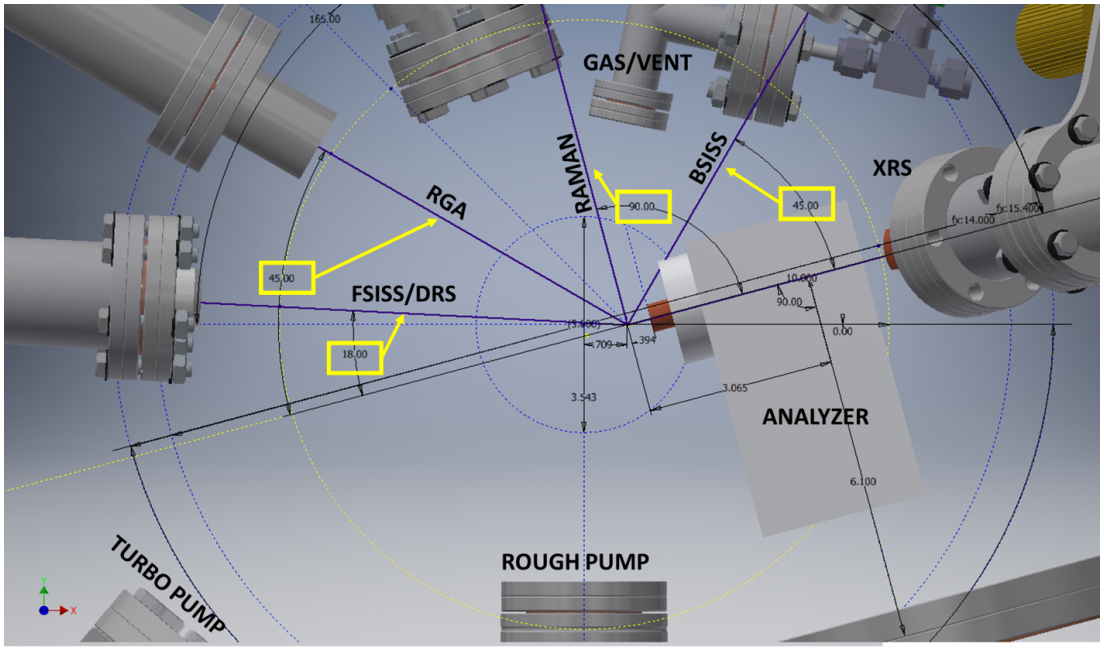


Figure 3.8: A cross-section of the MAPP CAD model showing the angles used for the diagnostics except for the X-ray source which is out of plane of the other diagnostics.

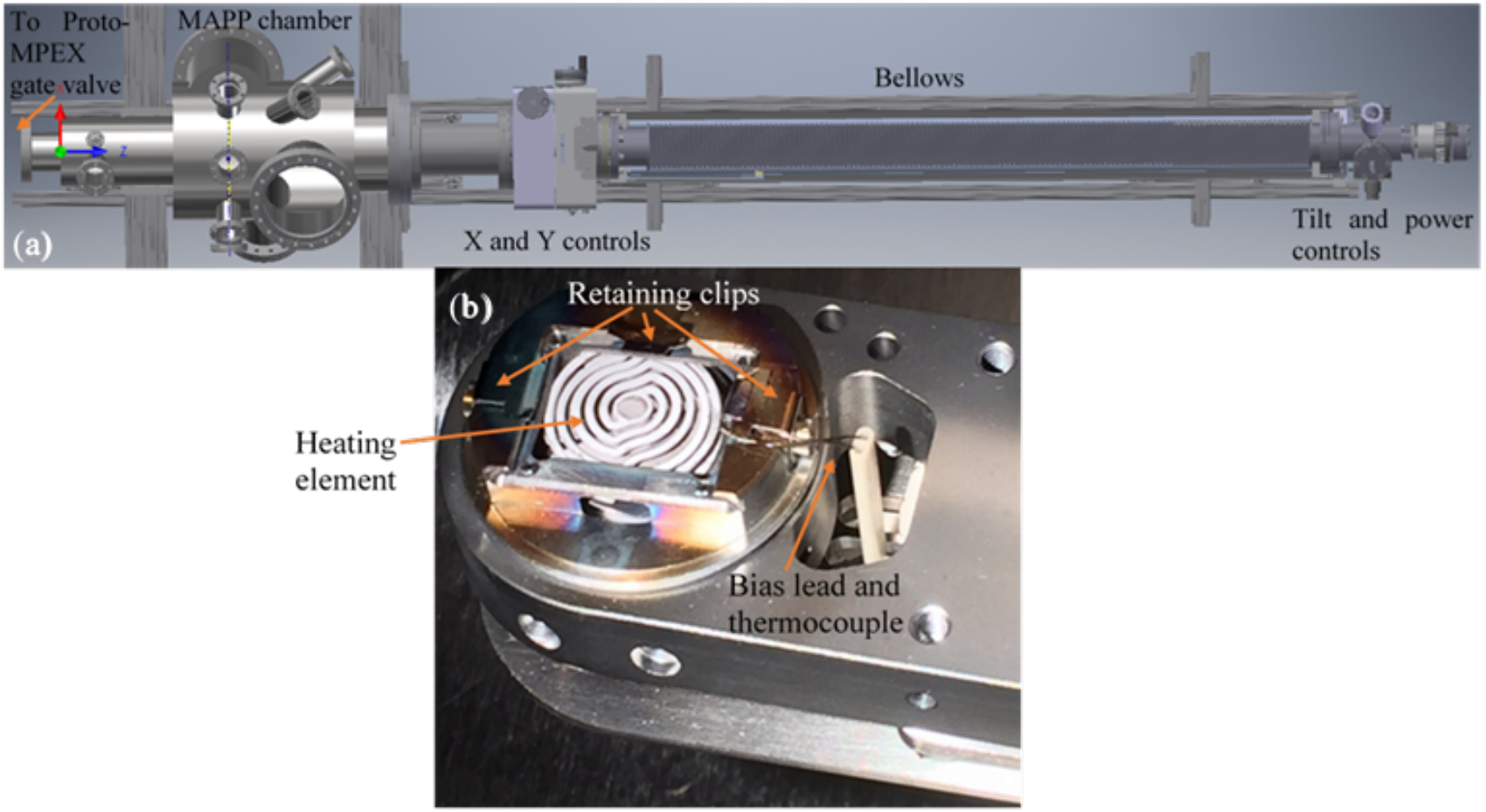


Figure 3.9: (a) The target region on Proto-MPEX with the MAPP chamber and bellows which moves the target holder in and out of the target region for exposure. The gate valve between the MAPP chamber and the target region of Proto-MPEX is to isolate the MAPP for higher vacuum to be achieved for diagnostic operations and to bring it up to area for sample retrieval from the door. (b) The target holder showing the heating elements for the sample, which is controlled via feedback loop from the thermocouple, the biasing capabilities via the bias lead, and the target retaining clips which hold the sample in place as well as the bias and thermocouple wires. The discoloration is from plasma exposure.

having to vent the rest of Proto-MPEX. The turbo pump port is designed for a 270 l/s Pfeiffer pump but the only working pumps on hand were a Pfeiffer 170 l/s pump. These turbo pumps can operate at angles of 180 to 360°. This pump allows for a vacuum level in the MAPP of $1 * 10^{-5}$ Pa after vacuum conditioning. The samples are loaded/unloaded via the door and slide into molybdenum (Mo) retaining clips that secure the sample on the heating element for good thermal contact. These clips also hold the thermocouple and bias lead to the target. The target also has biasing capabilities via the bias lead of up to 50 V while the target is heated. If the target is not being biased the bias MHV connector needs to be terminated with a 50-ohm connector to have the heating element work. The 50-ohm connector grounds the target with a grounding chain. The thermocouple wire provides a feedback loop to the dual heating mode Heat3 power supply from Prevac. The dual mode allows for heating via resistive heating up to 973 K and via electron beam heating up to 1273 K steady state or up to 1473 K with flash heating for up to two hours.

The MAPP targets are based on the given design target design from Lesker/UHV Design. The samples have a grip tab with a hole for special tongs or tweezers to make sample retrieval easier. Figure 3.10 shows the standard 1 mm thick design for pure metal targets and a modified top hat design for holding ceramic samples. The ceramic pieces are harder to machine into the odd geometry of the pure metal targets so a TZM top plate is used for holding the sample. Optional Grafoil from Lamons gasket company and a back TZM plate can be used to sandwich the ceramic piece if needed. The MAPP itself will need shielding around the bias and thermocouple wires as their small thermal mass can melt under plasma exposure in Proto-MPEX. Figure 3.11 shows (a) a piece used to shield the side of the target holder so plasma doesn't get to the internals when the target is tilted and (b) a front plate to shield the bias and thermocouple wire. An addition top shield with center hole diameter of 3 mm instead of 12 mm can be used when biasing the sample to reduce the current collected by the target. The MHV connector for the biasing wire can handle 3 amps but exposing the whole target surface to the plasma would draw much more than that. Limiting this hole size to 3 mm will lead to about 1 amp of current drawn. The gyro radius of the ions in Proto-MPEX are mid 10^{-4} m which will also still allow for ions to be collected through the small opening by the biased target. Due to the height of this top shield as very shallow

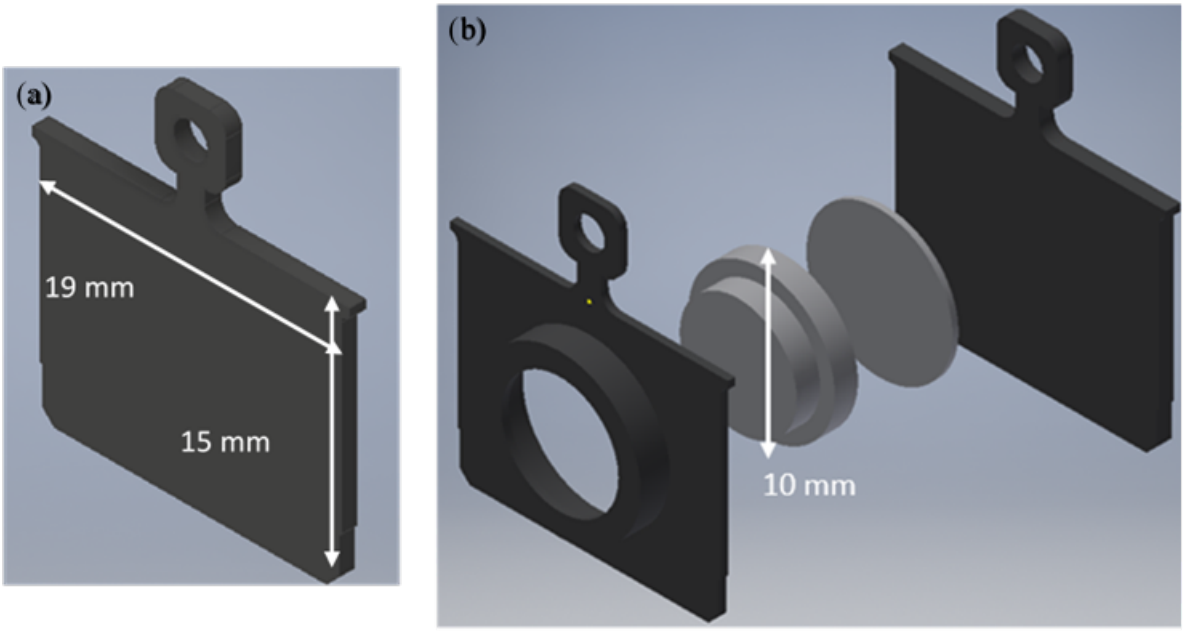


Figure 3.10: (a) The geometry for 1 mm thick pure metal targets to be used in the MAPP and (b) the geometry for a 10 mm diameter ceramic top hat pieces with a TZM retention plate in front and an optional Grafoil and TZM backplate behind.

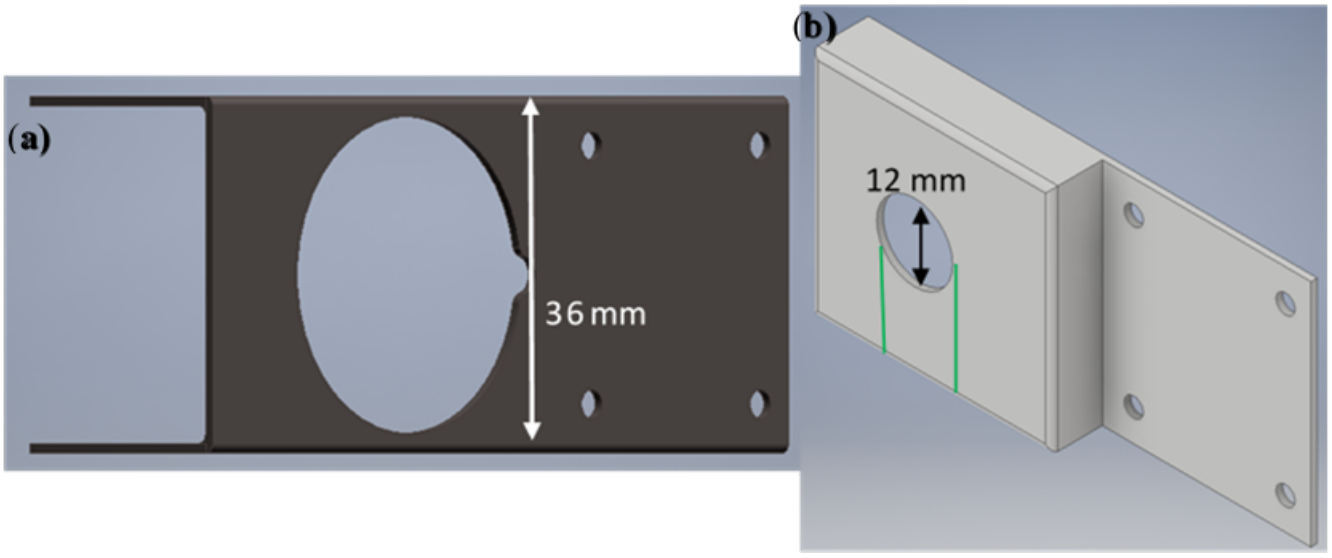


Figure 3.11: (a) The geometry for 1 mm thick TZM side shield to be used in MAPP tilted target experiments and (b) the geometry for a front shield to protect the bias and thermocouple wires along with the retaining clips. The green lines represent where material will be removed on an additional MAPP shield that would be used for tilted target experiments as to not shadow the target.

angles the shield would completely shadow the target from plasma thus another top shield has been made with part of the hole slit down the side to remove the part of the shield blocking the plasma from reaching the target. The green marks in Figure 3.11 (b) represent the location of where material is to be removed to make the slit hole shield.

3.3 Proto-MPEX Diagnostics

Proto-MPEX makes use of many diagnostics that have been built as a proof of principle design, for the ITER project, or built directly for measuring Proto-MPEX's parameters. Most of the diagnostics are flexible with their installation location but some are specifically for the target or helicon characterization. Only the diagnostics used in this work are discussed in the following sections.

3.3.1 Double Langmuir Probes

The double Langmuir probe(s) (DLP(s)) are constructed of two molybdenum (Mo) collecting wires that are housed in a dual or quad bored alumina ceramic rod. Double probes are used because this allows for RF compensation [67]. This alumina rod is encased in stainless-steel outside of the plasma exposed region to reduce RF pickup. The quad bored alumina is for including an additional two Mo collecting wires to be used for plasma flow collecting Mach probes. The two Mo wires for the DLP are swept at ±40 V to collect past the saturation current and see the knee characteristic of the J_{sat} versus V curve. The fitting routine to determine the plasma density and temperature follows the steps as shown in Beal et al. [68]. Multiple DLPs can be installed on Proto-MPEX at the same time but typically only one is operated at a time for collecting the plasma density and temperature. If diagnosing the helicon region, the probe can be installed at spool 2.5 and if diagnosing the target plasma then the probe at spool 12.5 is used. This target DLP cannot be used at the same time as when the MAPP is in the target region due to a likely collision.

3.3.2 Mach Probe

A Mach probe is probe for measuring plasma flow. Two Mo metal wire probe tips are exposed to the plasma and the difference in current collected gives the Mach number. The flow in one direction is greater for a flowing plasma which leads to a difference in collected current when the probe tips are aligned along the direction of flow. The tip facing the plasma will have a higher flow while the tip shadowed by the probe will have a lower current. Some of the Mach probes on Proto-MPEX are two bore alumina ceramics allowing for only Mach number collection and some are four bore, having the other two bores for a DLP. The four bore probes allow for collection of plasma density, temperature, and Mach number simultaneously and at the same radial location within the plasma. The Mach probes are also on a probe drive allowing for radial scans. Mach probe measurements were compared to B2.5 Eirene modeling for Proto-MPEX in Ref. [69].

3.3.3 Capacitive Probe

Electrostatic or capacitive probes work based on the principle of capacitively coupling the probe tip with the plasma. The probe tip is a metal wire (either Mo or W) that is housed in dielectric material (Alumina) [70, 71]. An image current is induced on the probe tip and current flows to the ground. The measured current through a resistor gives a voltage. This voltage is the measure of the RF potential. On Proto-MPEX the capactive probe is installed at spool 6.5 at Z=2.75m and has the capability to be moved into the plasma via a bellows with a ruler for marking the distance from the chamber center line allowing for radial scans.

3.3.4 Thomson Scattering

Thomson scattering is taken as the gold standard for plasma electron density and temperature. The laser used is a Nd:YAG at 1064 nm which is frequency doubled to 532 nm. The laser pulses are created from a Q-switched Spectra Physics Quanta Ray Pro-350. The laser has a power of 1.4 J per 8 ns pulse at a repetition rate of 10 Hz. The laser passes through the center point of the target spool as shown by the green arrow in Figure 3.2. The Thomson signal is collected using a Kaiser Optical Systems Holospec spectrometer with

a Princeton Instruments PI MAX III intensified charge-coupled device (ICCD) camera to read the spectrometer output. With Proto-MPEX's short plasma shot times only a few laser pulses can be collected for statistics in a plasma shot. The low statistics leads to many plasma shots being needed to collect enough photons to get a fit for temperature and density. The needed collection times can lead to needing a large portion of a day for Thomson statistics and given that there is agreement between Thomson scattering and DLPs [61], the DLPs will be used to get the plasma density and temperature. However, MPEX being a steady state device Thomson data collection is easier and the DLPs would like melt if not on a reciprocating mechanisms so Thomson will be the primary plasma density and temperature diagnostic. More detail on the Thomson scattering system can be found in Ref. [72, 73]

3.3.5 Visible Spectroscopy

Proto-MPEX uses a McPherson 2051 Czerny-Turner 1-m spectrometer with five viewing cords (McPherson) that connect to any of the fiber optic fibers looking into Proto-MPEX. Proto-MPEX makes use of in house made fiber optic mounts which sit on $2\frac{3}{4}$" conflat flange windows. They can either be straight views or views that have a 7 or 10° offset to measure Doppler broadening of ions. The views are columnated and angled such that the views all cross at the center of the vacuum vessel. The McPherson uses an 1800 grooves/mm grating and a slit width of 30 μm to collect light which is then passed in a Princeton Instruments PhotonMAX 512B EMCCD camera. The light collection time is varied based maximizing the photon signal while maintaining enough time resolution to see the changes that occur during the plasma discharges.

Proto-MPEX also makes use of four Edgertronic fast framing visible cameras [74]. There are three black and white cameras and one color camera that are used at various locations on Proto-MPEX. The cameras collect light at 1000 Hz with a pixel size of up to 1280 x 1024 but typically are smaller due to them being position on 4.5" conflat flange windows. The views are made smaller to not seen the window edges, to reduce the file sizes, and to allow for the 1000 Hz framing rate. The IR blocking on these cameras is also not present to allow for collection of spectral peaks in the 600-750 nm range. The spectral peaks are viewed by use of narrow band pass filters. These filters are 2" in diameter so they can be

screwed onto the lens of the camera. The filters used are narrow-band pass filters which have light transmittance around spectral lines of interest i.e. the hydrogen Balmer series emission peaks.

3.3.6 Infrared Camera Measurements

The target temperature is measured with a FLIR 655SC IR camera that is connected via an Ethernet cable to a PC containing the FLIR software ResearchIR. This IR camera has been used for a power balance study in Proto-MPEX [75, 76]. ResearchIR is used to pre-trigger and record the IR images at 100 Hz. The window transmittance, target baseline temperature, and target emissivity are inputs to the software to see live temperatures as well as to play back a recorded movie of the target temperature during a plasma shot. Post processing of the data can also done in MATLAB, a programing language and computational environment [77], using the ATLAS SDK from FLIR. This sdk for windows PCs is the library files that MATLAB uses to convert the data outputs from the camera to temperature values.

On the 13-magnet coil configuration of Proto-MPEX the IR camera views the plasma through a periscope located at spool 12.5 that looks at a mirror that is angled between the target face and the periscope. This mirror is outside of the plasma column and thus doesn't degrade during exposures. The mirrors are flat and give a straight reflection from the target to the periscope and then the IR camera. This mirroring rotates the true target image in the IR view which has been corrected with post-processing routines which also yield the heat flux.

Multiple operating temperature ranges work on the camera (123 to 673 K and 423 to 873 K) with the newest one as of January 2019 being 873K to 2273 K to record in the temperature range of the Proto-MPEX MAPP heated target capabilities. The maximum temperature of the Proto-MPEX target holder is 1473 K but is limited at this temperature for up to two hours. The steady state temperature of the target heater is 1273 K which is in the range of interest for the new camera temperature range setting.

3.4 Proto-MPEX's Operating Space

Proto-MPEX with use of its auxiliary heating scenarios can cover a broad range of operating space and has meet many of the desired conditions for MPEX [55, 78]. Table 3.1 shows a list of the conditions that Proto-MPEX has met with respect to the goals of MPEX.

3.4.1 Electron Density and Temperature

The electron density can be controlled with the helicon injected power level while the electron temperature stays relatively constant. Using the helicon only, the electron temperature is 2-3 eV while the electron density can range from $0.5 - 19\ x\ 10^{19}\ m^{-3}$ in the target region by using both the Sairem and FRT-86 RF transmitters together. These densities and temperatures in Proto-MPEX have been measured with several diagnostics: double Langmuir probes (DLPs) [67], Thomson scattering [72, 73], hydrogen Balmer series emission [79], helium line-ratio spectral-monitoring (HeLIOS) [80], and directly at the target with embedded flush mounted DLPs [61].

3.4.2 Ion Flux

The ion flux can be directly measured using an ion collecting electrode that is biased via:

$$\Gamma_{se} = e * j_{sat}(s) \ = \ 0.61 * n_{se} * c_s \ = \ 0.61 * n_{se} * \sqrt{k_b(\frac{T_e + \gamma * T_i}{m_i})}\ [ions\ m^{-2}\ s^{-1}] \quad (3.1)$$

where Γ_{se} $[ions\ m^{-2}\ s^{-1}]$ is the ion flux to the sheath entrance, e is the elementary charge, j_{sat} $[ions\ m^{-2}\ s^{-1}]$ is the ion saturation current incident on the probe area, n_{se} $[m^{-3}]$ is the density at the sheath entrance or the plasma density (n_e), c_s $[m\ s^{-1}]$ is the sound speed of ions, k_b is the Boltzmann constant in relevant units, T_e $[eV]$ is the plasma electron temperature, γ is 3 for adiabatic flow, T_i is the plasma ion temperature which is assumed to be equal to T_e, and m_i $[kg]$ is the mass of the plasma ions [19]. A single Langmuir probe, a

Table 3.1: Operational space for Proto-MPEX's target [55].

Parameter	Value	Note
Target n_e	$1.1 * 10^{20}\ m^{-3}$	Helicon at 150 kW
Target T_e	12 eV	With ECH and lower density
Target T_i	11 eV	With ICH and lower density
Target Flux	$1 * 10^{24}\ m^{-2}s^{-1}$	Helicon at 150 kW
Target B	1 T	At highest magnet currents
Plasma Diameter	8 cm	High Helicon magnetic field
Target Perpendicular Heat Flux	14 MW/m^2	With ECH and lower density

DLP, and Thomson with Equation 3.1 can give the ion flux but a single wire using its j_{sat} has the least assumptions and fittings applied to it making the measurement more accurate. The area of the wire is determined by a close-up picture with the probe and a ruler and then counting pixels in the image to determine probe length and diameter.

For the graphite target the Thomson scattering, DLP, and embedded flush mounted ion flux collector probe the ion fluxes agreed in value, $5 \pm 2.5 * 10^{23}\ ions\ m^{-2}\ s^{-1}$. The stainless-steel target measured density and temperature, and thus flux, has the Thomson scattering and DLPs disagreeing slightly [61]. This was not understood at the time but now is believed to be due to the target not being very well supported and swaying from the force of the plasma. This creates an oscillation in the density profile along the axis of the machine as was seen in the stainless-steel Balmer series ratios taken by Beers et al. [61]. The stainless-steel target has seen measured fluxes of up to $1 * 10^{24}\ ions\ m^{-2}\ s^{-1}$.

The flux measurement was also taken during the SiC target but yielded a lower flux than previously seen, $1 \pm 1 * 10^{23}\ ions\ m^{-2}\ s^{-1}$ but this could be due to a destroyed probe causing the area to change and the flux not being reported accurately.

The DLPs will be used to get the ion flux using their measured plasma density and temperature given their agreement with Thomson scattering and the target probes. The fact that the 13-magnetic spool configuration has the DLP in the same spool as Thomson and the target will lead to increased confidence in the target ion flux reported.

3.4.3 Ion Temperature

Proto-MPEX uses the Doppler broadening of a 10% argon seeded impurity plasma to measure ion temperatures. The McPherson spectrometer is used to collect the AR II transition line for fitting. The fitting process for determining the ion temperature is discussed by Beers et al.[62]. The plasma ion Ar II transitions from ${}^4P^o_{5/2}$ to state ${}^4P_{5/2}$ gives off light of wavelength 480.6 nm and is a transition that happens due to it being and ionized plasma ion. Measuring this spectral line at various locations, times, and with varied power levels can be done to understand the coupling location of the ICH to the plasma, the ion temperature, and the change in temperature along the axis of Proto-MPEX. The Doppler broadening of the Ar II line changes as the ion temperature changes; the wider the peak the higher the ion

temperature. The magnetic field can also cause broadening or splitting of the line, but this is removed by use of a polarization filter on the light collection optics. The spectrometer itself also has an instrument function that has been measured by using a "cold" Ar pen lamp for calibrations. It being "cold" gives the smallest detectable spectral width of a peak of interest. This width is the room temperature ion temperature and any width increase over this point is an ion temperature increase from room temperature. The spectra are fit to a Gaussian and the ion temperature determined from:

$$kT_{ArII} = \frac{mc^2}{8ln(2)e}\frac{FWHM}{\lambda^2} \tag{3.2}$$

where m is the mass of the Ar II ion, c is the speed of light, e is the charge of the electron, k is the center wavelength of the transition (480.6 nm), FWHM is the full width half maximum of the Gaussian function, and the ion temperature, kT_{ArII}, is in units of eV. A theoretical spectrum is also created and the χ value between the two profiles is calculated. The temperature is chosen when the minimum χ is achieved.

The ICH has seen an increase in T_i to 8-10 eV but combined heating with ECH and ICH has seen temperatures of up to 15 eV at the plasma core near the target. These conditions have been measured with the external ICH antenna that allowed for 6.5 MHz operations. The previous operations on the internal ICH antenna were done at 7.5 or 8.5 MHz when the graphite target was in and lower temperatures were measured in the core (4 eV) due to predominately an edge heated plasma (8-12 eV).

The effects of the material target on the measured ion temperature at the target is still being studied. The effect is speculated to be due the reflection energy coefficient where light elements will reflect off high-z materials keeping more of their energy and low-z materials will have more energy transferred to it. This leads to a lower energy distribution in front of the target for lower-z materials compared to higher-z ones. Graphite also has H/D adhesion where H/D would not stick to stainless-steel or tungsten.

3.4.4 Heat Fluxes and Target Temperature

The heat flux is a function of the change in temperature via:

$$q = C_p * m * \Delta T \tag{3.3}$$

where q $[W]$ is the power to the measured surface or in standard units of MWm^{-2} for heat flux, C_p $[J/kg * K]$ is the specific heat capacity of the material, and ΔT $[K/s]$ is the change in temperature measured between IR frames. This value has been modeled for Proto-MPEX using the code THermal Energy Onto DivertOR (THEODOR) [81, 82] and the multi-physics simulation package COMSOL [83]. THEODOR was created at the Max Planck Institutde for Plasma Physics in Garching, Germany for determination of heat fluxes from IR thermography. The code was modified to work with Proto-MPEX's geometry and experimental inputs which have been compared to COMSOL simulations of the target heat flux. These have given good agreement of $\sim 1 - 1.5 MWm^{-2}$ for helicon only data and have seen up to $5MWm^{-2}$ with auxiliary heating. These auxiliary heating heat fluxes are typically for short time durations (≤ 100 ms) leading to difficulty in larger fluence accumulations on Proto-MPEX while at a high heat flux.

The heat flux can be compared to a calculated heat flux from DLP density and temperature data via:

$$q = \gamma_i * \Gamma_i * T_i \ + \ \gamma_e * \Gamma_e * T_e \tag{3.4}$$

where the particle flux, Γ, assuming the ion and electron flux is equal is given by:

$$\Gamma_e = \Gamma_i = \frac{n_e}{2} * \sqrt{\frac{\gamma_e * k_b * T_e}{m_i}} \tag{3.5}$$

where γ_e *and* γ_e is the sheath heat transfer coefficient for electrons and ion at 5.5 and 1.5, respectively [9].

Equations 3.3 and 3.4 with 3.5 give a way to use the DLP to derive a heat flux value to compare to the IR camera's for calibration and creation of a 2D ion flux map to go along with the calculated heat fluxes from the IR images using Equation 3.3. The 3D heat

transfer through the thin stainless-steel target has been done in COMSOL and shows no time dependence for thermal diffusion through the thin target plates.

3.5 Surface Characterization Diagnostics

Many surface characterization diagnostics are available for use at ORNL and those that were used are given below. The diagnostics used within this work were performed ex-situ.

3.5.1 Profilometry

A Mitutoyo SJ-310 surface roughness tester with both a standard drive unit and a transverse tracing drive are used to measure surface roughness [84]. The profilometer has a resolution that is defined by using a standard with 1 μm surface roughness. The length of the measurement also defines the resolution where a 360 μm range has a resolution of .8 μm. After the calibration profile is created and saved each subsequent measurement uses the profile to calculate the surface roughness. The standard drive pulls the needle into the drive unit allowing for a parallel measurement and the transverse unit moves it perpendicular to the unit. The standard drive is useful for measuring inside a curved surface and the transverse unit is useful for across the face of a metal target. The profilometer has a digital readout which can display either the average surface roughness, R_a, or the profile height, P_a. The maximum length of the scan is 5.7 mm and the full profile readout can be seen on the digital output.

3.5.2 Scanning Electron Microscopes

ORNL has several scanning electron microscopes (SEMs), some with energy-dispersive X-ray spectroscopy (EDS). A Hitachi S-4800 scanning electron microscope (SEM) with an Ametek Octane Elect EDS System for measuring surface elemental concentrations is used for taking many of the high resolution images used in this work [85]. SEM is done with an electron beam being moved over the sample of interest for imaging. The electron beam interacts with the sample at a depth of a few micron to produce secondary electrons,

back-scattered electrons, and characteristic X-rays. Detectors around the sample collect the electrons that come from the interactions and produce an image via software. EDS is the collection of the x-rays that are produced from the electron beam on the sample. The X-rays are characteristic which mean they have an energy based on the element that the electron interacted with. The electron knocks an inner shell electron out and a higher state electron moves in to take the place of the knocked-out electron. Energy in the form of an X-ray is emitted during this process. X-ray detectors around the sample collect them and give the composition of the material based on the energy of the collected x-ray. Due to the scanning of the electron beam a composition map can be created from data reconstruction in software.

3.5.3 X-ray Photoelectron spectroscopy

X-Ray photoelectron spectroscopy (XPS) is another material composition technique used. The signal from XPS is more near surface (the first 1-10 nm) than EDS which allows for composition profiling if an ion sputtering tool is used to remove the surface layer and take additional XPS profiles. An x-ray source is used to expose the material of interest to an x-ray beam which produces an electron. The energy of the electron depends on the energy of the x-ray beam and the binding energy of the electron. Detectors for the electrons measure the energy which is then matched to the element for which that energy is given from. For each peak and the corresponding element the area under the peak is measured and normalized using tabulated sensitivity factors [86] which are either looked up or incorporated into the software used for analysis. The composition in atomic percentage (at.%) is achieved by taking the normalized area under the curve divided by the total normalized area under all curves for a single XPS spectra. The x-ray beam is not scanned and thus a small spot size is used to get the total composition in a small area. A Thermo Scientific K-Alpha model was used for the XPS data in this work [87]. An Ar ion gun is also used on the XPS setup to mill the surface to get depth profiles. A SiO_2 sputtering rate is assumed for all depths given. Measurement errors come from counting statistics which are indicated by the plotted line thickness in the XPS spectra and the sputtering rate of the material not being SiO_2.

Chapter 4

Experimental Characterization of Impurity Generation, Transport, and Deposition in Proto-MPEX

4.1 Proto-MPEX Impurity Deposition on Target Observations

Performing clean experiments in Proto-MPEX requires an understanding of the impurity movement within the device and how much would be accumulating on the target which is ideally zero. To first investigate impurity accumulation on the target a 99.9% pure Mo target in the design of the MAPP metal target was exposed to a pure deuterium plasma for 22 consecutive shots having a flux and total fluence of $2.8 * 10^{23}\ m^{-2}\ s^{-1}$ and $6.25 * 10^{24}\ m^{-2}$, respectively. The Mo sample was in the as-received state for exposure which did not include any heat treatment or sample polishing. This exposure had no Langmuir probes in the plasma during the exposure. The exposed Mo sample and locations where EDS were performed is shown in Figure 4.1. The TZM top covers were not in place for this exposure thus the discoloration pattern occured across the whole sample. The results from the EDS are given in Table 4.1. The main impurity elements at every location are aluminum (Al) and oxygen (O). It is expected that the surface will have an oxide layer of 10-20 nm thick but the

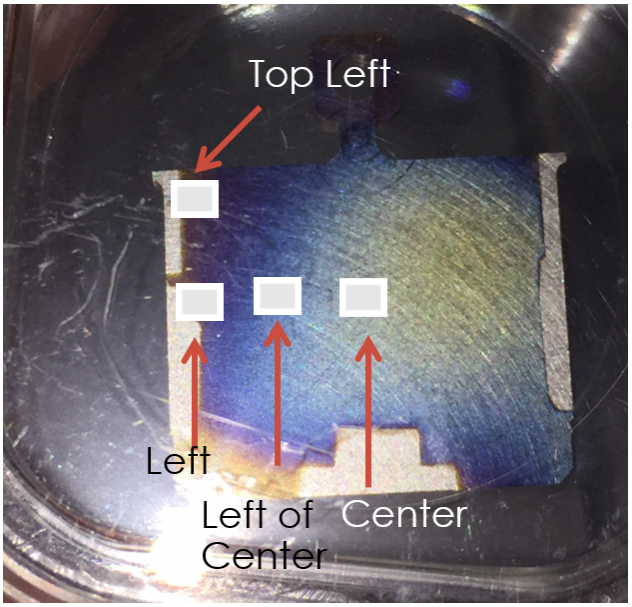


Figure 4.1: A Mo sample exposed to fluence of $6.25 * 10^{24}$ m^{-2} to understand impurities on the target. White boxes with labels denote where EDS was performed and the name of the location for further reference.

Table 4.1: EDS results from the four locations depicted on Figure 4.1. Elements are given in atomic percents. Chosen elements were first picked by best fit from the software but undefined peaks were added by hand (Fe and Cr).

Element At.%	O	Al	Si	Mo	Cr	Fe
Center Location	61.31	6.39	1.61	28.87	0.5	1.31
Left of Center Location	58.61	4.71	1.41	33.85	0.39	1.03
Left Side Location	48.67	3.10	1.03	46.16	0.32	0.72
Top Left Location	54.03	4.31	1.24	39.15	0.34	0.93

aluminum was unexpected. The iron (Fe) and chromium (Cr) is likely from stainless-steel but one would also expect to see nickel (Ni) present. The Si may be from basic sample polishing done at the manufacturing company. These results show that there could be a problem with future exposures and additional experiments are needed.

4.1.1 W coated Mo Exposure

An additional Mo MAPP target was sent to have an ion beam assisted deposition layer of W applied to it. This layer was 0.5 - 1 μm thick of natural W. This sample had no additional polishing other than from the deposition process. This sample was to be used in the MAPP target holder and have a He plasma with ECH, for getting the ion impact energies up to 50 eV, and IR imaging to get the surface temperature to achieve the W fuzz growth regime in Proto-MPEX. The target wasn't heated as the heating element and backing plate were damaged with the first experiment thus only the plasma heating was used to heat the target. The IR camera for viewing this was used at the Spool 12.5 location to view the front of the target. The view only saw the edge of the plasma due to the MAPP needed to be moved away from the large tungsten (W) plate target already in Proto-MPEX. The mirrors in vessel are aligned such that the IR camera is focused to one target location and moving the MAPP forward loses the center of the target focusing. The thermocouple that touches the target also was not used during this exposure due to being damaged. The gas mixture was set to be a 25% He - remainder D_2 for the exposure. Prior experiments to optimize He plasmas showed that a pure He plasma had lower than desired densities ($5 - 15 * 10^{18}\ m^{-3}$) for each of the varied gas puff and magnetic field conditions. This led to a second experiment using a He and D_2 gas mixture first at 25/75 He to D_2 and then at 50/50. The helicon was able to produce a high-density plasma with the 25/75 mixture at $5 - 8 * 10^{19}\ m^{-3}$ and the 50/50 mixture showed a reduced density at $1 - 2 * 10^{19}\ m^{-3}$. The electron temperatures were around 5 and 10 eV for the 25/75 and 50/50 mixtures, respectively, which is hotter than the usually seen 2-3 eV for helicon only plasmas. The higher electron temperature than from helicon only operations indicates that the He was also being ionized and not just D_2, but the ionization fraction is unknown. For the W coated Mo experiment the 25/75 gas mixture was used. Using this gas mixture, it is assumed that the He ion flux is 25% of the total measured

ion flux measured by the DLP (the DLP fitting routine's particle mass was adjusted to 2.5 amu from 2 amu to reflect the gas mixture ratio). The ECH pulse, however, does change the plasma density and temperature by lowing the density and increasing the temperature. The flux during the ECH pulse comes out to be $4 * 10^{23}\ m^{-2}s^{-1}$ which is useful in its own but the He flux is 25% of the total flux. The ECH pulse was also worked up to a 410 ms pulse length starting from 70 ms while the total helicon pulse length was kept at 1 s. This gives a He fluence during the ECH of $1.4 * 10^{24}\ m^{-2}$ and a total He fluence of $9.5 * 10^{24}\ m^{-2}$. The total H fluence was $2.8 * 10^{25}\ m^{-2}$. This fluence was accumulated over 62 pulses over two days. The 1 second pulse length requires about an 8-minute wait between shots to let the helicon window cool down. The uncooled helicon window is the limiting factor in pulse repetition rate currently. During the ECH pulses the ion temperature was measured to be 10-12 eV directly in front of the target and the electron temperature was 5 eV giving an ion impact energy of 35 eV.

Figure 4.2 shows the exposed W coated Mo sample along with the locations of SEM analysis locations in the yellow boxes. The grey areas are the unexposed regions while the darkened area is the exposed region which is indicative of a more textured surface. Figure 4.3 shows the SEM images of the unexposed and exposed areas of the W coated Mo sample. The exposed region shows a coarsening and enlargement of surface features, which matches with the surface color darkening. The surface roughening may because of He blister formation and rupture as described previously. It is not believed to be delamination of the W coating due to the size of the textured surface being 10 x smaller than the coating thickness. This coarse top layer has the same composition as was seen on the pure Mo sample indicating that Al impurities will be present on any exposures. The overarching research questions derived from this observation are where is the the source of the impurities and what is the transport of the impurities. An investigation to understand the impurity creation process and transport process was performed.

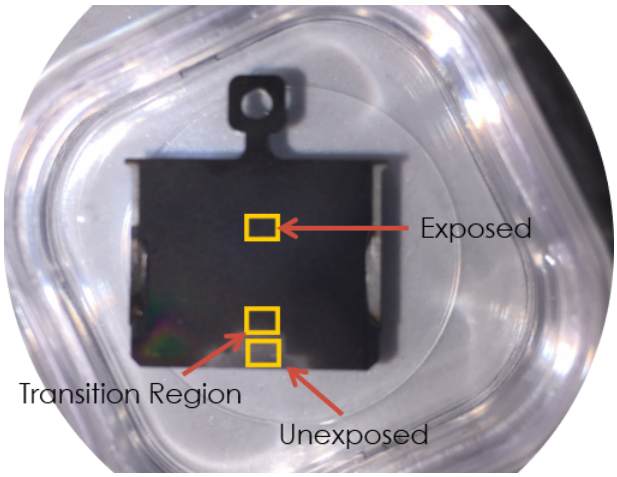


Figure 4.2: Mo target with an ion beam assisted deposition layer of 0.5 - 1 μm natural W after exposure to Proto-MPEX ECH plasmas (see text for exposure conditions). Blackening of the exposed area can be seen indicating texture changes on the sample surface. Three regions were SEM was done are shown by the yellow boxes, each with their respective labels.

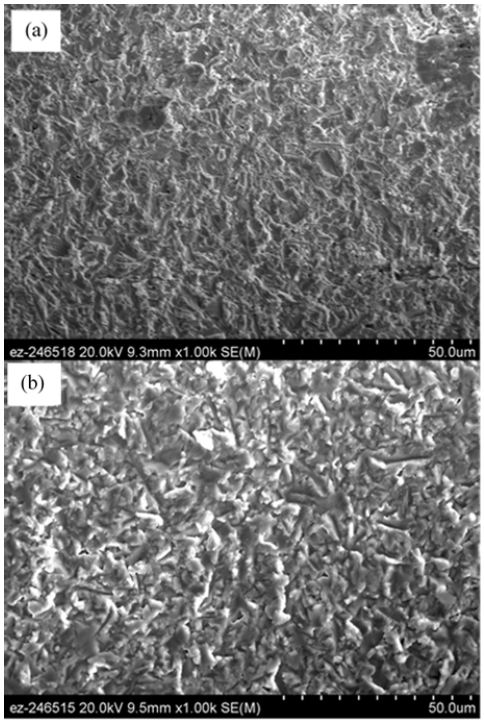


Figure 4.3: SEM results from the (a) unexposed and (b) exposed sections of a W coated Mo sample shown in Figure 4.2.

4.1.2 Helicon Window Observations

To look for additional locations of deposition the AlN helicon window was taken out and a deposition pattern was observed. Figure 4.4 shows the deposition pattern observed. Two main regions of deposition can be seen in the center of the window.

4.1.3 Pure W Samples

75 pure W samples of 99.95 % have been produced from Midwest Tungsten Service in the design of the MAPP metal target. The material composition in atomic percent is 0.0020% Fe and N_2, 0.001% Al, Ni, Si, and C, and 0.005% O_2 with remainder W. 25 of the samples are polished to a mirror finish on one side down to 0.5 micron colloidal silica and finished with a light relief polish. The other 50 W samples were left unpolished to be exposed in the as-received state. These W samples are used for the remainder of the experiments within this work.

4.2 Impurity Production Location

Based on the observation of the target impurity concentration and the helicon window deposition it is hypothesized that the impurities are coming from the helicon window. Experiments are performed to understand the impurity production and transport within Proto-MPEX.

4.2.1 Helicon Region

The helicon window is made of AlN and would be the most likely source for the aluminum. To understand the location of the impurity source an experiment of varied limiting location was performed with pure W MAPP targets in for impurity collection. The limiting location in Proto-MPEX is defined as the ending location of the LUFS that is not the target. Figure 4.5 shows the helicon region where 3 limiting locations were chosen: the helicon window limiting with black LUFS, the MPEX-like limiter (red box) with red LUFS, and the upstream limiting

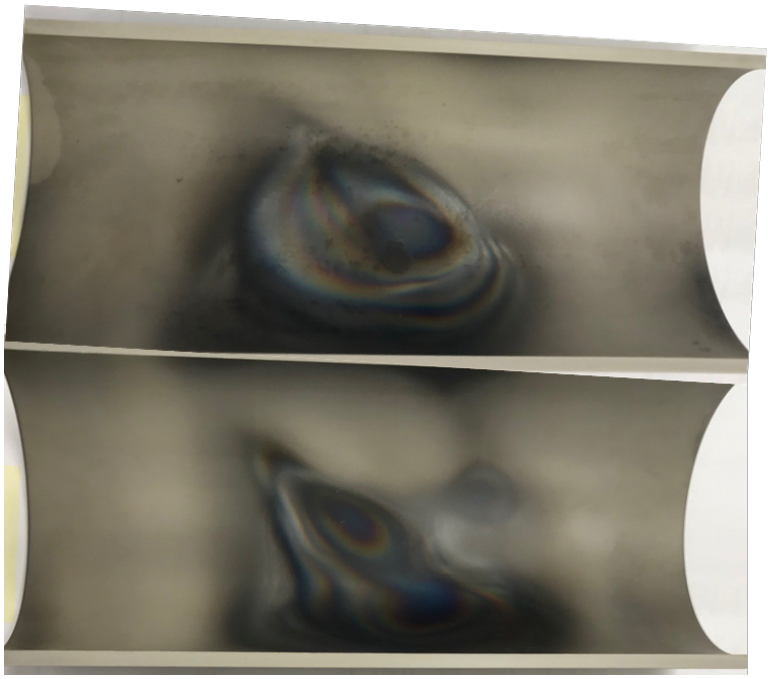


Figure 4.4: The AlN helicon window cut in half showing two main regions of deposition.

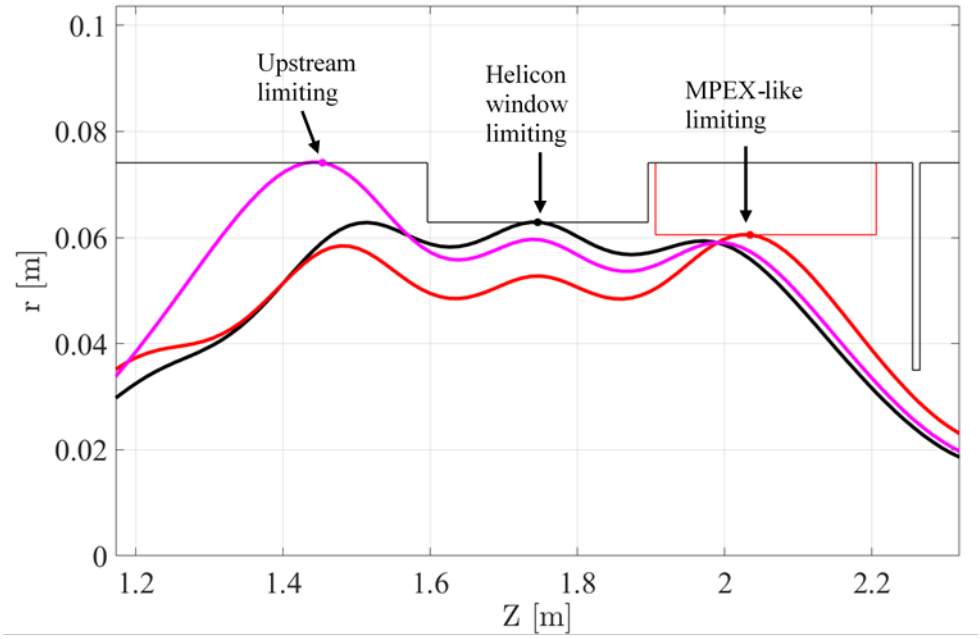


Figure 4.5: The last uninterrupted flux surface in Proto-MPEX for the helicon window limiting in black, downstream limiting on a stainless-steel MPEX-like limiter in red, and upstream on the stainless-steel vacuum vessel in magenta.

with magenta LUFS. The window limiting configuration is the condition that Proto-MPEX has used for all but one prior campaign. The MPEX-like limiter case requires the helicon magnetic field to be ramped from starting at the helicon window limiting and moving to the MPEX-like limiter limiting over the first 80 ms of the pulse. This ramping is to keep the helicon in helicon mode while allowing for a higher field underneath the helicon. The vacuum vessel limiting case (towards the dump side of the device) is referred here as upstream limiting and does not require a magnetic field ramp to reach. The main case of interest within this work will be the helicon window limiting as it was the majority of the campaigns used within Proto-MPEX but the MPEX-like limiter will be the case that MPEX will use. The experimental conditions used for the helicon window limit, MPEX-like limit, and the upstream limit are given in Table 4.2. Each exposure used 90 kW of helicon power. The DLP data was taken before the MAPP targets were installed as to not have an additional source of contamination and the conditions with the MAPP targets in are assumed to be the same as the Proto-MPEX plasma pulses were repeatable. The flux per shot is the averaged deuterium ion flux over a single plasma pulse but the total fluence is the deuterium fluence over the entire exposure of a single target. To get the composition and thickness of the deposition layer on the MAPP W targets, XPS depth profiles were taken. The depth profiles were performed by using an Ar ion beam to mill the surface after collecting XPS profiles. The XPS data and subsequent Ar ion beam milling was performed until the XPS profiles were prominently a W signal. The exposed sample for the helicon window limiting location and the location of the XPS depth profile are shown in Figure 4.6. Each limiting location had a XPS depth profile taken as the same location and the XPS data for the three limiting locations is shown in Figure 4.7 along with zoomed in plots of the stainless-steel and N components seen on the samples for the helicon and MPEX-like limiting cases. The depth markers are the location where the O and W signals cross indicating reaching the bulk. Each XPS depth profile shows a high O concentration that is consistent throughout the layer thickness. This consistency indicates that the O is present during the exposure within the device and is not an only near surface effect that occurs when the sample is exposed to air. The fact that the O signal drops-off when reaching the bulk also indicates that the XPS

Table 4.2: Proto-MPEX sample exposure conditions and plasma parameters near the target for the AlN helicon window limiting, upstream limiting, and MPEX-like limiter limiting cases.

Plasma parameter/Exposure condition	**Helicon Window Limit**	**MPEX-like Limit**	**Upstream Limit**
Target material	W	W	W
Gas species	D_2	D_2	D_2
Pulse length [s]	0.5	0.5	0.5
Number of pulses	8	10	9
T_e $[eV]$	2.5	1.6	2.4
n_e $[m^{-3}]$	$4.8 * 10^{19}$	$5.2 * 10^{19}$	$2.5 * 10^{19}$
Flux per shot $[m^{-2}s^{-1}]$	$4.3 * 10^{23}$	$3.7 * 10^{23}$	$2.3 * 10^{23}$
Total fluence $[m^{-2}]$	$2.3 * 10^{24}$	$2.4 * 10^{24}$	$1.3 * 10^{24}$

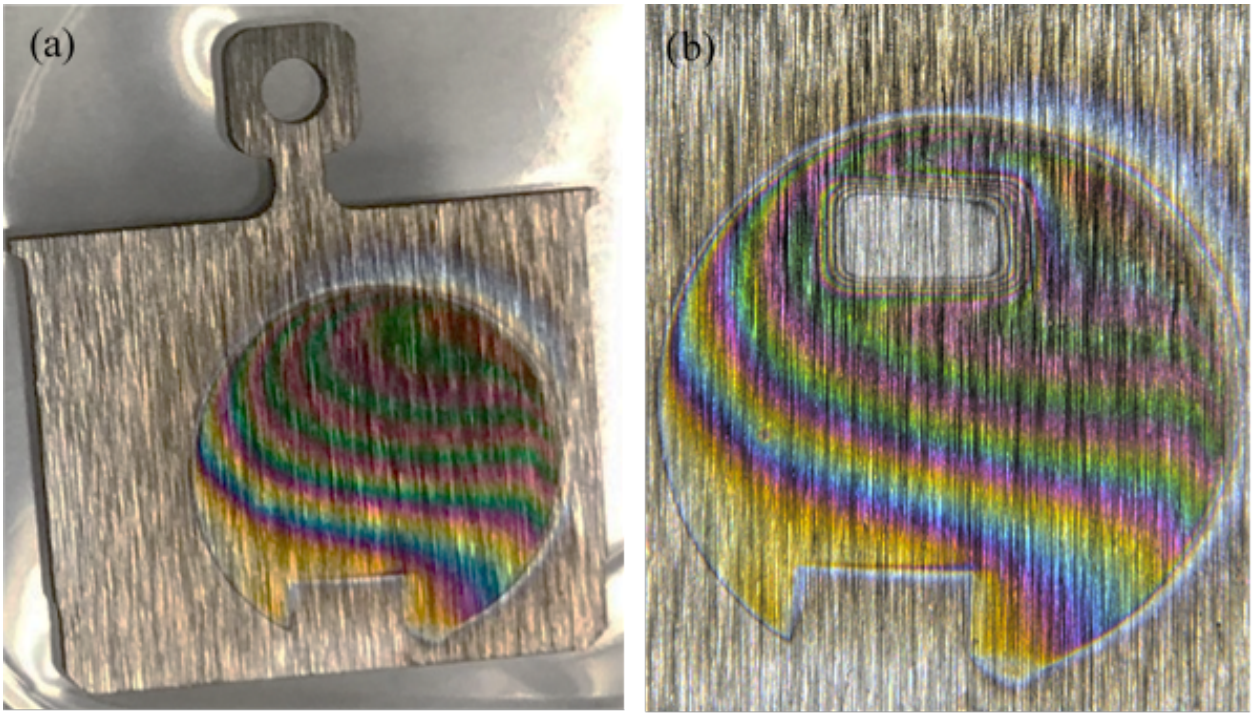


Figure 4.6: The exposed W sample for the AlN helicon window limiting case showing (a) the discoloration pattern on the sample which is under the TZM top cover and (b) the target in (a) after Ar ion beam milling and XPS depth profiling. The indicated depths are the crossover points for the O and W signals.

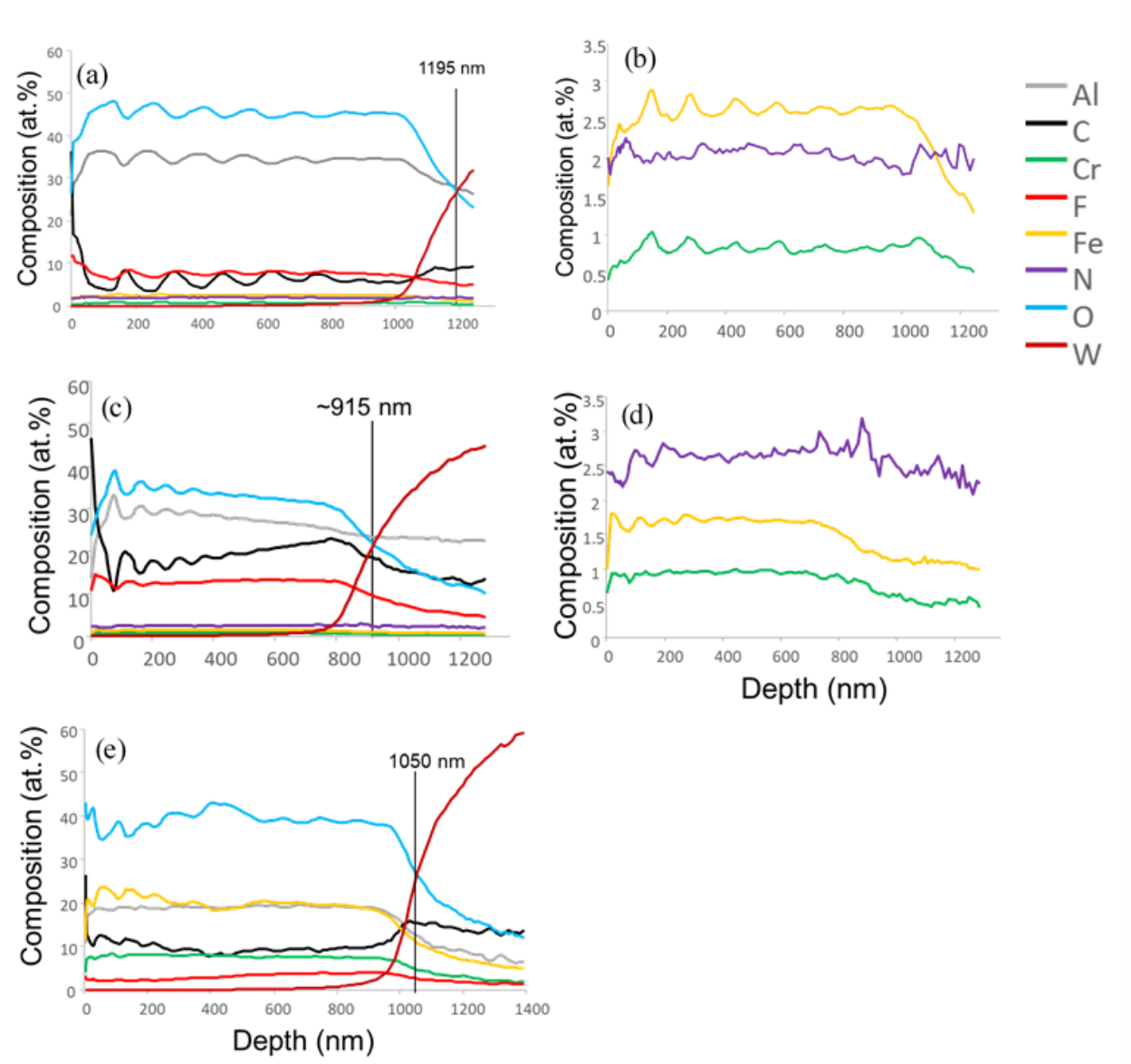


Figure 4.7: XPS depth profiles for (a) the helicon window limiting location exposure, (b) the zoomed in stainless-steel and N components from (a), (c) the MPEX-like limiter location exposure, (d), the zoomed in stainless-steel and N components from (d), and (e) the upstream vacuum vessel limiting location exposure. The indicated depths are the crossover points for the O and W signals. The standard error of the composition profiles are less than 1%.

system is not introducing O onto the surface. The standard error of all presented XPS composition profiles are less than 1%. Proto-MPEX does not bake, and any air or water leak could lead to water vapor dissociating and O being in the plasma. The stainless-steel components (Fe and Cr here, Ni was not measured) being present during the helicon limiting exposure is due to the flanges used to hold the helicon window in place and the fluorine (F) is from the Teflon O-rings used between the helicon flanges and the window. The Fe component likely goes down from the helicon window limiting to the MPEX-like limiter case due to the ramping of the helicon field during the short pulse which reduces the heat and particle flux that any one location receives. The helicon ramping up and down are not negligible lengths for the 0.5 s pulse and likely leads to the reduction in Fe concentration. The MPEX-like limiting case has a higher than usual C concentration which is likely due to this exposure being the first one with this stainless-steel limiter and the C coming from manufacturing. The carbon may also come from pump oils from the floor pumps that back the turbo pumps. The stainless-steel components do increase, and the Al and F decreases for the upstream limiting case which do not have a helicon magnetic field ramp indicating that the limiting location does have a direct impact on what impurities make their way to the target. The thickness of the layer does not change significantly for any of the conditions which is not expected as the upstream limiting case had 55% of the total fluence.

An additional experiment with a different helicon window was done to give further confidence in the impurity source location. A silicon nitride (Si_3N_4) helicon window was installed along with keeping the same MPEX-like stainless-steel limiter installed for testing. The Si_3N_4 window is the chosen helicon window material for MPEX for its critical stress values, thermal conductivity, and compatibility with helicon window coolant options. The exposure conditions are for the Si_3N_4 window exposure with a MAPP pure W target are given in Table 4.3. Here 90 kW of helicon power was used. The limiting location was the MPEX-like limiter for this experiment for wanting to test the conditions for MPEX. The XPS depth profile is shown in Figure 4.8 which shows O still present and Si being the now predominate impurity on the target. A new limiter was installed along with the Si_3N_4 window so the possibility of Si migrating to the limiter which would then be transported

Table 4.3: Proto-MPEX sample exposure conditions and plasma parameters near the target for the MPEX-like limiting case with the Si_3N_4 helicon window.

Plasma parameter/Exposure condition	**MPEX-like limiter with Si_3N_4 window**
Target material	W
Gas species	D_2
Pulse length [s]	0.5
Number of pulses	25
T_e $[eV]$	2.3
n_e $[m^{-3}]$	$7.6 * 10^{18}$
Flux per shot $[m^{-2}s^{-1}]$	$7.8 * 10^{22}$
Total fluence $[m^{-2}]$	$1 * 10^{24}$

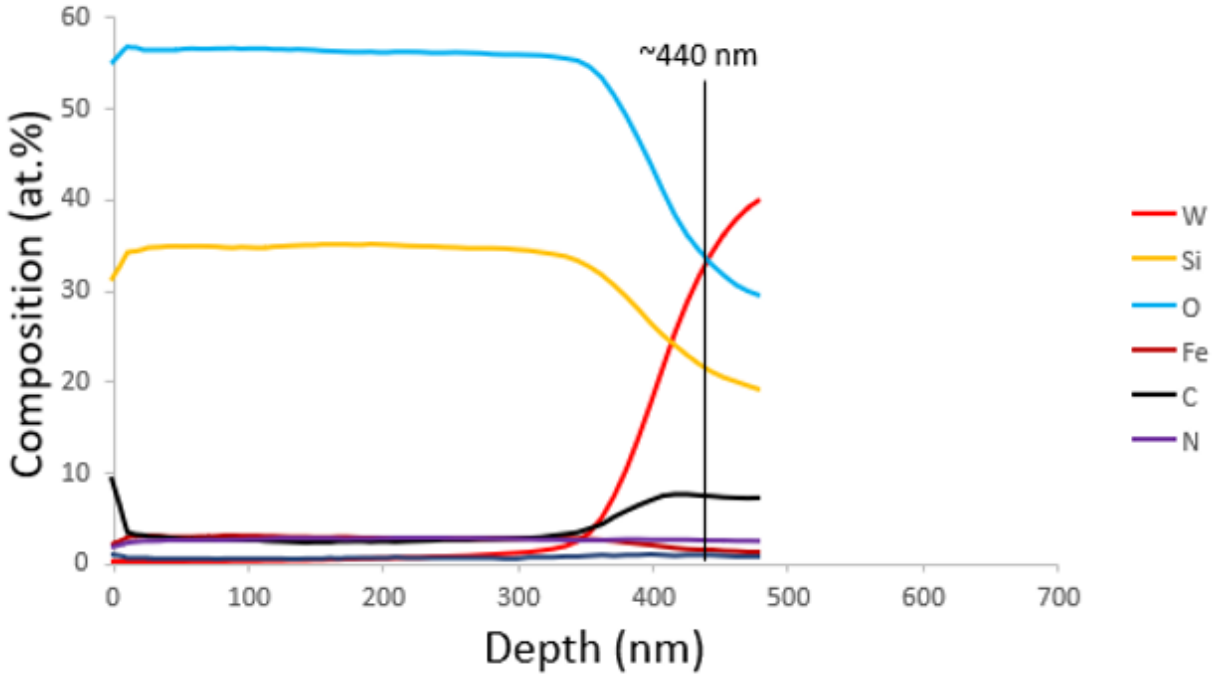


Figure 4.8: XPS depth profiles for the MPEX-like limiting condition with a Si_3N_4 helicon window. The indicated depth is the crossover point for the O and W signals. The standard error of the composition profiles are less than 1%.

in a two-stage process to go to the target after going to the limiter is still plausible. No observed Al on the target also indicates that the Al is not coming from elsewhere within the device. The helicon magnetic field ramping was also used for this exposure which could mean that the start of the plasma pulse which starts with the limiting location being the helicon window and moving to limiting on the MPEX-like limiter could contribute to a portion of the created impurities. This exposure also verifies that the helicon window is the source of the impurities occurring within Proto-MPEX. The O-ring used was not exposed with the new stainless-steel flange holding the Si_3N_4 helicon window which is why no F is present. The larger carbon concentration that was present on the first MPEX-like exposure is also reduced after the first exposures indicating that the carbon was indeed only on the surface and was cleaned off after the first exposures.

While the Si_3N_4 window was in Proto-MPEX the AlN window underwent analysis to compare to the exposed pure W MAPP targets. The window was first cut in half to be imaged. The view of the inner diameter of the exposed AlN helicon window is shown in Figure 4.9. The helicon antenna is overlayed on the image for reference. Where the antenna is located around the helicon window appears to be clean and areas between the helicon antenna location is darkened. The bottom half section was further sectioned into 0.02 x 0.04 m pieces to fit into the SEM for XPS depth profile analysis. Figure 4.10 shows the XPS depth profile taken for the darkest spot of the discolored region. The depth profile concentrations match that of the exposed pure W MAPP targets for the AlN helicon window limiting condition. The data suggests that the helicon window is eroding under the helicon antenna and redepositing between the antenna straps and making its way into the plasma and to the target. This further indicates the AlN helicon window was the source of Al impurities. The pattern on the inner diameter of the helicon window indicates that the RF is sputtering the window likely due to an RF induced sheath which enhances sputtering. Profilometry measurements were done across the helicon window discolored regions and on the blister-like spot from the top half of Figure 4.9. Figure 4.11 shows a 0.0057 m profilometry scan across the edge of the blister-like region from on the blister to off the blister. The location shows a jump at the edge of the region versus the rest of the scan indicating that a large, localized deposition happened which flaked off sometime during operations.

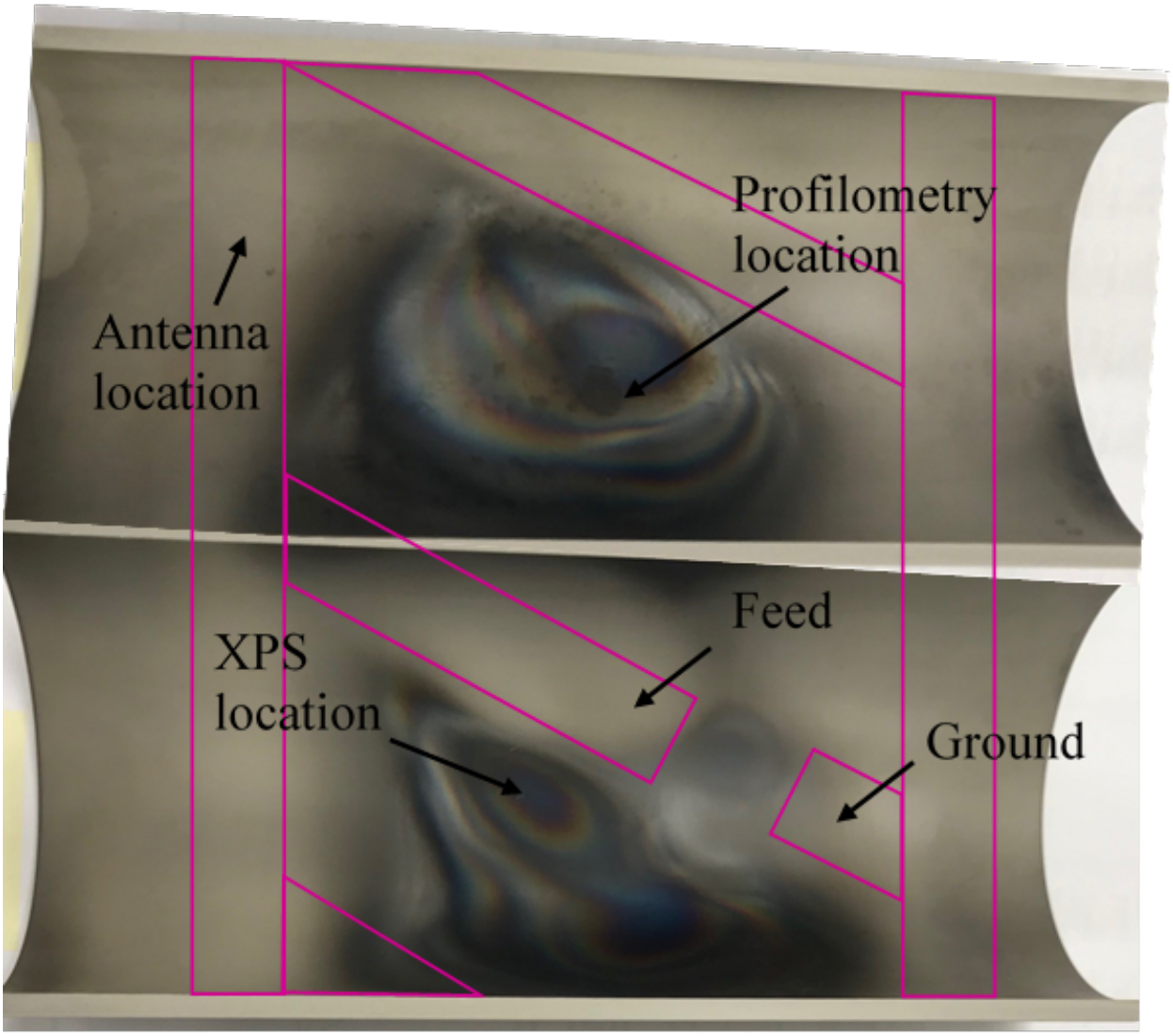


Figure 4.9: The exposed inner diameter of the AlN helicon window with the helicon antenna pattern overlayed in magenta. The locations of the power feed and ground on the antenna are shown along with the location of the XPS taken on the window shown in Figure 4.10 and the profilometry location that is shown in Figure 4.11

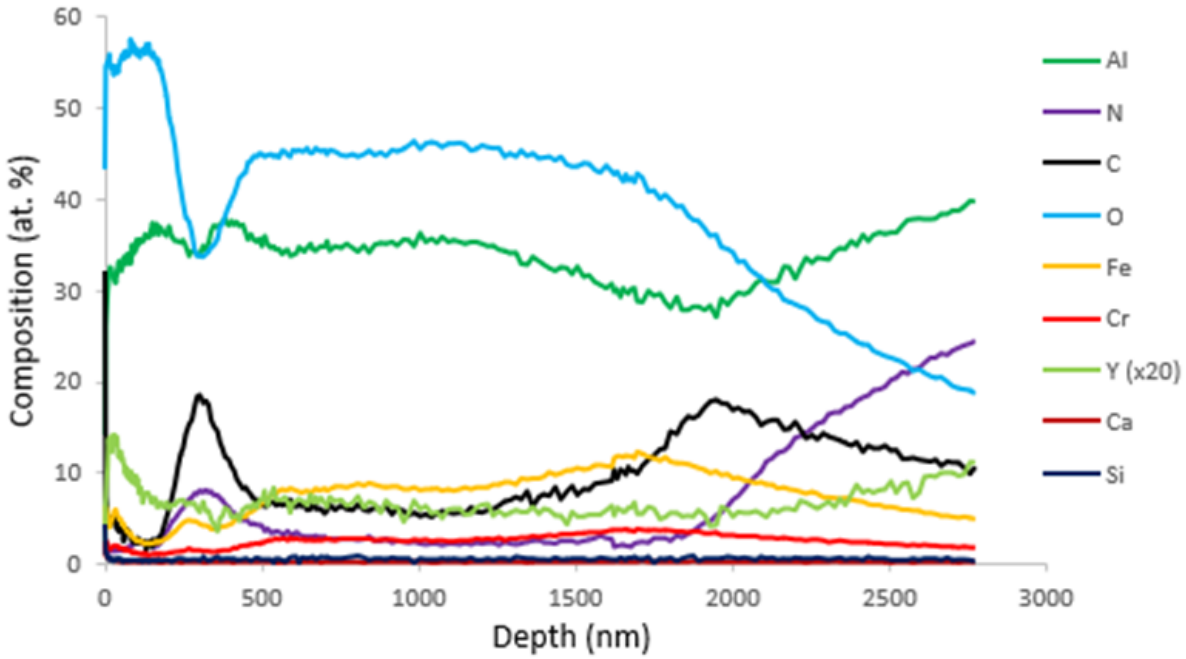


Figure 4.10: XPS depth profile from the exposed AlN helicon window. The standard error of the composition profiles are less than 1%.

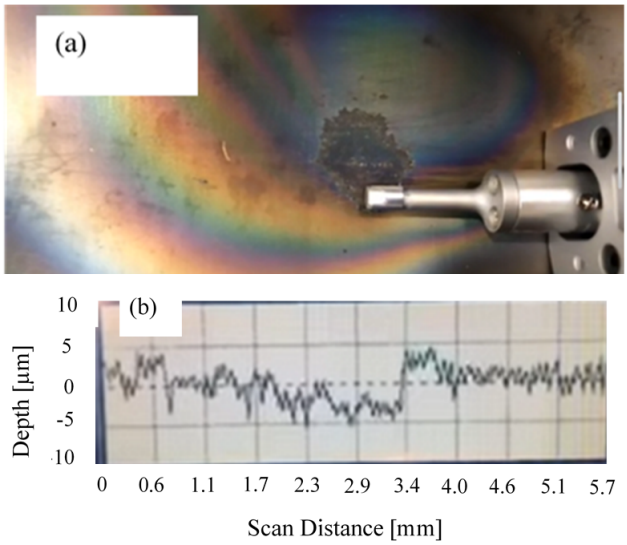


Figure 4.11: Profilometry measurements showing (a) the "blister"-like surface feature and profilometer scanning tip and (b) the profilometry measurement showing the measured surface depth over the 5.7 mm scan with the edge of the region at 3.4 mm indicating a jump in height.

4.3 Experiments on Impurity Source Characterization

Some of the previously shown exposure's XPS depth profiles showed little change in thickness while having a large difference in fluence indicating that different times during the plasma pulse might be contributing more to the impurity production than others. The hypothesis is that the beginning of the pulse contributes to most of the impurity creation. A capacitive probe measurement was done to measure the RF potential at the edge of the plasma (0.04 m off axis) at Z=2.75 m. The capacitive probe data is shown in Figure 4.12 for Proto-MPEX plasma pulse 31439. The black trace is the helicon power timing for 90 kW of peak power. A spike in the RF potential can be seen at the beginning of the pulse which then falls off and rises again throughout the pulse. This would indicate that the beginning of the pulse contributes to a higher RF sheath potential and indicates that the RF sheath is likely driving the sputtering of the helicon window through physical sputtering. Here we perform experiments to determine the primary timing during the pulse for the impurity generation.

4.3.1 Temporal Evolution

To give more information about the timing of the pulse that leads to the most impurity production a fluence scan was performed with single plasma pulses on pure W MAPP exposures to map the change in impurity layer thickness. The deuterium fluence scan results are shown in Figure 4.13. The impurity layer thickness has a slope change as the pulse gets over 238 ms. This time is much longer than the spike at the beginning of the pulse seen by the capacitive probe but the coarseness of the fluence scan may not capture the exact slope change location. The lower slope for the longer pulses matches the trend of the change in RF potential from the capacitive probe from the start of the pulse to the rest of the pulse.

Shutter Experiments

To reduce the role of the impurities at the start of the plasma pulse a shutter was installed in Proto-MPEX to be compatible with the MAPP target. The hypothesis that the impurities can be eliminated using a shutter to block impurities from getting to the target is tested

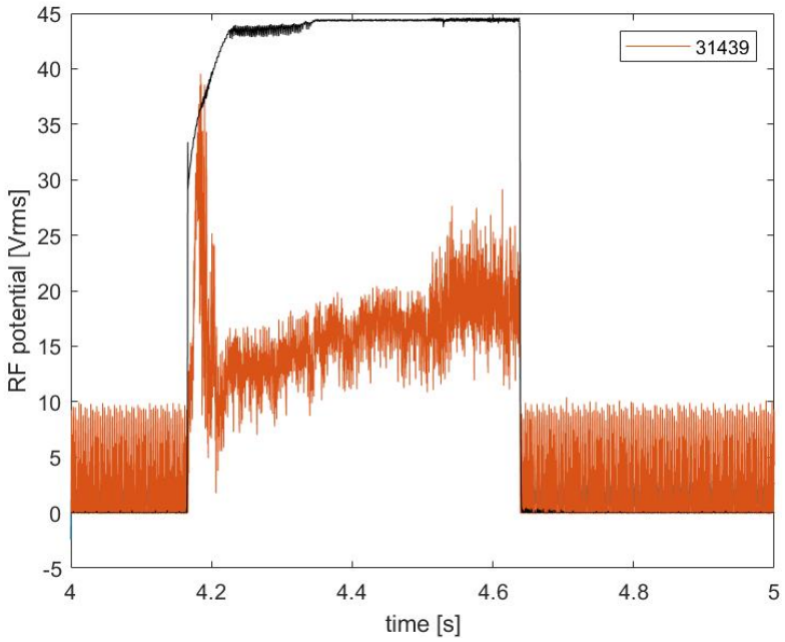


Figure 4.12: The RF potential measured by the capacitive probe at Z=2.75 m for Proto-MPEX plasma shot 31439. The probe was 0.04 m off axis for the measurement. The Si_3N_4 helicon window was in during this measurement and the black trace is represents the timing of the helicon RF pulse.

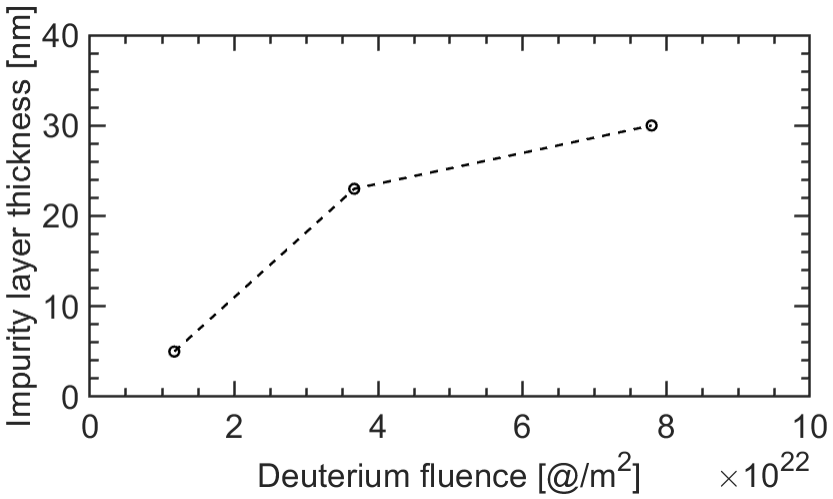


Figure 4.13: The thickness of the impurity layer, taken as the crossover point for the O and W, for exposure length of 137, 238, and 383 ms, respectively. The helicon window was Si_3N_4 for these exposures and the limiting location was the MPEX-like limiter.

here. The shutter was a W plate on a rod that was actuated by a solenoid. The shutter would block the plasma from reaching the MAPP target until activated. The timing for the shutter to be opened (not blocking plasma) was from 4.3 to 4.5 s. A comparison exposure was also done for the same plasma conditions with the shutter open for the whole plasma pulse. Table 4.4 gives the experimental conditions for the shutter experiment. The Si_3N_4 helicon window was in for these exposures and the helicon power was 90 kW. XPS depth profiles for the with and without shutter exposures are given in Figure 4.14. The XPS depth profiles show a 4.3 nm per $1 * 10^{22}$ m^{-2} for the without shutter exposure and a 2.9 nm per $1 * 10^{22}$ m^{-2} impurity deposition rate for the with shutter exposure. The data shows that the start of the pulse does not contribute to significantly more impurity production than the steady state time period of the pulse for the same fluence. The shortest pulse would need to be a much more than a few nm of deposition when compared to the longer pulses. In this scenario a shutter would not help to eliminate impurities on the target. However, if a two-stage process is occurring where the sputtered material is moving to the limiter then the target, then a shutter would help to eliminate the starting impurities.

4.3.2 Proto-MPEX Baking

The O is expected to play a large role in the impurity generation due to it being a heavier particle than D so an experiment was performed to reduce the O in the machine. The O is hypothesized to come from water vapor and reducing the water vapor is hypothesized to reduce the impurities created. To reduce the water vapor in the machine, and ultimately reduce the amount of O seen on the target samples, Proto-MPEX had heating tapes wrapped around the upstream dump region, either side of the helicon, the chamber at Z=2.75m, and the target area. The heating systems were on during normal business hours for two weeks and got up to a maximum of 130°. Using a residual gas energy analyzer at Z=1.25 m before the baking the water vapor concentration was 30% of the base pressure and went to 35% of the base pressure after baking. However, the base pressure was reduced due to the baking from $6.67 * 10^{-4}$ Pa to $2.67 * 10^{-4}$ Pa. After the baking an additional fluence scan was performed using the same plasma parameters as the first fluence scan. Figure 4.15 gives the impurity fluence scan results as well as the previous fluence scan for comparison. The data

Table 4.4: Proto-MPEX sample exposure conditions and plasma parameters near the target for the MPEX-like limiting case with the Si_3N_4 helicon window and a target shutter to screen part of the plasma pulse.

Plasma parameter/Exposure condition	**MPEX-like limiter with Si_3N_4window no target shutter**	**MPEX-like limiter with Si_3N_4window target shutter open from 4.3 to 4.6 s**
Target material	W	W
Gas species	D_2	D_2
Pulse length [s]	0.5	0.5
Number of pulses	5	5
T_e $[eV]$	3	2.7
n_e $[m^{-3}]$	$2.7 * 10^{18}$	$7 * 10^{18}$
Flux per shot $[m^{-2}s^{-1}]$	$3.5 * 10^{22}$	$9.3 * 10^{22}$
Total fluence $[m^{-2}]$	$1.75 * 10^{23}$	$4.8 * 10^{22}$

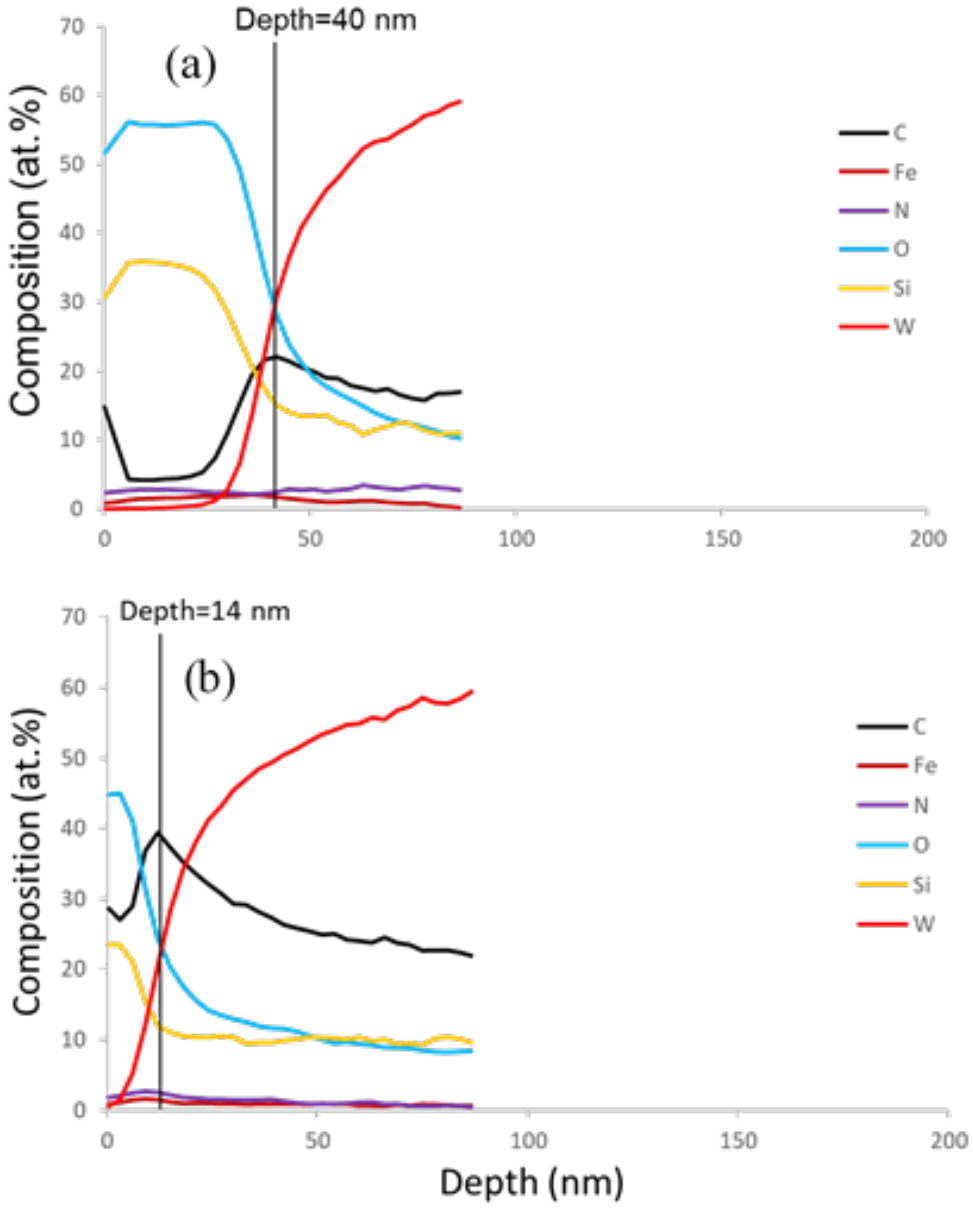


Figure 4.14: The XPS depth profile data for the MPEX-like limiting conditions with a Si_3N_4 helicon window for (a) the exposure without the shutter blocking any of the target during the plasma pulse and (b) the shutter screening the plasma outside of the 4.3 to 4.6 second time frame. The indicated depth is the crossover point for the O and W signals. The standard error of the composition profiles are less than 1%.

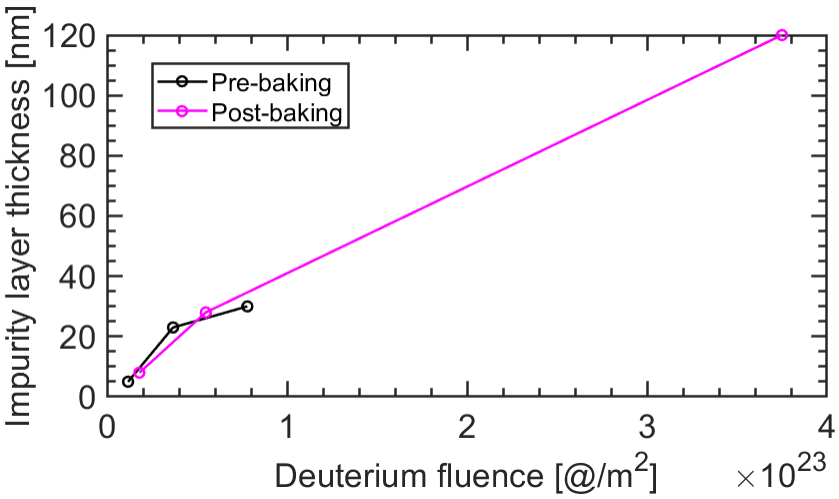


Figure 4.15: The impurity layer thickness for various single plasma pulse fluences during the pre and post-baking time frames of Proto-MPEX.

shows no significant reduction in the impurity thickness versus fluence as expected from the O concentrations and the small base pressure drop. XPS from these samples also showed no change in the O concentration. The baking was likely not long or hot enough to reduce the O in the machine to a measurable level. MPEX will have a baking system and a higher vacuum quality than that of Proto-MPEX which is expected to reduce the role of O. The O could also be from the helicon window as Si is a strong O getter. The AlN helicon window showed O throughout the deposition layer on it so any churning of the helicon window material can lead to released O.

4.3.3 ECH and Krypton Gas Addition and Tilted Target

Changing the impurity source generation has been performed and the next option is to reduce the accumulation of deposited impurities on the target. It is hypothesized that increasing the electron temperature or increasing the mass of the ions impacting the target will lead to additional sputtering of the impurities that accumulate on the target, thus reducing the accumulation of impurities on the target. To increase the re-erosion of the impurities on the target exposures were performed with ECH present. An exposure with only ECH as the additional heating source and two additional exposures with ECH and 3% Kr seeded gas were performed, the later exposure with the target being tilted 45°. The AlN helicon window was installed during these exposures and the helicon power was 90 kW while the ECH power was 50 kW. The exposure conditions are given in Table 4.5 and the XPS results for the three exposures are given in Figure 4.16. The ECH was on for 100 ms during each plasma pulse and the Kr concentration was measured via mixing with partial pressures before being puffed into Proto-MPEX. The XPS shows a reduction in the impurity layer thickness for the perpendicular exposure and a further reduction with Kr present. When compared to the previous MPEX-like limiter exposure having 915 nm for a 2.4x fluence which is greater than the 50x impurity thickness decrease. The increase in electron temperature and higher mass lead to a further increase in erosion of impurities on the target lowering the deposition rate.

Table 4.5: Proto-MPEX sample exposure conditions and plasma parameters near the target for the MPEX-like limiting case with the AlN helicon window and ECH to raise the erosion/redeposition impurity rates.

Plasma parameter/Exposure condition	**MPEX-like limiter with AlN window ~0° Exposure ECH from 4.5 to 4.6 s**	**MPEX-like limiter with AlN window ~0° Exposure with Kr gas ECH from 4.5 to 4.6 s**	**MPEX-like limiter with AlN window ~45° Exposure with Kr gas ECH from 4.5 to 4.6 s**
Target material	W	W	W
Gas species	D_2	$D_2 + 3\%Kr$	$D_2 + 3\%Kr$
Pulse length [s]	0.5	0.5	0.5
Number of pulses	9	18	12
T_e $[eV]$	2.7	4.2	4.2
n_e $[m^{-3}]$	$4.9 * 10^{19}$	$7.2 * 10^{18}$	$1.1 * 10^{19}$
Flux per shot $[m^{-2}s^{-1}]$	$2.75 * 10^{23}$	$1 * 10^{23}$	$1.6 * 10^{23}$
Total fluence $[m^{-2}]$	$2.5 * 10^{24}$	$1 * 10^{24}$	$1 * 10^{24}$

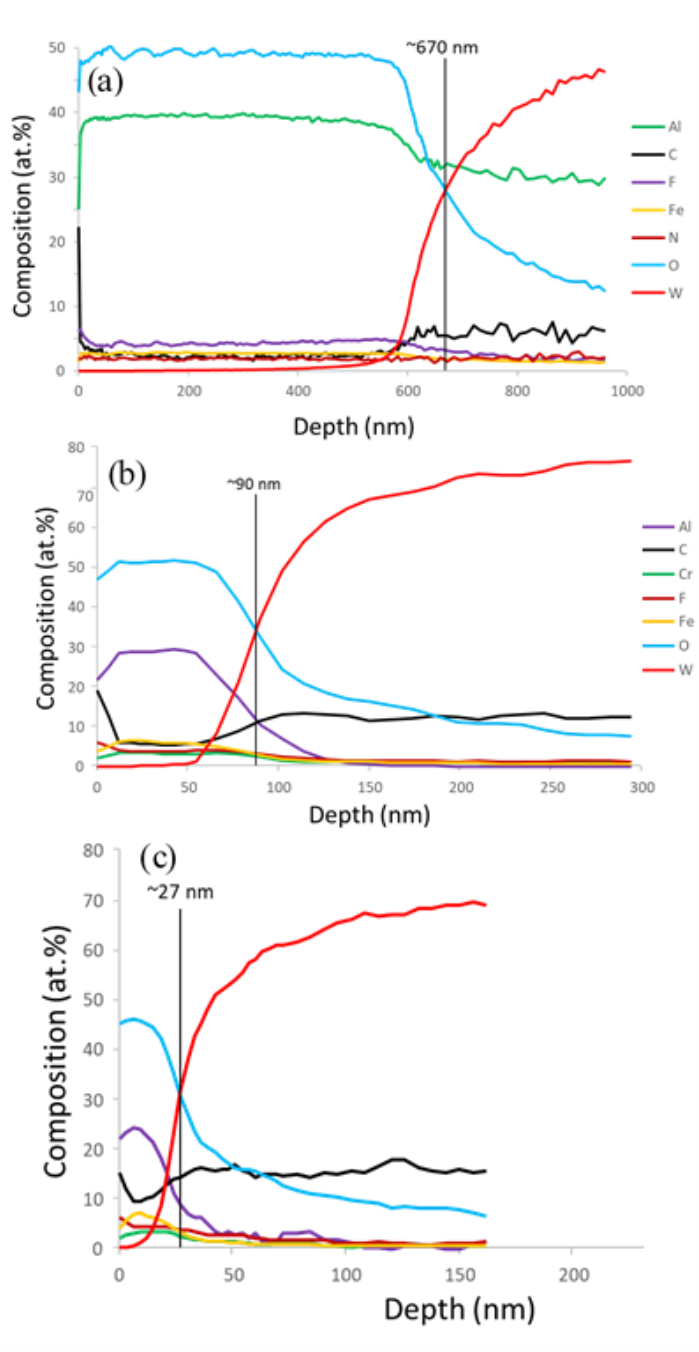


Figure 4.16: The XPS depth profile data for the MPEX-like limiting conditions with an AlN helicon window for (a) a perpendicular target exposure with ECH present from 4.5 to 4.6 seconds (b) the perpendicular target exposure with ECH from 4.5 to 4.6 seconds also with 3% Kr gas seeding (c) the 45° target exposure with ECH from 4.5 to 4.6 seconds with 3% Kr gas seeding. The indicated depth is the crossover point for the O and W signals. The standard error of the composition profiles are less than 1%.

4.4 ICH Window Impurity Generation, Transport, and Deposition

Another window on Proto-MPEX is the alumina window for the ICH. An investigation to determine if this window also produced impurities was performed. It is hypothesized that an increase in Al would be seen on the target during ICH operations if window sputtering is occurring. An exposure of a pure W MAPP target was done using the MPEX-like limiter condition, again with the magnetic field ramping, but this time with 20 kW of ICH present during 4.3 to 4.55 s on each plasma pulse. The Si_3N_4 helicon window was in place for this exposure with the purpose of not masking the Al from the ICH window over those that come from the alumina window. The magnetic field mapping for the LUFS is 0.01 m from the ICH window during these exposures as this will be the MPEX-like gap between the plasma and window. The exposure conditions for the ICH experiment are shown in Table 4.6. 90 kW of helicon power was used for these exposures. The total deuterium ion fluence was lower than previous exposures due to time limitations. The XPS depth profile for the exposure with ICH is shown in Figure 4.17. The O concentration is still present as well as the Si but the Si is reduced in concentration and the main observation is that Al is not present on the samples. This indicates that the ICH for up to 20 kW of power does not created additional impurities from the alumina window. The 30 at.% Si for this exposure was less than the 35 at.% which is likely due to the higher plasma ion temperature. The higher energies may sputter more impurities that make their way to the target but not at high enough rate to remove any impurities from being on the target.

Table 4.6: Proto-MPEX sample exposure conditions and plasma parameters near the target for the MPEX-like limiting case with the Si_3N_4 helicon window.

Plasma parameter/Exposure condition	**MPEX-like limiter with Si_3N_4 window and ICH present**
Target material	W
Gas species	D_2
Pulse length [s]	0.5
Number of pulses	15
T_e $[eV]$	4.8
n_e $[m^{-3}]$	$2.9 * 10^{18}$
Flux per shot $[m^{-2}s^{-1}]$	$5 * 10^{22}$
Total fluence $[m^{-2}]$	$7.6 * 10^{23}$

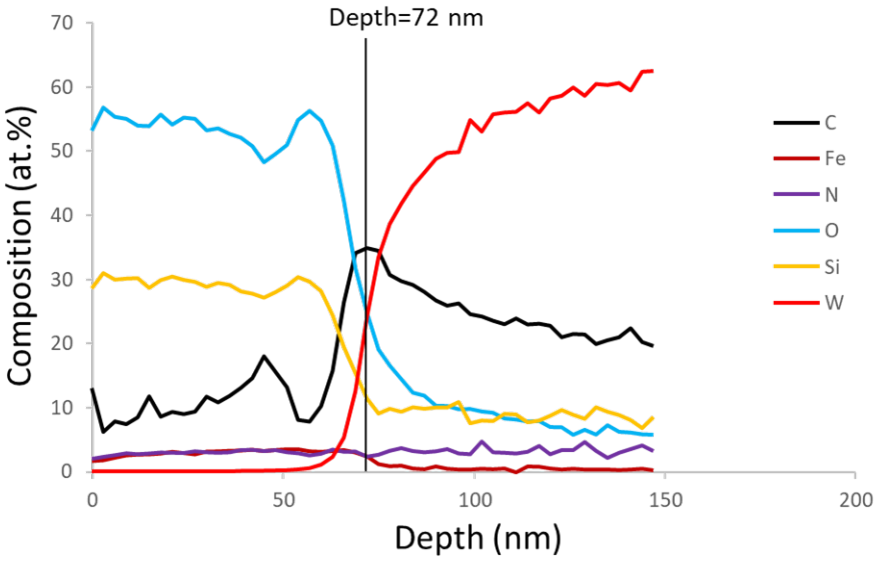


Figure 4.17: The XPS depth profile data for the MPEX-like limiting conditions with a Si_3N_4 helicon window. Each plasma pulse had ICH present from 4.3 to 4.55 seconds. The indicated depth is the crossover point for the O and W signals. The standard error of the composition profiles are less than 1%.

Chapter 5

Helicon Erosion and Redeposition Modeling

Reproduced from C. J. Beers, D. L. Green, C. Lau, J. R. Myra, J. Rapp, T. Younkin, and S. J. Zinkle, "RF sheath induced sputtering on Proto-MPEX part 1: sheath equivalent dielectric layer for modeling the RF sheath," Accepted by Phys. Plasmas (2021).

C. J. Beers contribution was the literature review, COMSOL and GITR modeling, COMSOL and sheath model coupling, sensitivity studies/parameter scans, data collection, data analysis, and manuscript preparation. **D. L. Green** advised on the models. **C. Lau** advised on the COMSOL and sheath model physics. **J. R. Myra** created the sheath model and wrote the template code. **J. Rapp** advised on the experimental setup and conditions that were performed for the model input data. **T. Younkin** created the GITR code and advised on its operations. **S. J. Zinkle** advised on the manuscript and problem statement.

5.1 Model Overview

To understand the erosion and deposition on the AlN helicon window and at the target a model was created for the helicon window limiting case. The model uses a COMSOL Multiphysics ®[83] RF module coupled with a sheath impedance matching model [88–91] to get the RF sheath potential. The RF sheath is thought to be accelerating ions to the helicon window producing additional sputtering. The sputtering yields from the sheath potential

are obtained from Fractal-TRIDYN (F-TRIDYN) [92] which are then used in the Global Impurity TRansport (GITR) code [93–95] to calculate the sputtering rates. The sputtering rates are then assigned to injected particles in the simulation geometry which are used to track impurity transport and get the net deposition and erosion locations. Figure 5.1 gives the flowchart of the model. This model allows for the small scale sheath effects to be studied within a full device model.

5.2 COMSOL Model

The COMSOL Multiphysics®[83] RF module is used to model the 3D axisymmetric full-wave simulation by solving Maxwell's equations in the frequency domain for the Proto-MPEX helicon antenna region. For the discharge simulated in this paper, Proto-MPEX's magnetic field profile and plasma radius of the last uninterrupted flux surface are shown in Figure 5.2. The 3D COMSOL model used is based off of a 2D axisymmetric full-wave simulation of the Proto-MPEX helicon given in Ref. 56 which was used in 3D for the Proto-MPEX ion cyclotron antenna in Ref. 96 and the helicon antenna in Ref. 97. The COMSOL model is adopted within this work for further modeling of an experimental plasma pulse on Proto-MPEX for comparisons. The COMSOL 3D modeled geometry is shown in Figure 5.3 where a one meter plasma column between Z=1.25 m and Z=2.25 m from Figure 5.2 is illustrated. The origin of the COMSOL model is the center of the helicon window and the positive Z-direction is towards the target 2.3 m away. Proto-MPEX makes use of a half-turn helical copper antenna with right-handed helicity for delivering 13.56 MHz to the plasma with various input powers of up to 120 kW. The helicon window is given the material properties of the following: density of 3300 kg/m^3, the dielectric constant is 9, the electrical conductivity is 0 S/m, and the relative permeability is 1. The helicon window is 0.137 m in diameter with a 0.00635 m wall-thickness. The antenna geometry is shown in Figure 5.4. For this simulation 100 kW of power, P, is input at the injection port and 88 kW is delivered to the plasma (forward power) as measured by the total power dissipation in COMSOL. The boundary system shown in Figure 5.3 acts as a matching network with tunable material

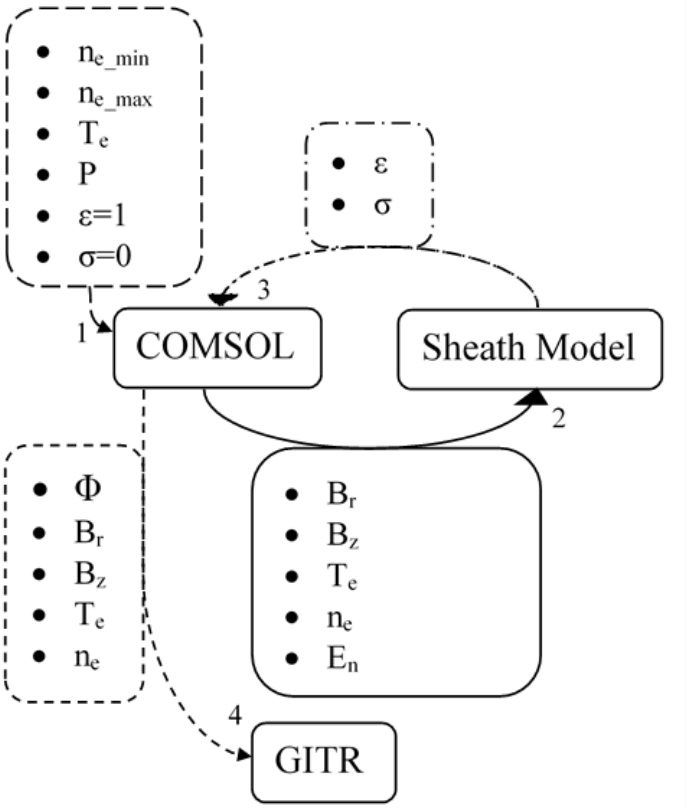


Figure 5.1: The flow chart of the model used within this work. The COMOL inputs are given by arrow 1 and the outputs are given in arrow 2 which are the inputs to the sheath model. The outputs of the sheath model (arrow 3) are then the updated inputs to COMSOL. The process of steps 2 and 3 is iterated until a converged solution is reached. The converged solution of the sheath potential in GITR along with the plasma parameters and field mapping are the inputs to GITR (arrow 4).

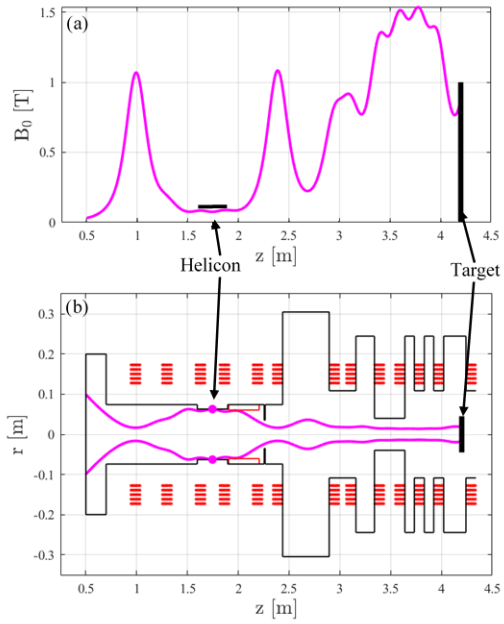


Figure 5.2: The conditions in Proto-MPEX for the COMSOL simulation with (a) the magnetic field strength profile in magenta and (b) the plasma radius in magenta along the last uninterrupted flux surface (LUFS) from the helicon window to the target. In (b) the magenta dot is the intersection point for the LUFS on the helicon window, the horizontal red lines represent the 13 magnetic coil winding cross sections, and the black lines represent the vacuum chamber boundary. The helicon and target locations are indicated for reference.

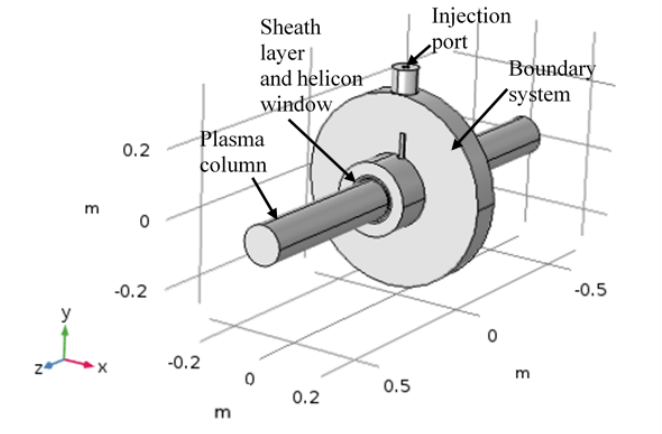


Figure 5.3: The modeled geometry in COMSOL starting from the center outwards is the one-meter long plasma column, the 5 mm wall-thickness sheath layer, the 6.35 mm wall-thickness helicon window, the helicon antenna structure (shown in more detail in Figure 5.4), the boundary system, and the power injection port. The coordinate system is set such that positive Z is towards the target region in Proto-MPEX.

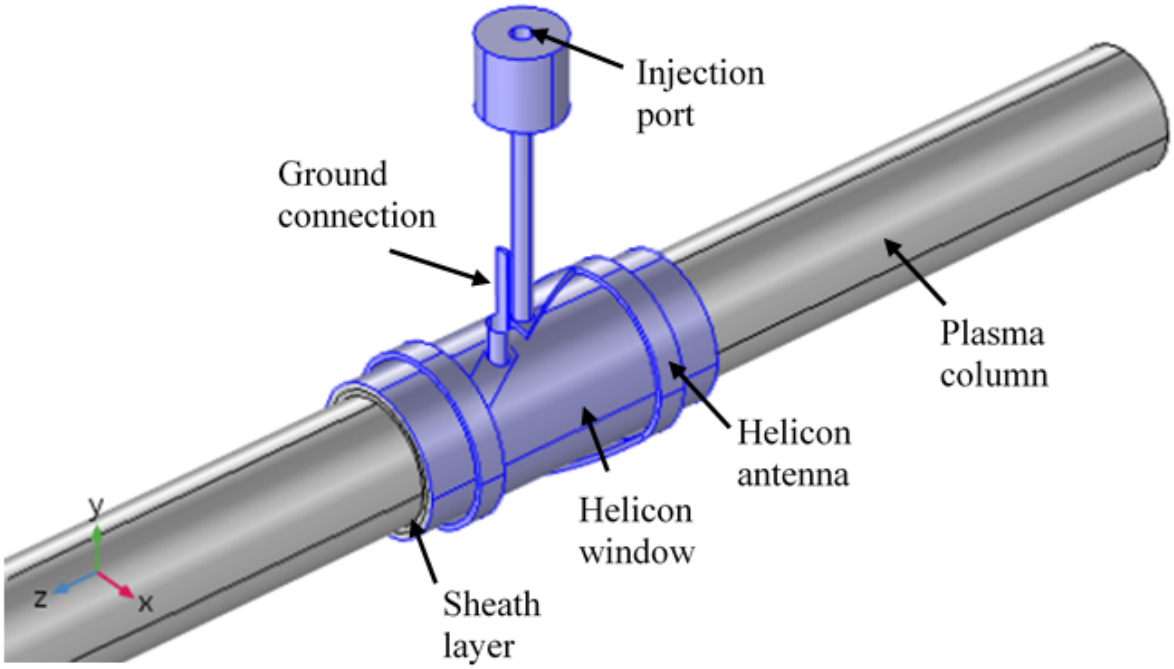


Figure 5.4: The modeled geometry in COMSOL without the boundary system showing the plasma column, the modeled sheath layer on the inside of the helicon window, the helicon window, and the helicon antenna structure which includes the copper antenna, ground connection, and the power injection port.

properties to match experimentally observed power coupling. The Proto-MPEX matching network consists of two variable capacitors that are adjusted to achieve the lowest reflected power similar to the setup in Ref. 98 where the forward and reflected powers are recorded for adjustments.

The simulated plasma radius is 0.06 m except for under the helicon window where a 0.005 m wall-thickness layer is introduced as a simulation layer for the sheath. The plasma density profile within the plasma radius boundary follows that of the magnetic flux function and has a last uninterrupted flux surface plasma edge density of 1.5 x 10^{18} m^{-3} and a plasma core density of 5 x 10^{19} m^{-3}. The density used is based on previous double Langmuir probe measurements taken at Z=1.46 m for a 100 kW injected power high-density helicon normal mode plasma pulse [99]. The plasma tensor derived from cold plasma theory is rotated to follow the magnetic field line curvature within the modeled region [99]. The electron temperature is set to a flat 4 eV profile which is the average temperature for the helicon mode deuterium plasmas used on Proto-MPEX measured at the Z=1.46 m location [69]. The ion flux to the helicon window will be peaked at the center of the window following the field mapping, shown in Figure 5.2, and fall off as the distance from the window center increases. The collisional frequency is set as $2\pi * 13.56$ MHz and is included as an effective mass term in the rotated cold-plasma dielectric tensor. [56, 96, 100] The ends of the plasma column are set as a scattering boundary condition and the sides of the plasma no under the helicon window are set as a perfect electrical conductor.

The simulated sheath layer is between the plasma and helicon window and is introduced in the simulation as a dielectric insulating material with relative permittivity, ϵ, set as 1, and the electrical conductivity, σ, set as 0. The material properties are iterated on with the sheath model to match the properties of the RF plasma sheath. The changes to the sheath layer properties to converge on the RF sheath potential are discussed within section 5.3.1. A wall-thickness of 0.005 m for the sheath layer was chosen such that two mesh elements fit within the layer. Figure 5.5 shows the tetrahedral mesh structure used for the final solution after a mesh convergence study was performed. The sheath layer in blue is on the blown-up section of Figure 5.5 which was set with minimum element size to be half of the layer

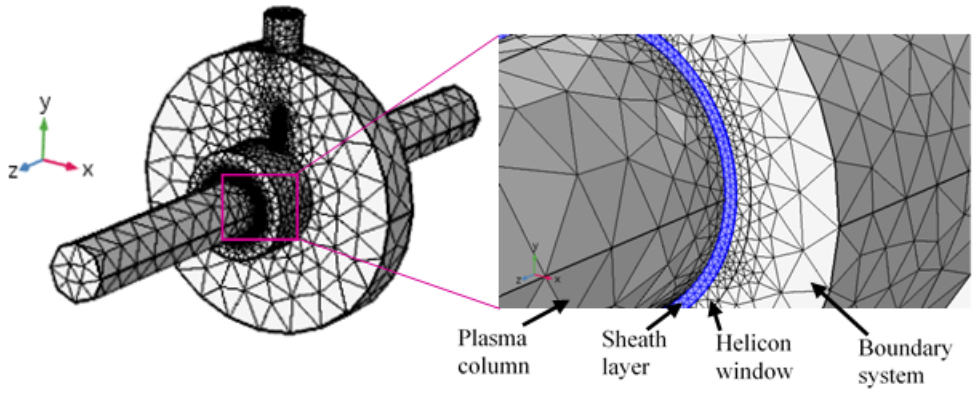


Figure 5.5: The 3D mesh used for the COMSOL simulation with the simulated sheath layer and helicon window blown-up on the right. The sheath layer is shown in blue. The sheath layer thickness is set such that two mesh elements reside within the layer.

thickness at 0.0025 m. This allowed for the conditions to be collected at the center of the layer.

5.3 Sheath Model

The radial scale of the sheath is typically a few Debye lengths (10s of microns) or smaller which is smaller than the RF wavelength and much smaller than the size of the whole device of interest. To solve for the sheath potential a self-consistent RF sheath boundary condition approach has been used. [88, 90, 91, 101, 102] Note, that previous references simulated a conducting wall boundary next to their sheath, but for Proto-MPEX, the boundary is an insulating dielectric ceramic window next to the sheath. Here we instead replace the sheath boundary condition with a dielectric layer in the COMSOL model whose material properties are given by the complex conductivity, σ, (starting at 1) and dielectric constant, ϵ (starting at 0) which have the sheath equivalent properties. While all the RF sheath physics remains the same, the computational implementation of the RF sheath boundary condition is non-trivial within the commercial COMSOL code. A dielectric layer formulation can be implemented in COMSOL with a spatially varying dielectric tensor.

To solve for the conductivity and dielectric constant we start from the impedance of sheath, Z_{sh}, which is described in Ref. 88 and 89, and the dimensionless sheath impedance, $\hat{z}$, which are connected via:

$$Z_{sh} = Z_0 * \hat{z} \tag{5.1}$$

where Z_{sh} is in Ohms, and Z_0, the impedance of a single sheath is given by:

$$Z_0(Ohms) = \frac{9 * 10^{11} * 4\pi * \lambda_{de}(cm)}{\omega_{pi}(s^{-1}) * A_{\perp}(cm^2)} \tag{5.2}$$

where λ_{de} is the Debye length, ω_{pi} is the ion plasma frequency, and $A_{\perp}$ is the surface area. Both the Debye length and the ion plasma frequency are evaluated at the sheath entrance. The relationship between the sheath impedance factor and the sheath admittance factor, $\hat{y}$, is given by:

$$\hat{y} = 1/\hat{z} \tag{5.3}$$

where $\hat{z}$ is the inverse of the sheath admittance $\hat{y}$, which is given by:

$$\hat{y} = \frac{1}{\hat{z}} = \frac{\langle JV \rangle}{\langle V^2 \rangle} - \frac{i\omega \langle J\dot{V} \rangle}{\langle \dot{V}^2 \rangle} \tag{5.4}$$

where J is the total current across the sheath, $\dot{V} = dV/dt$, and at the wall, $x = x_1$, is where all quantities are evaluated at. The sheath admittance is the ratio of the RF current density to the RF potential across the sheath at the frequency of 13.56 MHz for Proto-MPEX. Here, the sheath admittance factor is comprised of the electron, displacement, and ion admittance factors which are a function of the dimensionless quantities: the ion mobility parameter, $\hat{\omega}$, the ion magnetization parameter, $\hat{\Omega}$, the normal component of the unit vector parallel to the B field, b_n, and the 0 to peak amplitude, ξ, which are given by:

$$\hat{\omega} = \frac{\omega}{\omega_{pi}}, \hat{\Omega} = \frac{e * B}{m_i * \omega_{pi}}, b_n = \frac{\overrightarrow{B} \cdot n}{B}, \xi = \frac{e * \Phi_{sh}}{T_e} \tag{5.5}$$

where ω is the wave frequency, $\rightarrow n$ is the unit surface normal, $\overrightarrow{B}/B$ is the unit vector parallel to the B field, Φ_{sh} is the RF potential across the sheath or the simulated sheath layer, and T_e is the plasma electron temperature. Note, the normalized DC current density flowing through the sheath can also modify the sheath admittance factor but is set to 0 within this paper because the helicon window is an insulator.

The sheath impedance in SI units can be had by using $\mu_0 = 4\pi * 10^{-7}$(H/m), $c = 3 * 10^8$(m/s), and the permittivity of free space, ϵ_0(F/m), given by:

$$\epsilon_0 = 1/(\mu_0 * c^2) \tag{5.6}$$

The impedance of the sheath in SI units is then given by:

$$Z_0 = \frac{\lambda_{de}(m)}{\epsilon_0 * \omega_{pi} * A_{\perp}(m^2)} \tag{5.7}$$

Next the parameters are derived for the simulated sheath equivalent layer. Φ_{sh}, is given by:

$$\Phi_{sh} = Z_{sh} * I_{sh} \tag{5.8}$$

where the sheath current, I_{sh} is given by:

$$I_{sh} = J_n * A_{\perp} \tag{5.9}$$

where J_n is the sheath current density normal to the surface. Using Equation 5.1 and 5.9 we get:

$$J_n = \frac{I_{sh}}{A_{\perp}} = \frac{\Phi_{sh}}{A_{\perp} * Z_{sh}} = \frac{\Phi_{sh}}{A_{\perp} * Z_0 * \hat{z}} \tag{5.10}$$

For the sheath equivalent simulated layer we have:

$$J_n = \sigma * E = \sigma * \frac{\Phi_{sh}}{d} \tag{5.11}$$

where, σ is the electrical conductivity, E is the electric field, and d is the thickness of the simulated sheath layer. Setting Equation 5.10 and 5.11 equal to each other gives:

$$\frac{\sigma}{d} = \frac{1}{A_{\perp} * Z_0 * \hat{z}} \tag{5.12}$$

The limit where the ions are unmagnetized in the sheath occurs when $\Omega_i << \omega_{pi}$ or equivalently when $\lambda_{de} << \rho_i$ where ρ_i is the ion gyroradius evaluated at the ion sound speed. The sheath ions are always unmagnetized within Proto-MPEX but the model parameters allow for them to be magnetized in the magnetic pre-sheath. For the sheath electrons to be unmagnetized the case when $\lambda_{de} << \rho_e$, where ρ_e is the electron thermal gyroradius, must be satisfied. This case is true for the higher density regions at the helicon window in Proto-MPEX, but for the lower density regions it is not true. Due to the unavailability of an electron sheath impedance model that spans the unmagnetized and magnetized regimes, both cases are investigated which are referred to as the unmagnetized and magnetized electron sheath cases. References 88 and 103 have looked at the role of the RF sheath regimes on

the boundary condition formulation and found that for the unmagnetized case the $\hat{\Omega}$ is not needed and therefore one can set $b_n = 1$.

Now using Equation 5.2 and the sheath admittance we can solve for the complex conductivity of the simulated sheath layer given by:

$$\sigma = \epsilon_0 * \hat{y} * \omega_{pi} * \frac{d}{\lambda_{de}} \tag{5.13}$$

Using $\epsilon = i * \sigma/\omega$ the dielectric susceptibility (relative permittivity) is given by:

$$\epsilon = i * \epsilon_0 * \frac{\hat{y}}{\hat{\omega}} * \frac{d}{\lambda_{de}} \tag{5.14}$$

where i is the unit imaginary number. The real part of the electrical conductivity and relative permittivity come from the real and imaginary parts of the sheath admittance in Equation 5.13 and 5.14, respectively.

For a thin layer the normal electric field in the layer, E_n, will be constant and the voltage across the layer is a surrogate for the sheath potential and is given by:

$$\Phi_{sh} = E_n * d \tag{5.15}$$

The sheath voltage is independent of the thickness of the layer which can be proven by matching the conditions across the simulated layer/plasma interface in the form of:

$$V_s = d_s * E_s = d_s * \frac{\epsilon_p \cdot \overrightarrow{E}_p}{\epsilon_s} \tag{5.16}$$

where the subscript s denotes the simulated sheath layer and p denotes the plasma. E_s is the normal voltage in the simulation layer, ϵ_s is the complex scalar dielectric in the layer, and d_s is the thickness of the layer. Using Equation 5.14 then yields:

$$V_s = d_s * E_s = -i * \hat{\omega} * \lambda_{de} * \frac{\epsilon_p \cdot \overrightarrow{E}_p}{\hat{y}} \tag{5.17}$$

which is independent of the layer thickness, d_s. Lastly, using Equation 5.1 and Equation 5.2 brings us back to the sheath voltage being the sheath current times the sheath impedance given by:

$$
\begin{aligned}
V_s &= -i * \hat{\omega} * Z_s * A_\perp * \epsilon_0 * \epsilon_p \cdot \overrightarrow{E}_p \\
&= Z_s * A_\perp * \sigma_p \cdot \overrightarrow{E}_p \\
&= \overrightarrow{E}_p * A_\perp * Z_s \\
&= I_p * Z_s \\
&= I_s * Z_s
\end{aligned}
\tag{5.18}
$$

5.3.1 COMSOL and Sheath Model Coupling

A validation case has been performed comparing to the work in Ref. 90 for the fits used within that work and comparison to the fits used within this work. The validation study results are given in Appendix D.

The goal is to have the simulated sheath equivalent layer physics equal to that of those in the sheath as derived in the previous section. In COMSOL the displacement current normal to the surface, D_n, is matched across the interface between the plasma and the sheath layer and is given in the layer by:

$$
D_n = \frac{i * J_n}{\omega} = \epsilon_{sim} * E_{n,sim} \tag{5.19}
$$

where sim denotes the simulated sheath equivalent layer and $E_{n,sim}$ is given by:

$$
E_{n,sim} = \frac{\partial \Phi_{sim}}{\partial x} = \frac{i * J_n}{\omega * \epsilon_{sim}} \tag{5.20}
$$

Taking the 1-D electrostatic problem for $d << c/\omega$ which has $\nabla \times E_x(x) = 0$ gives:

$$
\Phi_{sim} = \frac{i * d}{\omega * \epsilon_{sim}} * J_n \tag{5.21}
$$

Figure 5.6 shows the surface and dielectric layer geometry for the 1D case with d being the thickness of the dielectric layer, n being normal to the surface in the x-direction, and t being tangential to the surface direction. It should be noted that as long as $d << c/\omega$, d can be chosen in the simulated geometry to be constant everywhere and for all iterations. Setting Equation 5.21 and Equation 5.8 equal yields:

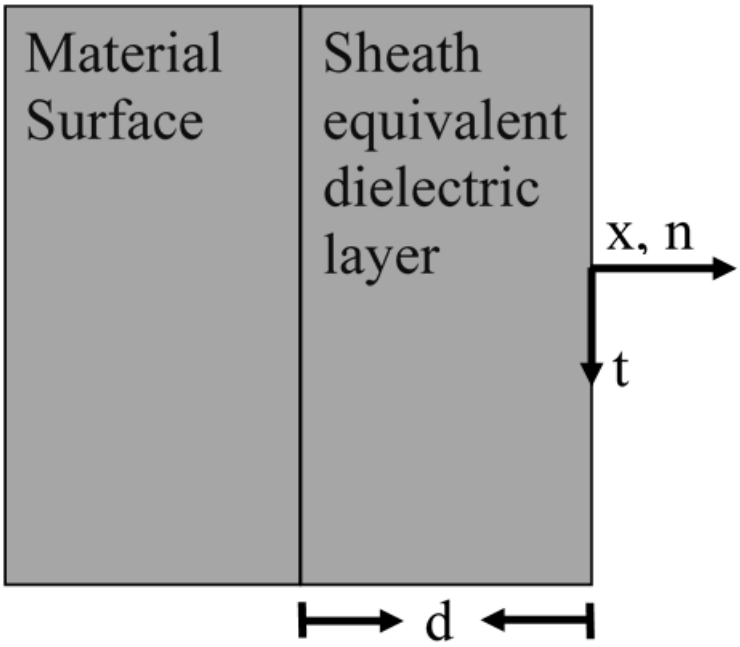


Figure 5.6: The diagram of the sheath equivalent dielectric layer with thickness, d. The current density normal to the equivalent layer surface, n, is along the x-direction.

$$\frac{i * d}{\omega * \epsilon_{sim}} = Z_{sh} * A_{\perp} \tag{5.22}$$

which equivalently is

$$\epsilon_{sim} = \frac{i * \epsilon_0}{\hat{\omega} * \hat{z}} * \frac{d}{\lambda_{de}} \tag{5.23}$$

which matches that of Equation 5.14.

This process of impedance matching is an iterative one since $\hat{z}$ is a function of the RF wave amplitude at the surface. The iteration starts with an initial guess for $\hat{z} = 0$ which was taken to be the insulating limit where $\epsilon_{sim} = 1$ and $\sigma = 0$ for allowing vacuum capacitance. The plasma properties at the sheath are input parameters to the sheath model and were obtained by running a simulation without the sheath layer present and by taking the plasma parameters at the plasma/helicon window interface location. The sheath's plasma electron temperature and density, magnetic angle to the helicon window surface, b_n, and the electric field imposed on the window to solve for the sheath potential Φ_{sh}, in Equation 5.5 from COMSOL are used as the inputs to the sheath model to get an updated $\hat{z}$. This sheath simulation layer and iterative process is a more general one that can account for shine through of the RF to the helicon window. Figure 5.1 shows the flow of the model coupling and the inputs to each model. 100 points radially and 1000 points axially along the window are output from COMSOL to be input to a MATLAB script that locally calculates the RF sheath model. This solves each point through a naive Picard process for the updated $\hat{z}$ and gives a corresponding updated conductivity and relative permittivity value. The new conductivity and relative permittivity values are then input to COMSOL in an interpolation function and set as the updated material properties for the layer. The properties of the helicon window remain constant throughout the iterations. This process is repeated until the tolerance of $< 5\%$ change is seen in the potential across the layer. This iterative method takes 10 or fewer cycles for all cases analyzed. Figure 5.7 shows the sheath potential along the z-direction at $\theta = 90°$ for the low-density unmagnetized and magnetized electron sheath cases and Figure 5.8 shows the high-density convergence for the unmagnetized and magnetized

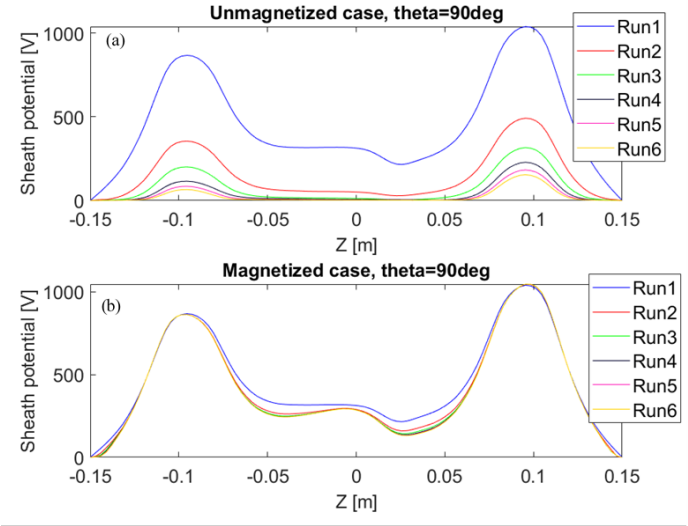


Figure 5.7: The sheath potential showing convergence plotted along the Z-direction at $\theta = 90°(y = 0\ m$ and $x = 0.06\ m)$ for the low-density cases using the (a) the unmagnetized case and (b) the magnetized case. The final run number shown is the run that reached the convergence tolerance of $> 5\%$ change.

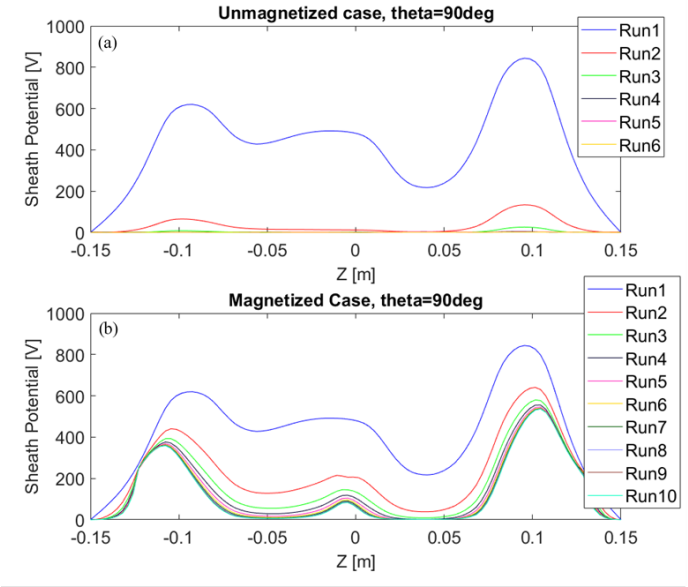


Figure 5.8: The sheath potential showing convergence plotted along the Z-direction at $\theta = 90°(y = 0\ m$ and $x = 0.06\ m)$ for the high-density cases using the (a) the unmagnetized case and (b) the magnetized case. The final run number shown is the run that reached the convergence tolerance of $> 5\%$ change.

electron sheath cases. The final run number is the number of iterations needed to reach the set tolerance.

Proto-MPEX's plasma conditions are between an unmagnetized and magnetized electron boundary limits within the sheath because the electron Larmor radius is comparable to the sheath width. Both the bounding cases are analyzed using the sheath model which created two iterations of both the low-density and high-density simulations. For both models, the desired output is the RF sheath potential which is the converged electric field times the thickness of the layer. Figure 5.9 shows the electric field imposed on the simulated sheath layer for the high-density magnetized case and the wire frame of the helicon antenna structure is overlayed on the simulated sheath layer for reference. The unrolled sheath potential across the equivalent layer is given in Figure 5.10 for the four modeled cases where the view is looking at the inner diameter of Figure 5.9 starting at $y = 0$ m and $x = 0.06$ m for the 0° point and moving counterclockwise along the window around the Z-axis to go to 360°. It can be seen that there are hot spots that developed mainly under the helicon antenna in both conditions and the potentials present in the unmagnetized case are much lower than the magnetized case. With these potentials and the ion fluxes to the helicon, the sputtering yields can be calculated in F-TRIDYN.

5.3.2 Mesh Study

To perform a convergence study with the COMSOL mesh a scan with the "Fine" and "Finer" preset COMSOL options and an additional "Custom" mesh option were ran. The custom mesh resolution was finer than the "Finer" present option. The low-density magnetized electron sheath case was used and only the mesh options for the plasma were altered. The mesh parameters used for the scan are given in Table 5.1. The sheath layer was set a custom mesh to have two elements in the layer and the total mesh elements to be below $1.5 * 10^6$. The results of the simulations showed no changes between themselves and the first solution from 5.10 (b) for both the shape of the profile and the magnitude. The custom mesh was used for all other simulations to keep the conditions the same.

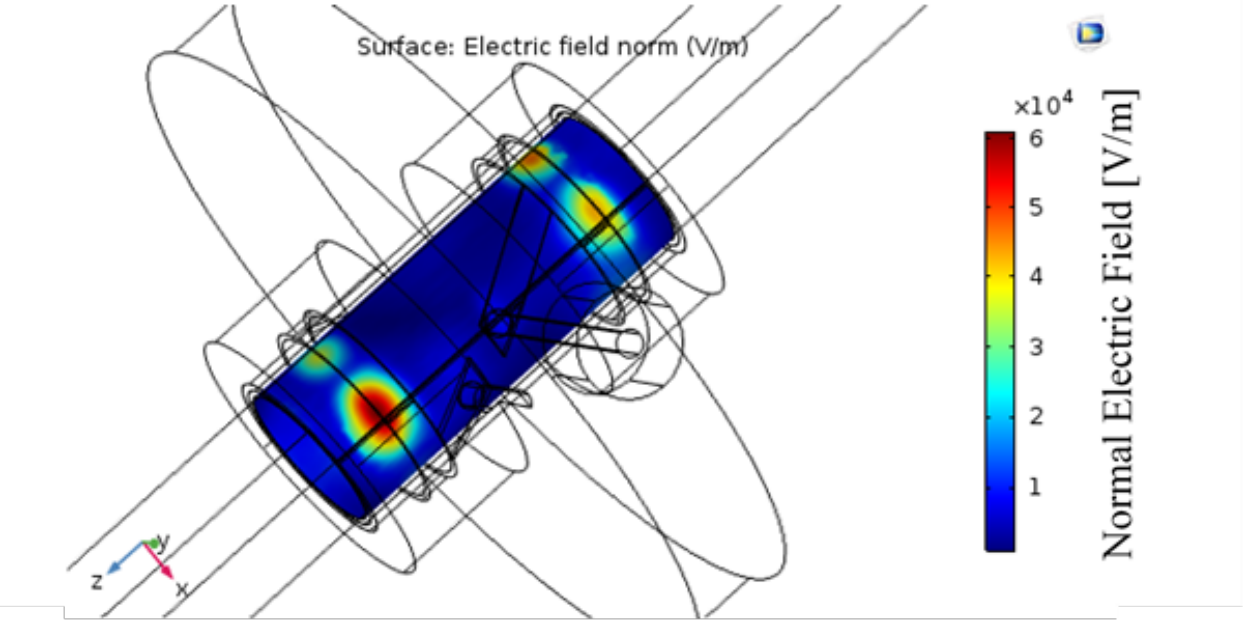


Figure 5.9: The COMSOL produced 3D electric field normal on the inner diameter of the helicon window for the magnetized sheath model case. The highest potentials imposed on the window are underneath the helicon end rings. The wire frame of the geometry shown in Figure 5.4 is given for reference.

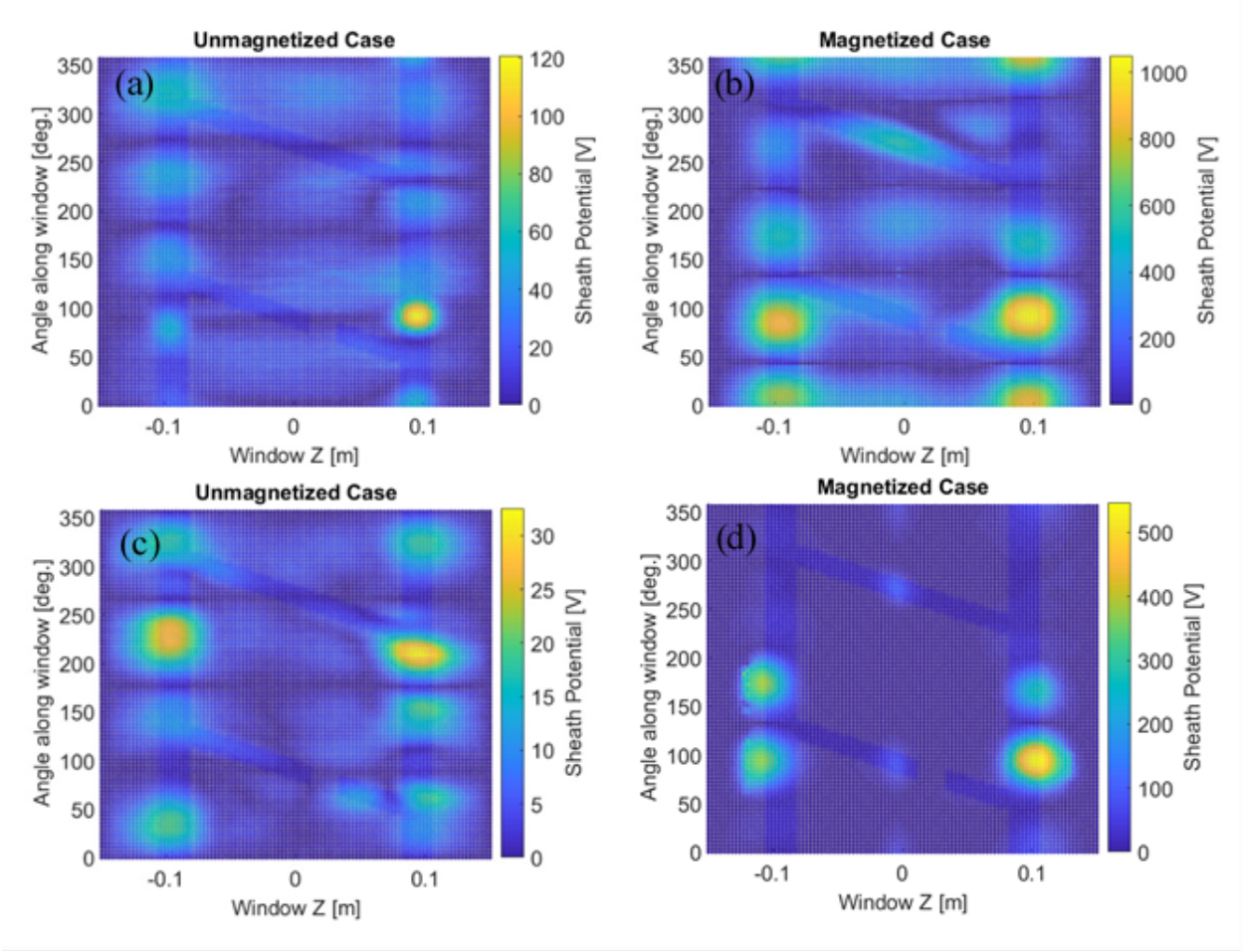


Figure 5.10: The potential across the sheath layer in the COMSOL model that has been unrolled for (a) the low-density unmagnetized sheath case, (b) the low-density magnetized sheath case, (c) the high-density unmagnetized case, and (d) the high-density magnetized case. An overlay of the helicon antenna location has been placed on both plots for reference.

Table 5.1: COMSOL mesh settings

Mesh Condition		Maximum element size	Minimum element size	Maximum growth rate	Curvature factor	Resolution of narrow regions
Plasma	Fine Mesh	0.105	0.0132	1.45	0.5	0.6
	Finer Mesh	0.0723	0.00526	1.4	0.4	0.7
	Custom Mesh	0.1	0.002	1.5	1	0.5
Sheath Layer		0.004	0.0025	1.5	1	0.5
Boundary System		0.8	0.005	1.5	0.6	0.5

5.3.3 Role of Power on Sheath Potential

A COMSOL simulation using 50 kW of inject power was run for both the unmagnetized and magnetized case with the low-density parameters. Figure 5.11 shows the converged sheath potentials for the two cases. The sheath potential profiles are similar to the 100 kW pulses but the magnitudes are less for both cases. The lower power reduces the voltage potential across the window but the lower density near the sheath creates the increased potential when compared to the high-density cases.

5.3.4 Role of Density on Sheath Potential

A higher density case with an edge density of $1*10^{19}m^{-3}$ and a core density of $1*10^{20}m^{-3}$ was run in COMSOL to understand the role of density on the sheath potentials. Figure 5.12 gives the converged sheath potential results for the unmagnetized and magnetized sheath cases. The potentials match the pattern of the core density of $5*10^{19}m^{-3}$ case but have a lower magnitude. The higher density near the sheath has a higher current and thus reduces the potential.

5.4 GITR Model

The Global Impurity TRansport (GITR) code is a 3D Monte Carlo particle tracking code 93. Benchmarking and validation studies for GITR have been performed in Ref. 93 and 104. GITR tracks the full gyro-motion of ions through the Lorentz force, including drifts in a steady state scenario. Simulated ion species undergo Coulomb collisions with a Maxwellian distributed (drifting if there is a flow velocity) background plasma species. The interaction of ions with the material surface is simulated through reflection and sputtering. Input data for physical sputtering and reflection yields and their reflected/sputtered energy and angle distributions are generated and input from F-TRIDYN [92], a binary-collision approximation code. The sputtering yields for D onto Al are shown as a function of ion impact angle and energy in Figure 5.13.

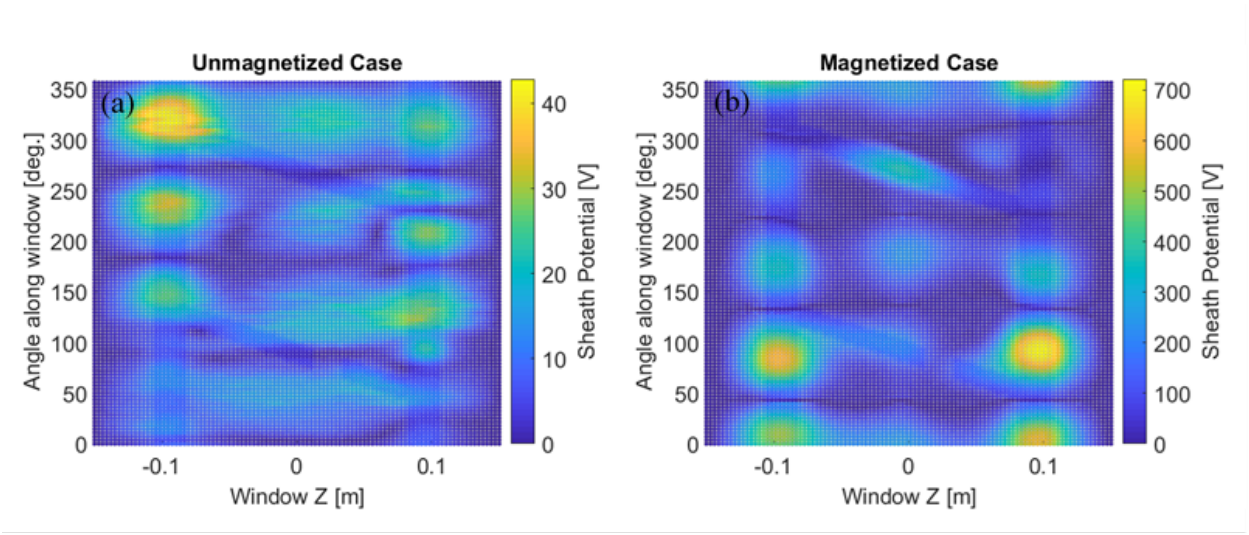


Figure 5.11: The converged sheath potentials using 50 kW of injected power for (a) the unmagnetized sheath case and (b) the magnetized sheath case.

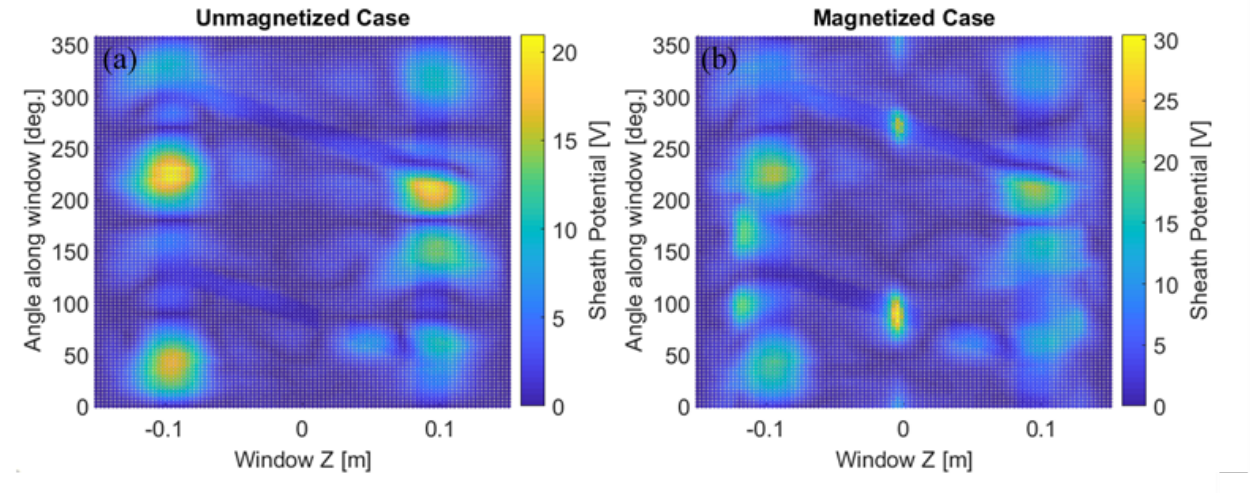


Figure 5.12: The converged sheath potentials using an edge density of $1 * 10^{19} m^{-3}$ and a core density of $1 * 10^{20} m^{-3}$ for (a) the unmagnetized sheath case and (b) the magnetized sheath case.

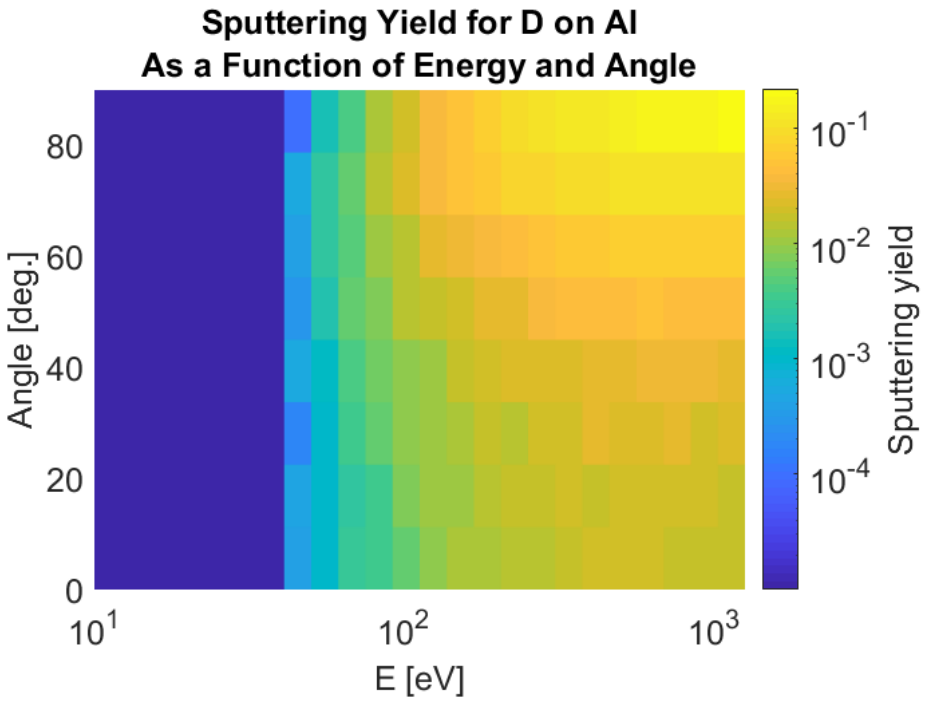


Figure 5.13: The sputtering yields for D impacting onto Al based on the energy and angle, (Ψ), of the incoming ion where the angle is defined as the angle from the surface normal as shown in Figure 2.4.

The modeled geometry is 0.4 m in length and 0.125 m in diameter with a maximum tetrahedral mesh length of 0.005 m. An Al boundary follows that of the helicon window geometry with a diameter of 0.125 m and a length of 0.3 m and the boundary outside of the window and at the end boundaries (referred to here as the end caps) are a surface with a sticking coefficient of one. The window material is chosen to be pure Al to simplify the sputtering yield calculations as the helicon window nitrogen is assumed to be lost in the vacuum chamber via volatile H_xN_y processes. The pure Al case is not expected to change the results as the window is expected to be Al enriched near the surface based on Ref. 41, which found for D^+ ion irradiation of AlN that the Al/N ratio at the surface approximately doubled over that of an unexposed surface.

The problem of physical sputtering is computationally expensive to model, and has complex dependencies to account for, as each particle has an incoming angle and energy which then produces an angle and energy distribution for the sputtered particle(s). In this work, various approximations to the impacting ion energy-angle distribution at the surface are used to study these parameters. To simulate the ion energy-angle distribution of D^+ ions at the Al surface with the GITR model, a velocity half-sphere of Maxwellian distributed particles are initialized, with the half-sphere directed along the magnetic field toward the helicon window. The position of these particles is initialized to the sheath entrance (the point at which 99% of the sheath electric field potential has been integrated) above a flat surface. Particles are traced through an analytic electric field model, gyromotion, drifts, and Coulomb collisions until they impact a surface. The distribution of impact energy, E_{impact} and impact angle with respect to the surface normal, θ, are binned in a histogram which gives the distribution function $f_i(E_{impact}, \theta)$ at the surface for each introduced particle. The effective sputtering yield, $\hat{Y}_{s,i}$, from ion species, i, D in this case, is given by:

$$\hat{Y}_{s,i} = \frac{\iint f_i(E_{impact}, \theta) * Y_i(E_{impact}, \theta)\, dE\, d\theta}{\iint f_i(E_{impact}, \theta)\, dE\, d\theta} \tag{5.24}$$

where f_i is the D^+ ion distribution function. Equation 5.24 gives the effective sputtering yield of Al by D, accounting for the averaged sputtering yield over the ion energy-angle distribution for D^+ ions at the Al surface. The sputtering yield in Equation 5.24, $Y_i(E_{impact}, \theta)$, comes

from an array of F-TRIDYN simulations. F-TRIDYN simulations of D on Al vary the E_{impact} parameter from 10 to 2500 eV (20 intervals logarithmically spaced) and vary the θ parameter from 0 to 89.9 degrees (18 intervals linearly spaced). The surface binding energy of 3.19 eV was used as the surface binding energy for Al in the F-TRIDYN simulations. Four-dimensional look-up tables were generated based on GITR simulation of D on Al, varying parameters in surface potential, and ion/electron temperature and density. Subsequently, sputtering yields based on the plasma electron density at the Al surface ($1 * 10^{16}$ m^{-3} to $1 * 10^{19}$ m^{-3}) and temperature (5-10 eV), the plasma ion temperature (assumed to be equal to the electron temperature), the ion impact angle distribution from GITR, and the sheath potential at the surface (10 to 1200 V) can be interpolated at the helicon window surface. The average sputtering yield for each mesh element is calculated and the total eroded Al flux per mesh element is then given by:

$$\Gamma_{s,eroded} = \sum_i \hat{Y}_{s,i} * \Gamma_{i,total} \tag{5.25}$$

where $\Gamma_{i,total}$ is the total ion flux to the mesh element. The total ion flux to the Al surface is a function of the plasma electron density and temperature profiles and the electron density is the same as was used for the COMSOL simulation with a maximum core density of $5 * 10^{19}$ m^{-3}. An electron temperature profile that was taken from double Langmuir probe measurements near the helicon region at Z=1.25 m was used in GITR. A measured profile is used here instead of the flat 4 eV as in the COMSOL model to capture the variation in ionization mean free path within the plasma column as the ions traverse varying electron densities and temperatures. COMSOL simulations making use of the electron temperature profile, along with using 8 eV in the sheath model showed negligible change in surface potential, and the hot spot locations remained the same. Figure 5.14 shows the electron density and temperature profile used in the GITR simulation which is constant along the Z-axis of the modeled geometry.

To simulate the Al transport and deposition, subsequent GITR simulations are run using the same model setup but this time with sputtered neutral Al particles initialized near the helicon window surface. The distribution of initialized locations of particles across the helicon

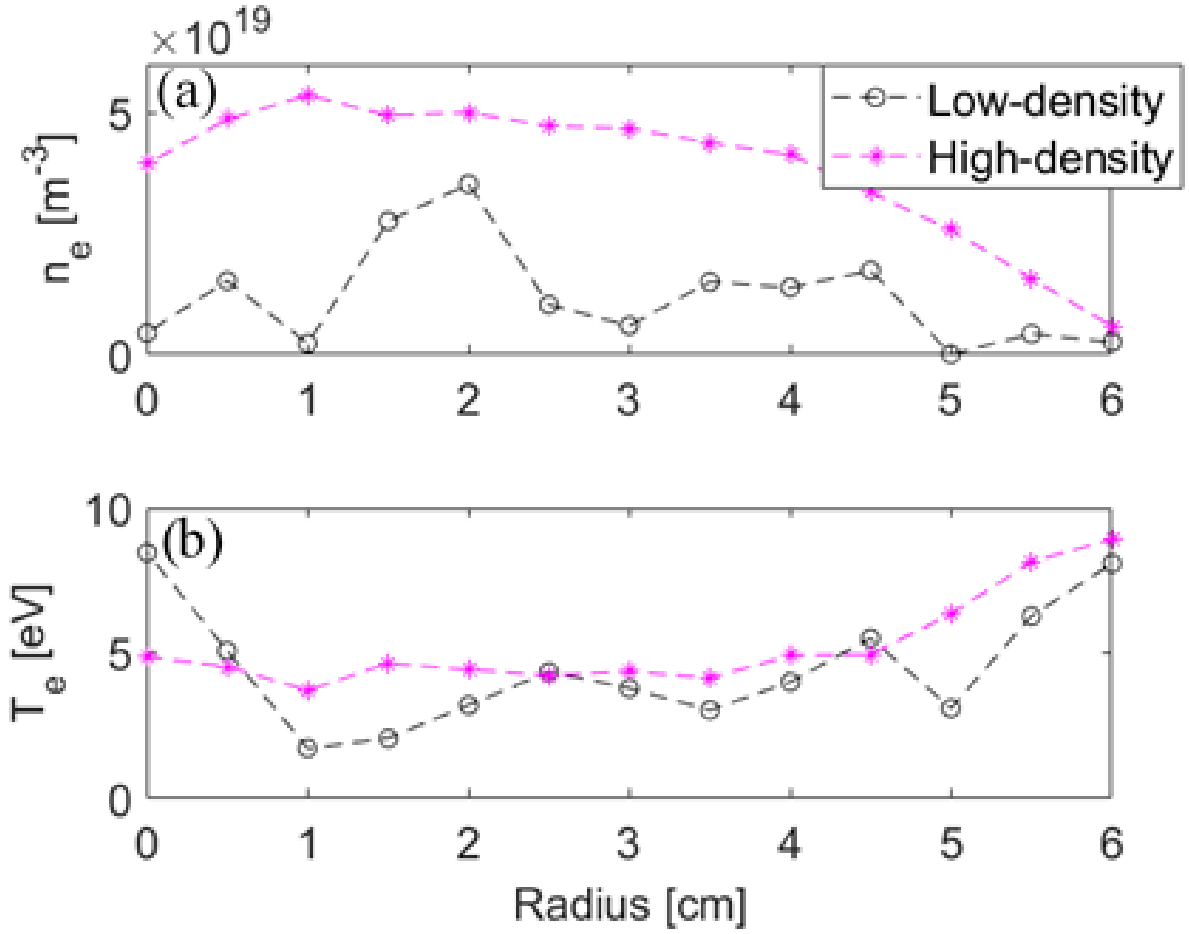


Figure 5.14: The (a) plasma electron density and (b) electron temperature profiles used in the GITR simulation for the low-density and high-density cases. Data was taken via double Langmuir probe at Z=1.25 m at t=4.175s.

window is generated using the distribution of eroded Al flux. Each particle simulated is an equal fraction of the total eroded Al flux so sufficient particles need to be simulated to get enough counts in each mesh element to have a converged solution. For the mesh size of 0.005 m, $1 * 10^6$ particles gives a converged erosion and deposition flux after $5 * 10^5$ time steps at $1 * 10^{-9}$ s per step. Self-sputtering of Al by Al is included in the simulation and the Al particles and their ionization states are tracked throughout the modeled geometry. Figure 5.15 gives the sputtering yields used for the Al onto Al impacts based on the incoming ion's impact energy and angle. The eroded and deposited Al flux on the helicon window or the Al flux to the end caps is of interest and is therefore tallied.

Figure 5.16 shows the model flow chart for obtaining the sputtering Al yield and flux from inputs from F-TRIDYN, GITR, and the sheath potential from Figure 5.10 (steps 1 and 2). Step 3 then takes the Al flux with a GITR simulation to model the ionization, migration, and deposition of the eroded Al flux.

5.4.1 COMSOL and GITR Coupling

The spatial distribution of sheath potential on the helicon window created the need to model this variation in GITR. The GITR code was modified to accept input, as part of the geometry input file, for the specification of the 3D surface sheath potential. The initial GITR inputs are shown by arrow 4 in Figure 5.1. The potential is then used in the analytic sheath electric field calculation for eroded Al ions near the surface where the electric field is given by:

$$E_n = \Phi_{sh} * (\frac{f_{de}}{2 * \lambda_{de}} * e^{\frac{-r}{2*\lambda_{de}}} + \frac{1 - f_{de}}{\rho_i} * e^{\frac{-r}{\rho_i}}) \tag{5.26}$$

where f_{de} is the fraction of the sheath potential difference in the Debye region, ranging from 0 to 0.32 for these simulations, and r is the normal distance of the Debye and Chodura sheath from the surface. [105–107] The electric field along with Coulomb collisions directly contribute to the simulated ion impact energies and the total sputtering yield per mesh element. The total Al erosion and deposition fluxes are tallied to see if impurities stay

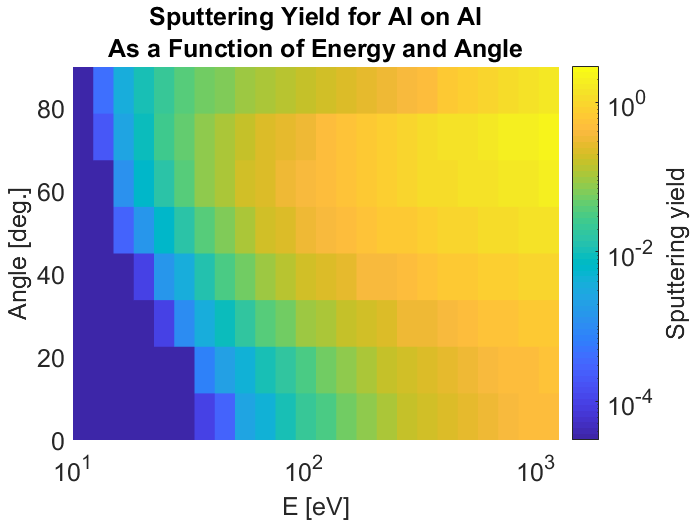


Figure 5.15: The sputtering yields for Al impacting onto Al based on the energy and angle, (Ψ), of the incoming ion where the angle is defined as the angle from the surface normal as shown in Figure 2.4.

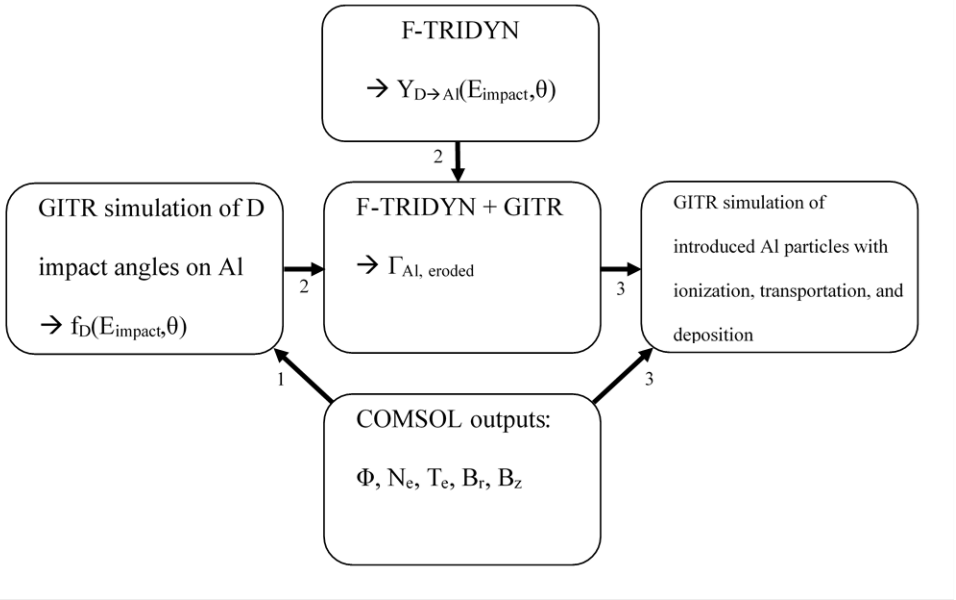


Figure 5.16: The flow chart for the GITR simulations. In step 1 the COMSOL sheath potentials are inputs to GITR to get the D ion fluxes to each mesh element. Step 2 uses the F-TRIDYN calculated sputtering yields to get the eroded Al flux at each mesh element. In step 3 the sheath potential again with GITR is used to introduce and track surrogate particles representing the total eroded Al flux where the transportation and deposition locations can be tracked.

within the helicon region or exit it. Figure 5.17 and Figure 5.18 show the Al gross deposition, gross erosion, net deposition, net erosion, Al ion flux in the -Z direction out of the modeled geometry, and the Al ion flux in the +Z direction out of the modeled geometry for the low-density unmagnetized and magnetized cases, respectively. Figure 5.19 and Figure 5.20 show the Al gross deposition, gross erosion, net deposition, net erosion, Al ion flux in the -Z direction out of the modeled geometry, and the Al ion flux in the +Z direction out of the modeled geometry for the high-density unmagnetized and magnetized cases, respectively. The helicon antenna is overlayed for reference and it can be seen that the same hot spots locations as seen in Figure 5.10 are present. The end caps are at location $Z = \pm 0.2$ m from the helicon window center where the upstream end cap is moving in the negative Z-direction towards the dump plate and the downstream side end cap is moving in the positive Z-direction towards the target region of the machine. The main redeposition areas are seen to be around the high erosion areas and particles that leave the helicon region moves equally in both directions.

5.4.2 GITR Mesh and Particle Scan

Each particle in the GITR simulation is representative of a flux value and to get good statistics in the simulation both the mesh and particle number need to be set so that a solution is converged upon. Three particles were used before looking at the mesh as the mesh is for visualization of the impurities fluxes and the particles determine them quantities. $5 * 10^5$, $1 * 10^6$, and $2 * 10^6$ particles were simulated and at $1 * 10^6$ particles the solution converged. Figure 5.21 shows the GITR solutions for the $5 * 10^5$ and $1 * 10^6$ particles. The $2 * 10^6$ is not shown because it is the same solution as for $1 * 10^6$ particles. $1 * 10^6$ particles due to this was used for all other simulations.

The mesh values used investigated were a minimum mesh length of 0.01 and 0.005 m. Figure 5.22 gives the GITR results for the two mesh sizes used. The 0.005 m mesh minimum length displays the data with a smoother gradient and thus was used for all other simulations.

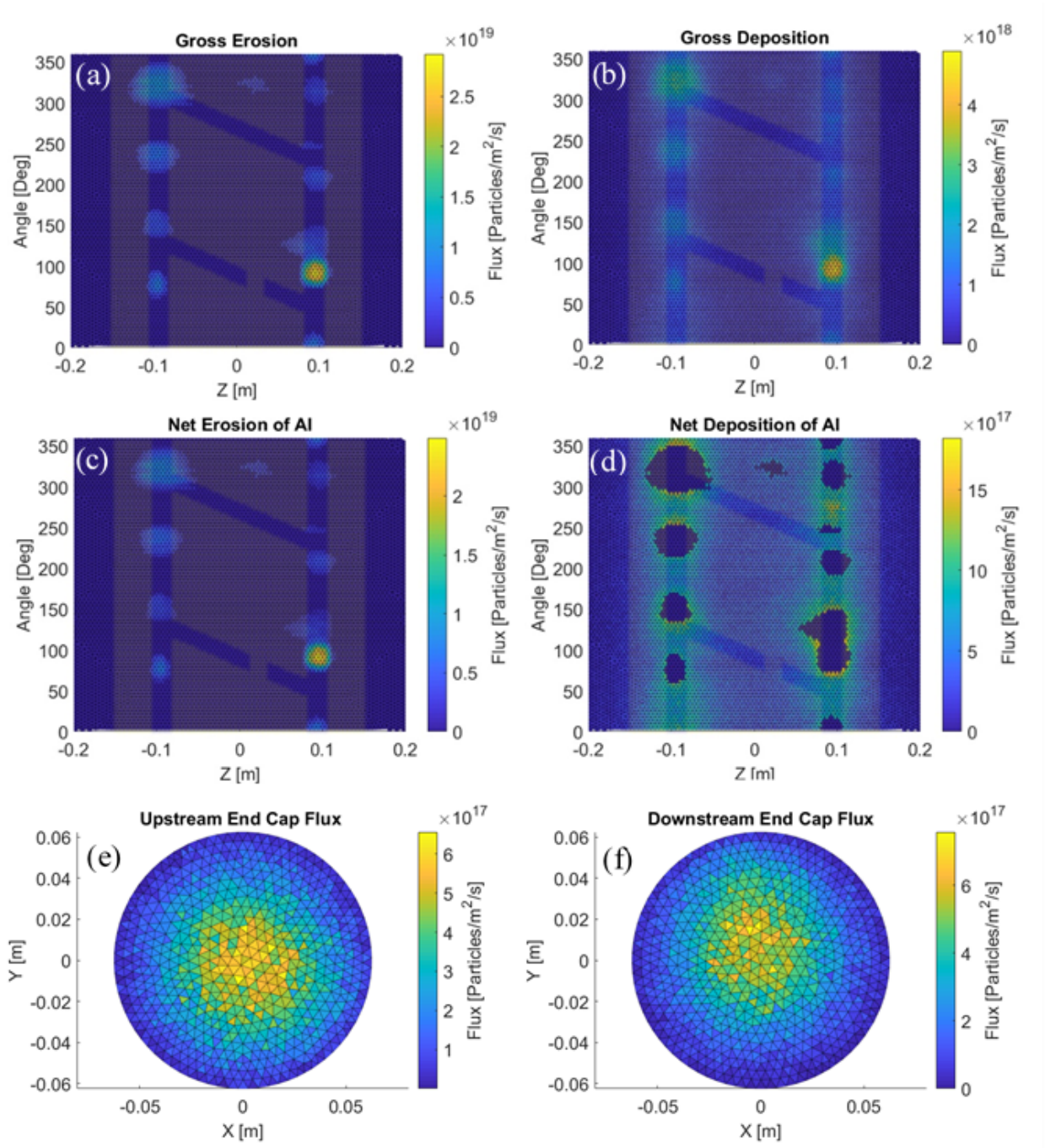


Figure 5.17: The GITR results on the AlN window for the low-density unmagnetized sheath case for (a) the gross Al erosion flux, (b) the Al gross deposition flux, (c) the Al net erosion flux, (d) the Al net deposition flux, (e) the ionized Al impurity flux moving in the -Z-direction out of the helicon region at Z=-0.2 m, and (f) the ionized Al impurity flux moving in the +Z-direction out of the helicon region at Z=0.2 m. The helicon antenna overlay is present on a-d for reference.

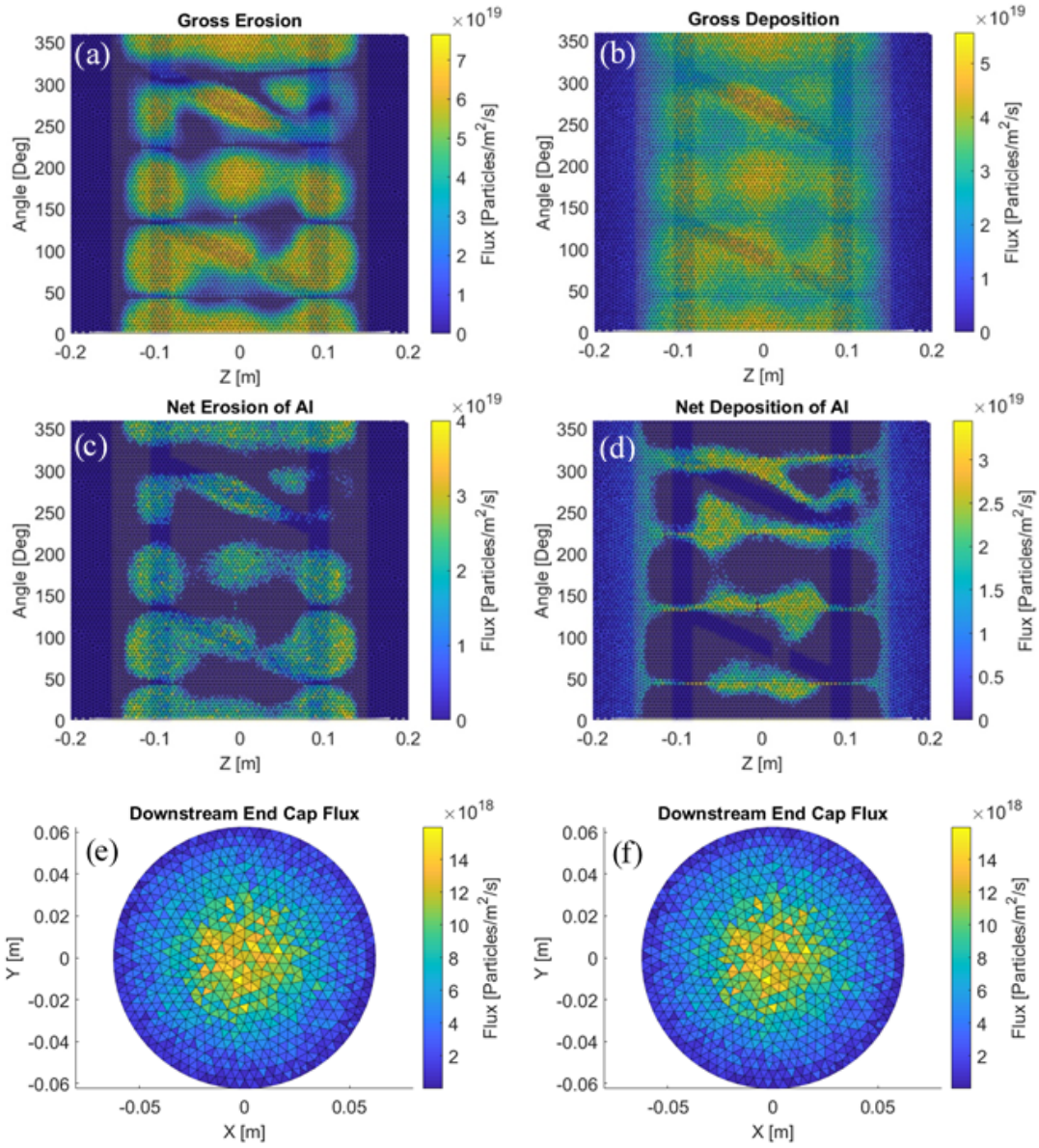


Figure 5.18: The GITR results on the AlN window for the low-density magnetized sheath case for (a) the gross Al erosion flux, (b) the Al gross deposition flux, (c) the Al net erosion flux, (d) the Al net deposition flux, (e) the ionized Al impurity flux moving in the -Z-direction out of the helicon region at Z=-0.2 m, and (f) the ionized Al impurity flux moving in the +Z-direction out of the helicon region at Z=0.2 m. The helicon antenna overlay is present on a-d for reference.

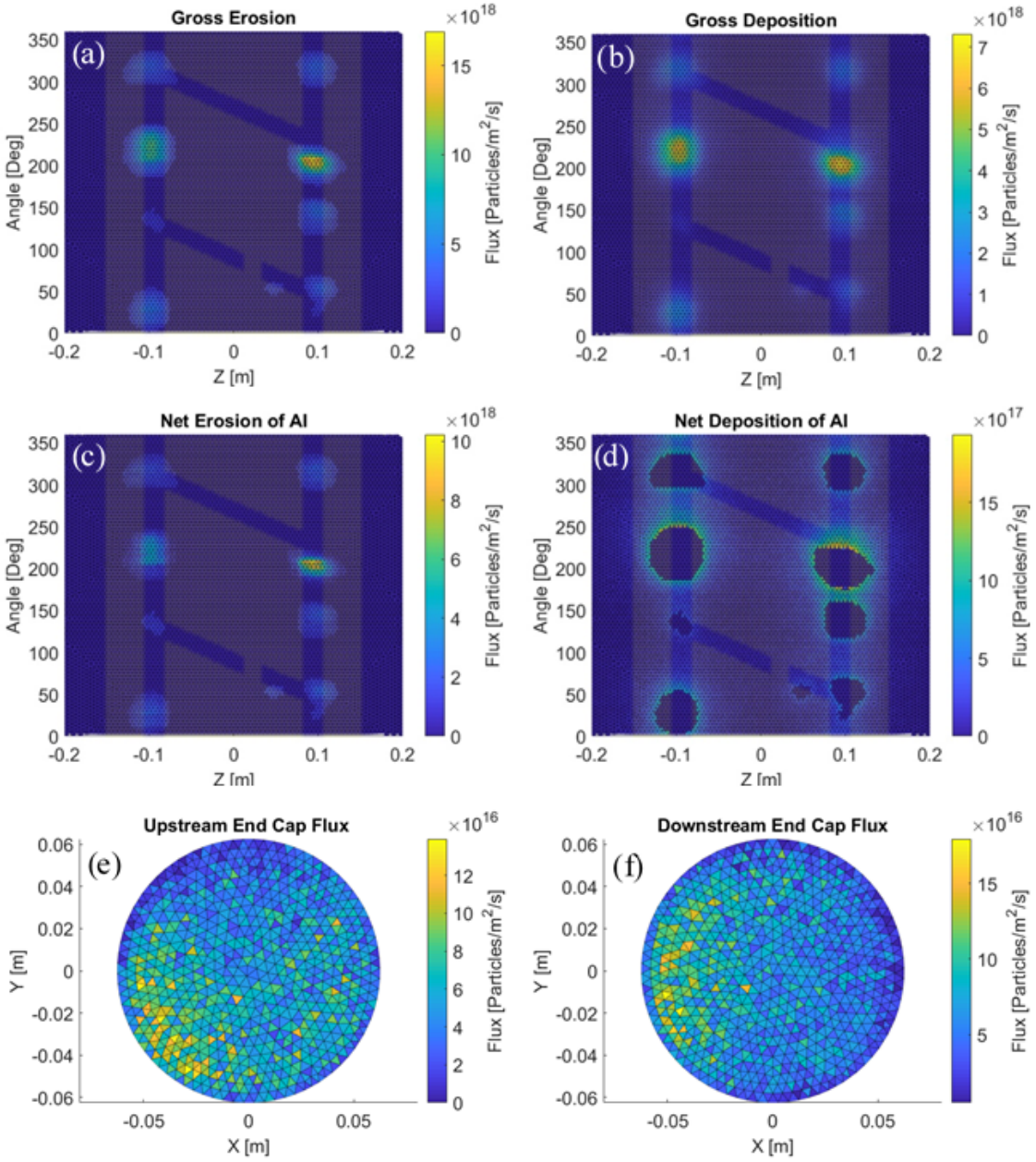


Figure 5.19: The GITR results on the AlN window for the high-density unmagnetized sheath case for (a) the gross Al erosion flux, (b) the Al gross deposition flux, (c) the Al net erosion flux, (d) the Al net deposition flux, (e) the ionized Al impurity flux moving in the -Z-direction out of the helicon region at Z=-0.2 m, and (f) the ionized Al impurity flux moving in the +Z-direction out of the helicon region at Z=0.2 m. The helicon antenna overlay is present on a-d for reference.

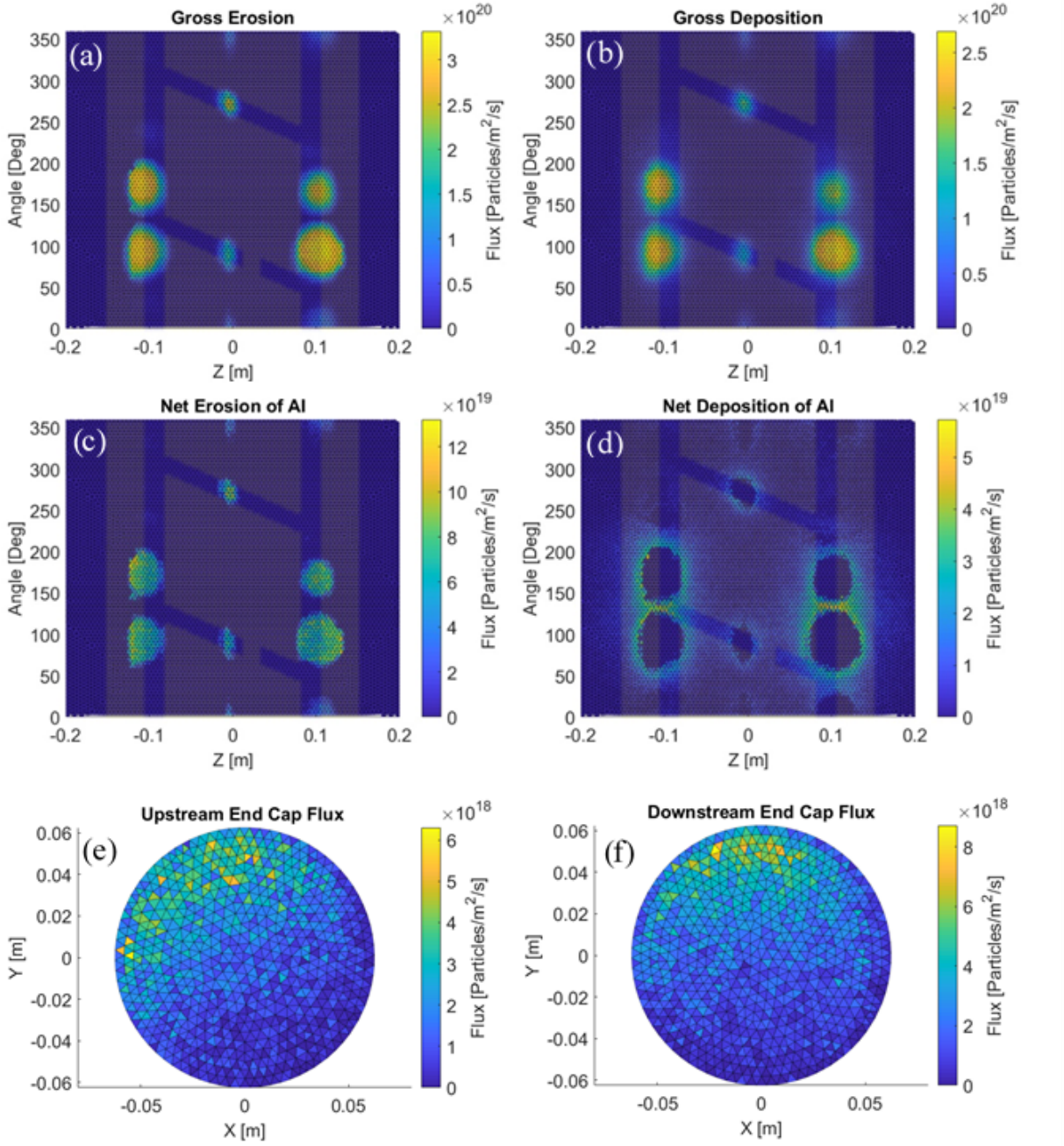


Figure 5.20: The GITR results on the AlN window for the high-density magnetized sheath case for (a) the gross Al erosion flux, (b) the Al gross deposition flux, (c) the Al net erosion flux, (d) the Al net deposition flux, (e) the ionized Al impurity flux moving in the -Z-direction out of the helicon region at Z=-0.2 m, and (f) the ionized Al impurity flux moving in the +Z-direction out of the helicon region at Z=0.2 m. The helicon antenna overlay is present on a-d for reference.

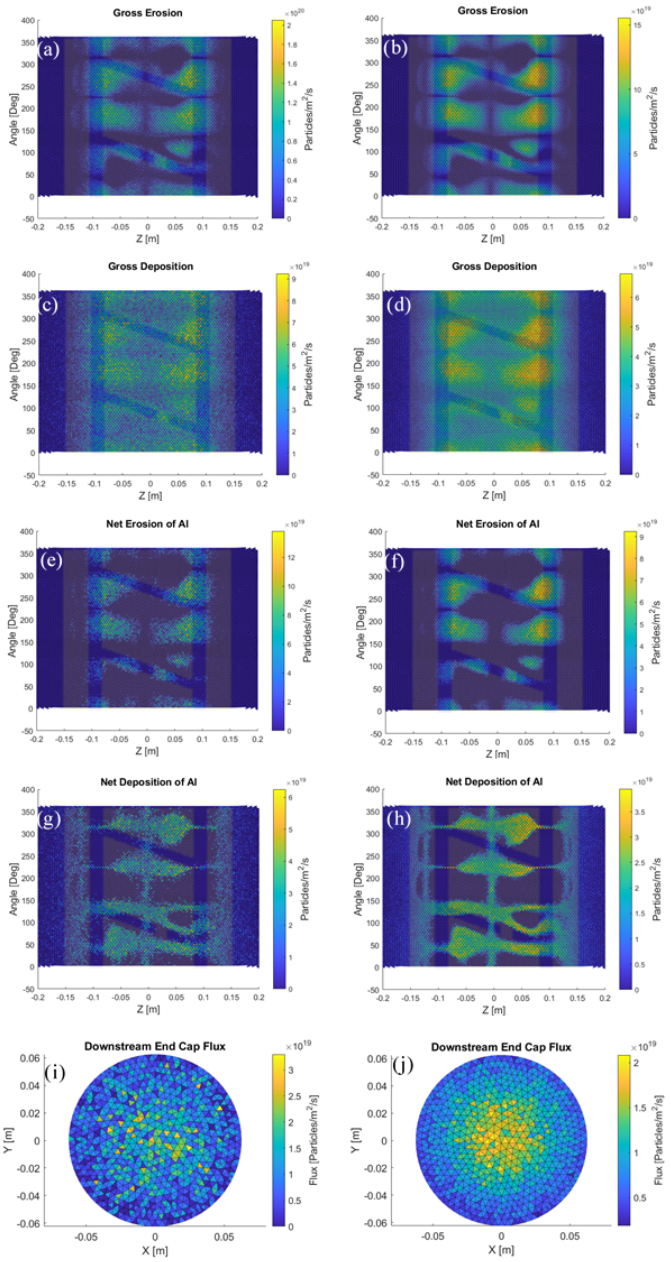


Figure 5.21: The GITR results on the AlN window for the low-density magnetized sheath case with $1 * 10^5$ particles for (a) the gross Al erosion flux, (c) the Al gross deposition flux, (e) the Al net erosion flux, (g) the Al net deposition flux, and (i) the ionized Al impurity flux moving in the +Z-direction out of the helicon region at Z=-0.2 m. $1 * 10^6$ particles used in GITR is shown in (b) the gross Al erosion flux, (d) the Al gross deposition flux, (f) the Al net erosion flux, (h) the Al net deposition flux, and (j) the ionized Al impurity flux moving in the +Z-direction out of the helicon region at Z=-0.2 m The helicon antenna overlay is present on a-h for reference.

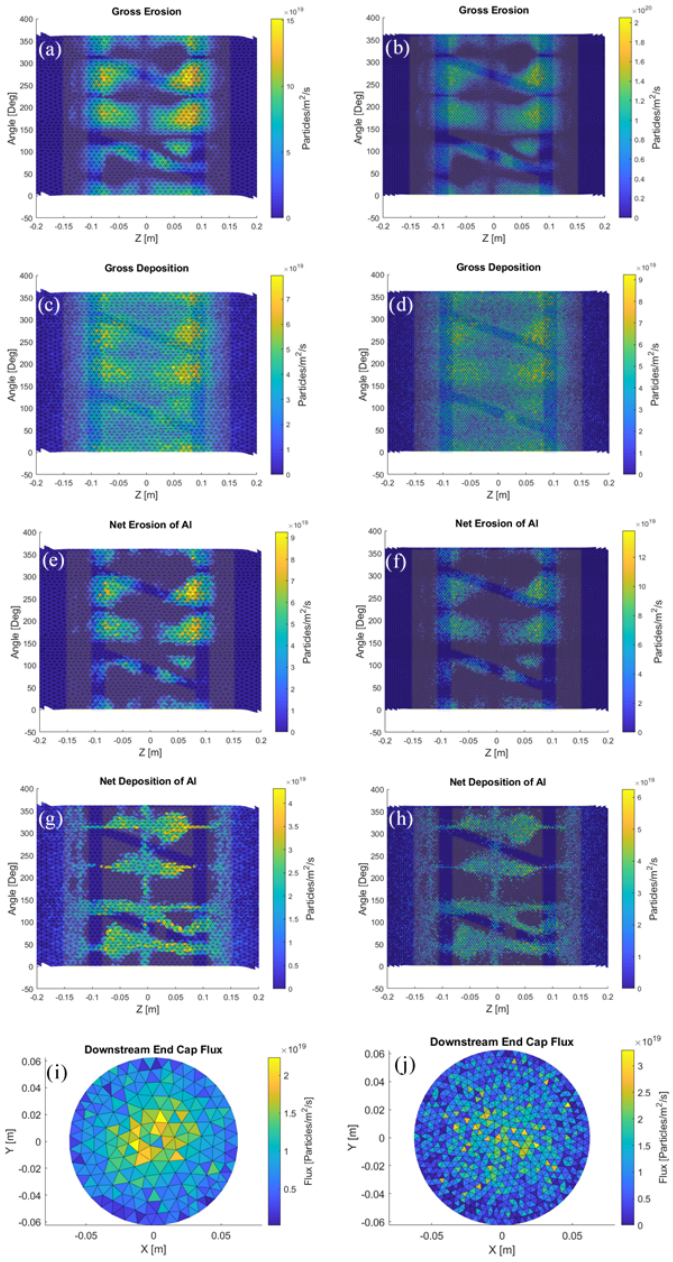


Figure 5.22: The GITR results on the AlN window for the low-density magnetized sheath case with minimum mesh length of 0.01 m for (a) the gross Al erosion flux, (c) the Al gross deposition flux, (e) the Al net erosion flux, (g) the Al net deposition flux, and (i) the ionized Al impurity flux moving in the +Z-direction out of the helicon region at Z=-0.2 m. A finer mesh with minimum length of 0.005 m in GITR was used in (b) the gross Al erosion flux, (d) the Al gross deposition flux, (f) the Al net erosion flux, (h) the Al net deposition flux, and (j) the ionized Al impurity flux moving in the +Z-direction out of the helicon region at Z=-0.2 m The helicon antenna overlay is present on a-h for reference.

5.4.3 Role of Impact Angle on Sputtering Yield

Looking at Figure 5.22 one can see the vertical net deposition pattern in the middle of the image. This is due the magnetic field mapping to the helicon window being perpendicular at the center of the window. To understand the vertical strip an impact angle of 75° across the entire window was analyzed. Figure 5.23 shows the GITR solution for the gross erosion for the magnetic field mapping and the 75° impact. The vertical strip is no longer there, and the erosion distribution no longer has the sharp break in the profile. The perpendicular magnetic field and also the 75° impact angle is not physical and impact angles are a distribution. To keep the magnetic field angle mapping but removing the perpendicular locations the impact angle was set to 89° at locations were they would be $> 89°$. The F-TRIDYN sputtering yields used an average sputtering yield for the given impact angles along the helicon window.

5.4.4 Role of Mach Number on Impurity Transport

The high-density simulations have the Al impurity flux at the edge of the plasma column which doesn't match the expected radial impurity movement. This is likely due to the axial velocity assigned to the particles being zero. To investigate the radial impurity movement the axial velocity was scaled between 0 and 1 for the Mach number. Figure 5.24 shows the GITR results for the high-density magnetized case using axial velocities of 0, 200, 5000, 10000, and 27000 m/s. The radial impurity densities move inward as the axial velocity increases as expected. To use the radial movement within Proto-MPEX a full device model was created in GITR and is discussed in Section 5.5.

5.4.5 Role of Oxygen on Experiments

The experimental composition of the deposition layer showed a high concentration of O throughout the layer indicating that O is present in Proto-MPEX throughout the pulse. To understand the role of O on the sputtering of the helicon window additional GITR simulations were performed with O as the species producing sputtered Al instead of D. These simulations used the sheath potentials from the four COMSOL cases and the F-TRIDYN sputtering

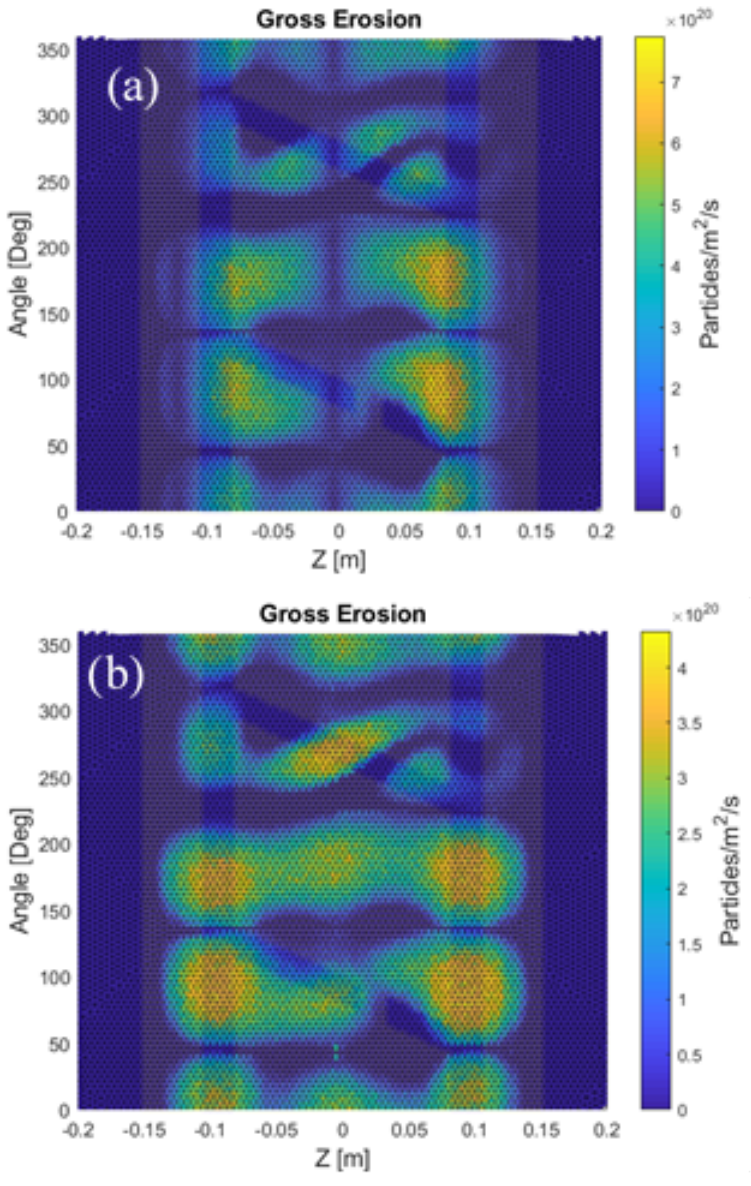


Figure 5.23: The GITR gross erosion on the AlN window for the low-density magnetized sheath case for (a) impact angles taken as the magnetic field angle intersections with the helicon window and (b) 75° impact angle across the entire helicon window.

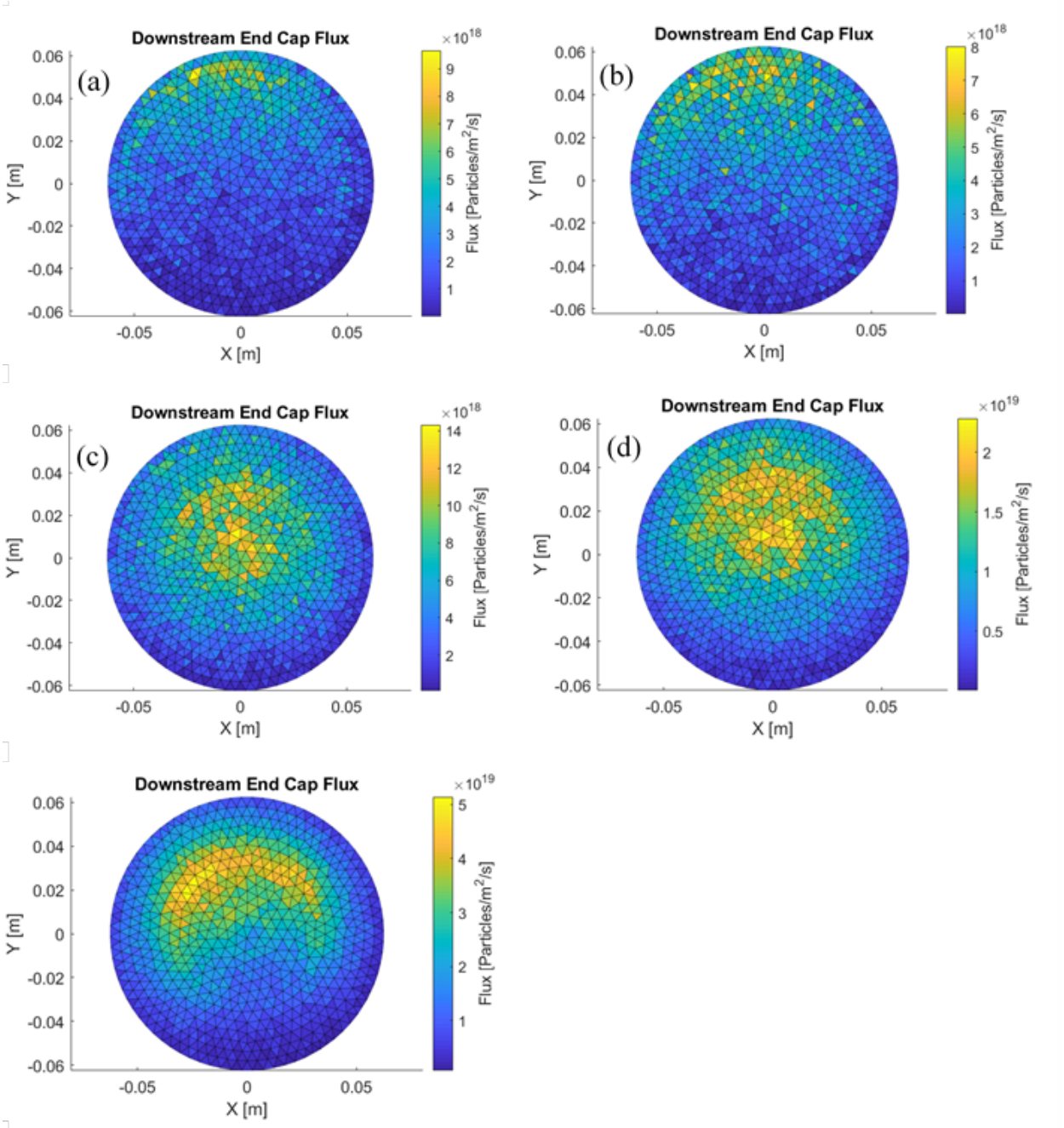


Figure 5.24: The GITR results on the AlN window for the high-density magnetized sheath case at Z=0.2m with flow velocities of (a) $0m/s$, (b) $200m/s$, (c) $5000m/s$, (d) $10000m/s$, and (e) $27000m/s$.

yields for O onto Al. Figure 5.25 gives the sputtering yields used for the O impacting on Al based on the incoming O ion's impact energy and angle. The sputtering yield from O is higher than for D due to it being a heavier particle that can impart more energy to the PKA. This increases the amount of sputtered Al leading to an increase in sputtering downstream Al ion impurity flux. The full-device model with O included is discussed in the next section.

5.5 Full Device GITR Model

To model the full Proto-MPEX device a geometry was created from the dump plate at Z=0.5m to the target at 4.14m using a radius of 0.06m. The helicon window location was adjusted to have the center at Z=1.75m and the sheath potentials on the helicon window were kept the same from the COMSOL simulations. The magnetic field mapping is extended throughout the simulation volume and the velocity of the particles follow the field lines. The density and temperature profiles from the original simulation are now mapped to follow the field lines throughout the simulation volume. The density is also scaled with the magnetic field ratio. The ratio is the magnetic field underneath the helicon (where the profile is originated from) to anywhere else within the machine. This increases the density everywhere else within the geometry because the helicon region has the lowest magnetic field. The ionization of the sputtered Al occurs primarily within the helicon region due to the ionization mean free path being a couple centimeters. For the full device model, the Mach number for the velocity was set to 0.1 under the center of the helicon and rises to one in both directions towards the dump plate and towards the target. Figure 5.26 shows the axial profile used in the simulation for the Mach number. The Mach number profile comes from B2.5-Eirene modeling which was compared to Mach probe measurements taken along the axis of Proto-MPEX [73].

The minimum time set size was set to $1 * 10^{-10}$ s while the maximum was set to $1 * 10^{-7}$ s and the maximum number of time steps was set as $5 * 10^{5}$. An adaptive time step feature was used for these simulations which skips time steps that do not have a particle contact a surface. The surfaces in the simulation are the pure Al helicon window and a boundary surface with sticking coefficient of one elsewhere.

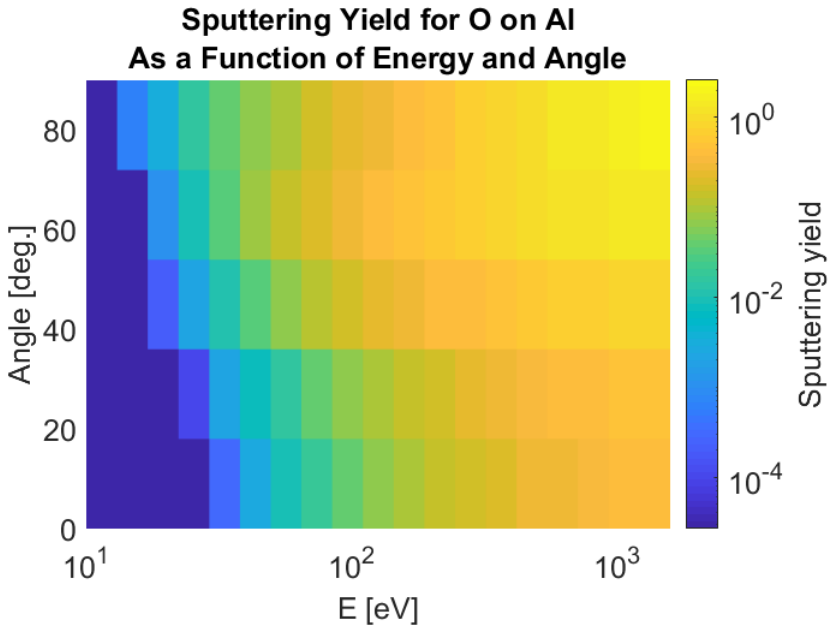


Figure 5.25: The sputtering yields for O impacting onto Al based on the energy and angle, (Ψ), of the incoming ion where the angle is defined as the angle from the surface normal as shown in Figure 2.4.

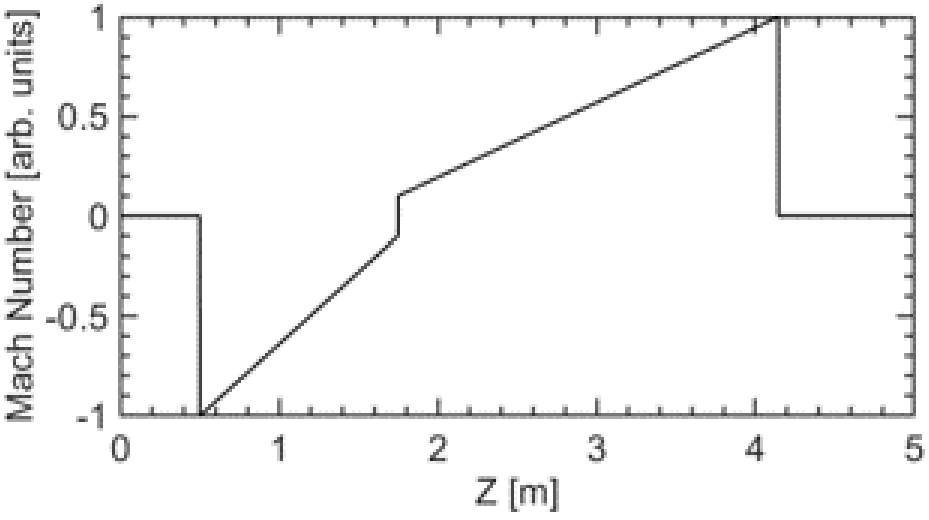


Figure 5.26: The axial Mach number profile used in the GITR full device simulations. The profile starts at 0.1 under the center of the helicon antenna and grows linearly until it is one at the dump plate and the target. The flow towards the dump plate is in the negative direction and positive towards the target for the geometry.

The axial location of the Al ions when the simulation has ended is shown in Figure 5.27. The Al ions follow the magnetic field lines as expected and the highest concentration can be seen under the helicon. At the end of the simulations less than 500 out of the $1 * 10^6$ particles remained within the simulation volume. The final location of each particle is shown in Figure 5.28. The blue particles are particles that have hit a wall while the orange particles within the geometry have not yet hit a surface where they have stuck. Where the magnetic field flairs out the particles can be seen to hit the boundary system. The magnetic field flairs out around Z=0.75 m so no particles are seen on the upstream dump plate facing end cap, but particles do make their way to the target location and can be tallied for comparison to the experimentally seen Al flux.

The results from the full device GITR simulations for the low-density unmagnetized and magnetized case are given in Figure 5.29 and Figure 5.30, respectively. The results for the full device GITR simulations for the high-density unmagnetized and magnetized case are given in Figure 5.31 and Figure 5.32, respectively. The gross erosion, gross deposition, net erosion, and net deposition are the same as the helicon region only simulations. This is due to the low axial velocity in the helicon region.

The results from the full device GITR simulations using O as the ion species inducing Al sputtering for the deuterium background plasma low-density unmagnetized and magnetized case are given in Figure 5.33 and Figure 5.34, respectively. The results for the full device GITR simulations using O as the ion species inducing Al sputtering for the deuterium background plasma high-density unmagnetized and magnetized case are given in Figure 5.35 and Figure 5.36, respectively. The gross erosion, gross deposition, net erosion, and net deposition are larger than the D sputtering of Al simulations as expected. The impurity flux at the target is also greater by an order of magnitude. However, this assumes only O ions induces Al sputtering, but is not the case in Proto-MPEX from looking at the yields from D onto Al which are not negligible. The highest O concentration would be 10% but is likely to be lower than this which will produce a rate that is between the pure D and pure O sputtering yields.

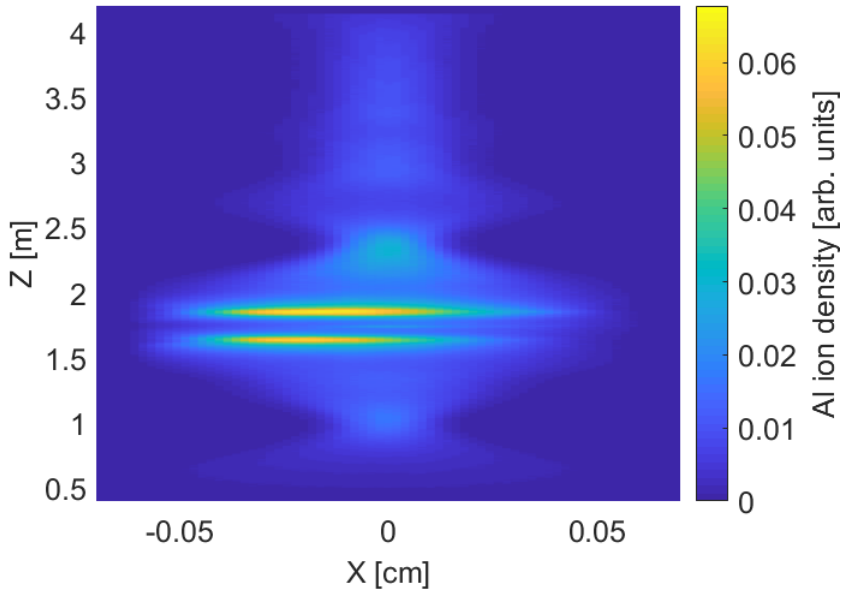


Figure 5.27: The GITR results for the ionized Al axial locations for the high-density magnetized sheath case. The distribution is summed in the Y-direction. The distribution follows the magnetic field profile and is concentrated under the helicon window as expected from the helicon region only results.

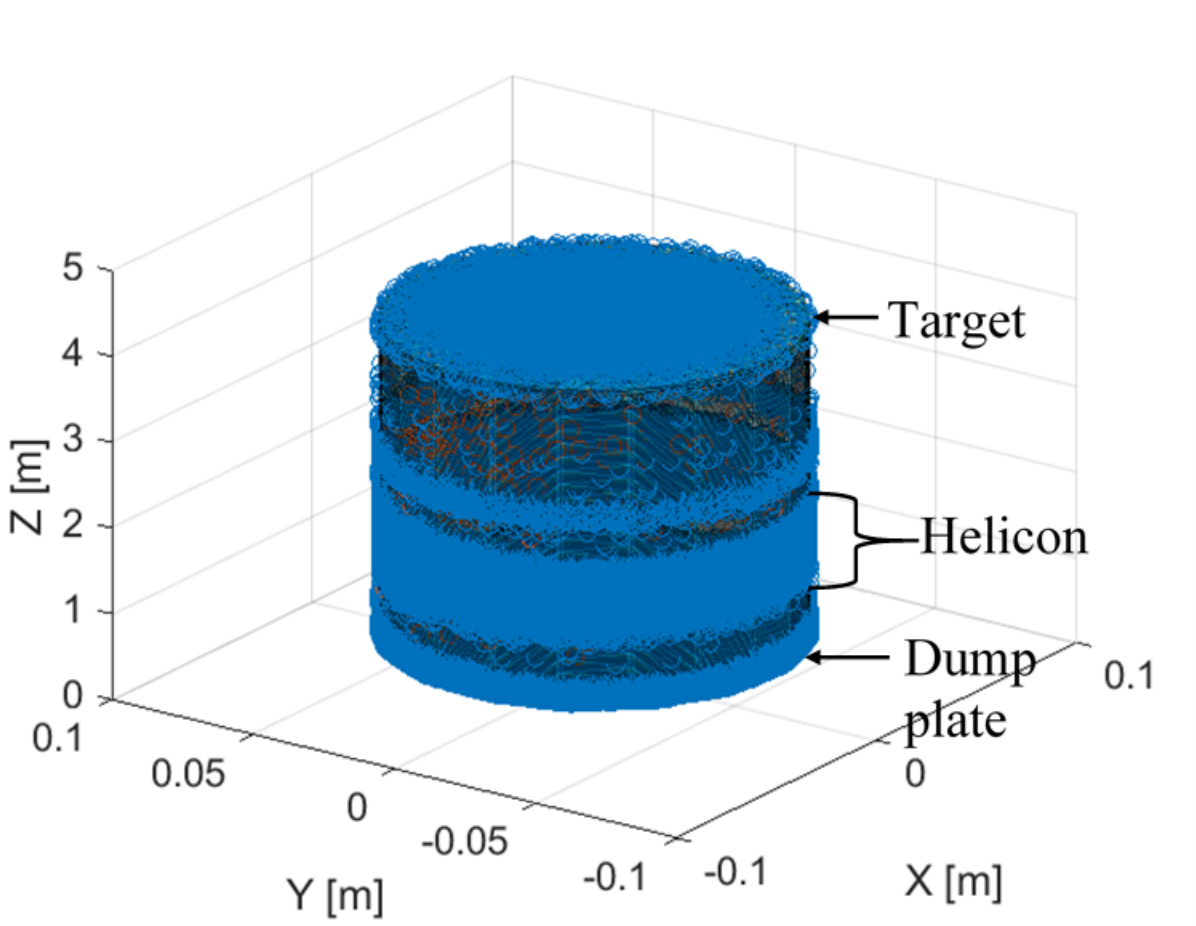


Figure 5.28: The GITR results for the particle deposition locations for the high-density magnetized sheath case. Orange particles have not deposited yet and blue particles have stuck to a surface. Less than 500 particles remain out of the one million introduced. The helicon window is centered at Z=1.75 and is 0.3 m in length, the target is at 4.14 m, and the dump plate is at 0.5 m.

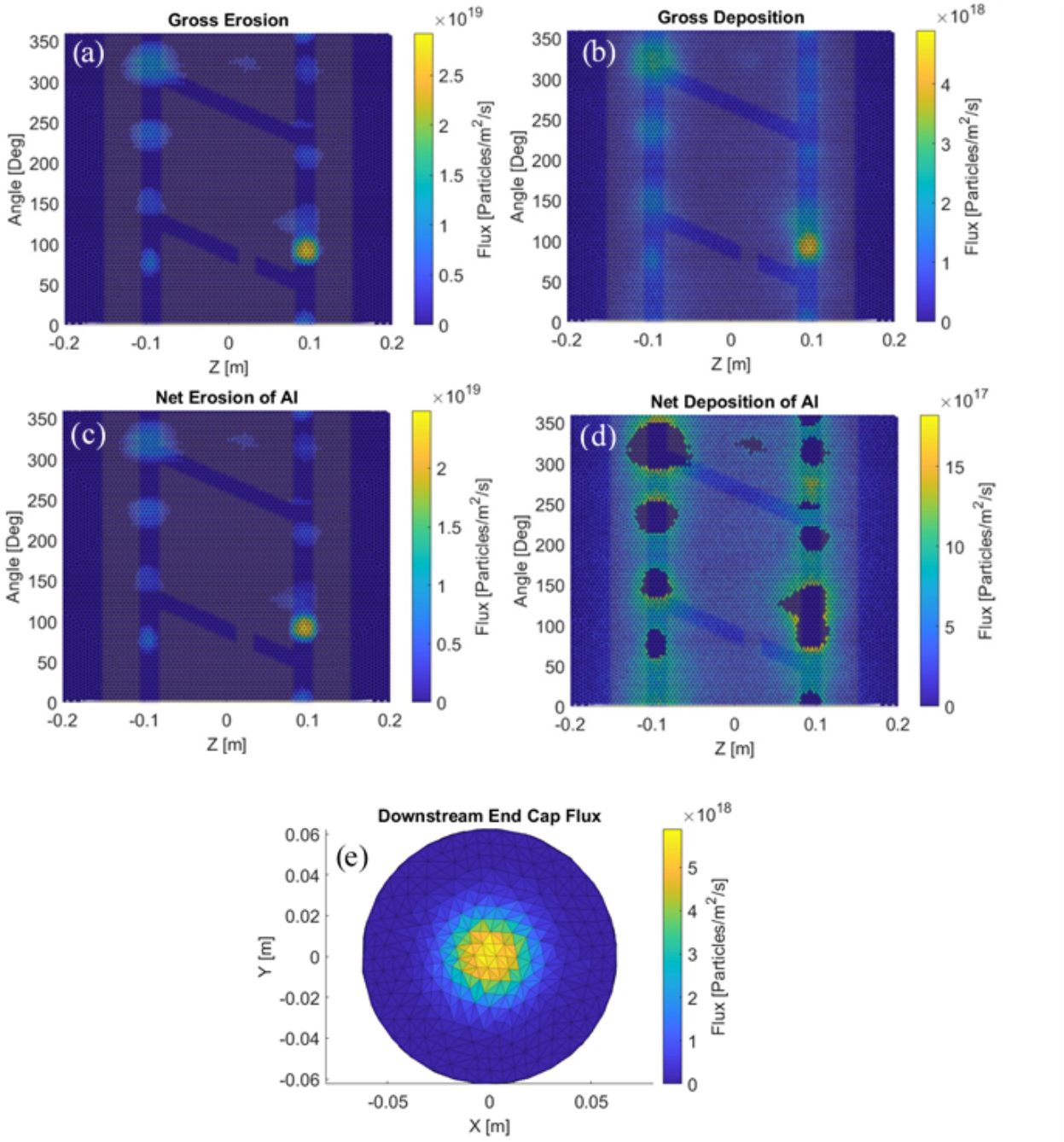


Figure 5.29: The GITR results on the AlN window for the low-density unmagnetized sheath case for (a) the gross Al erosion flux, (b) the Al gross deposition flux, (c) the Al net erosion flux, (d) the Al net deposition flux, and (e) the ionized Al impurity flux at the target at Z=4.14m. The helicon antenna overlay is present on a-d for reference.

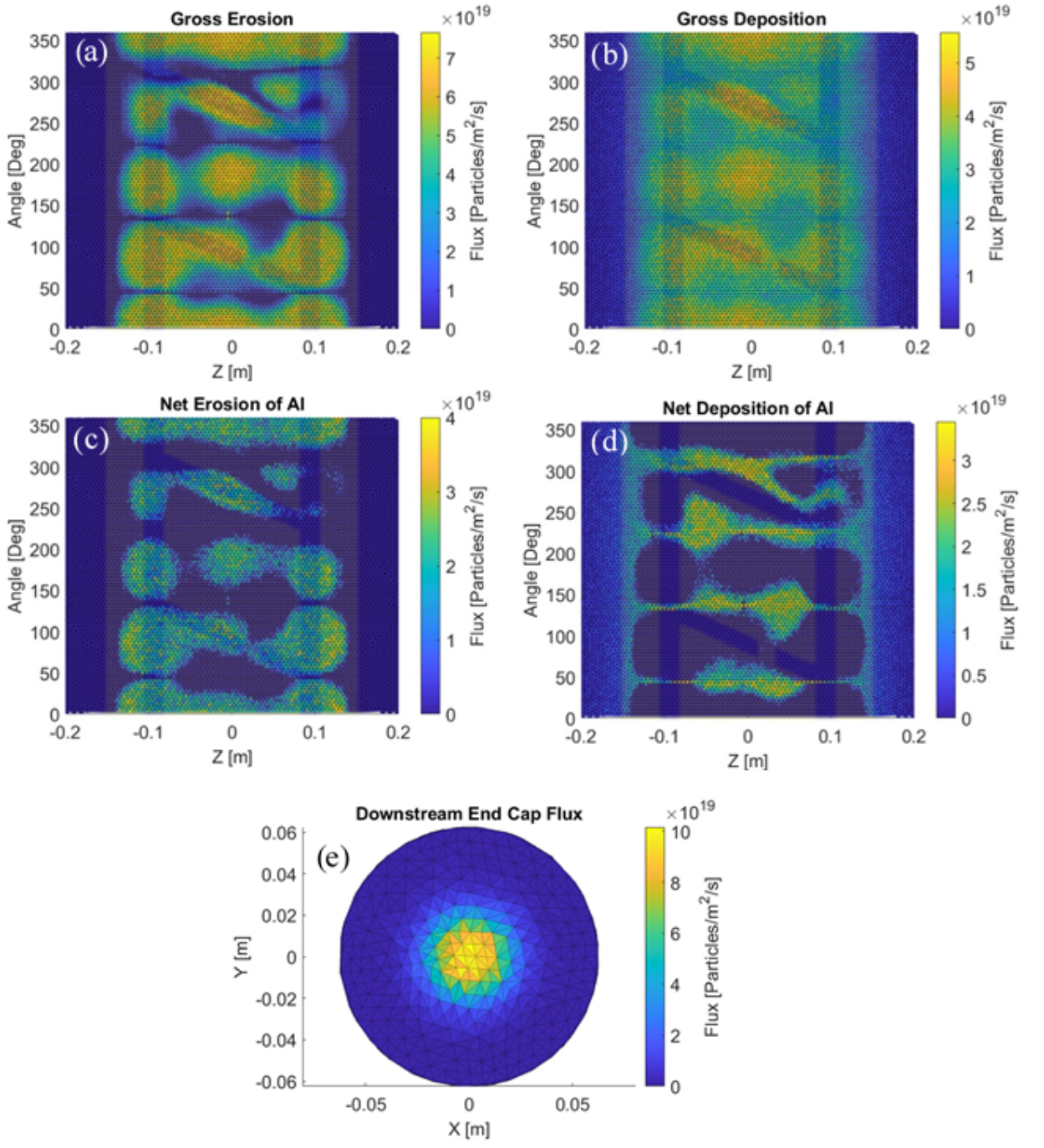


Figure 5.30: The GITR results on the AlN window for the low-density magnetized sheath case for (a) the gross Al erosion flux, (b) the Al gross deposition flux, (c) the Al net erosion flux, (d) the Al net deposition flux, and (e) the ionized Al impurity flux at the target at Z=4.14m. The helicon antenna overlay is present on a-d for reference.

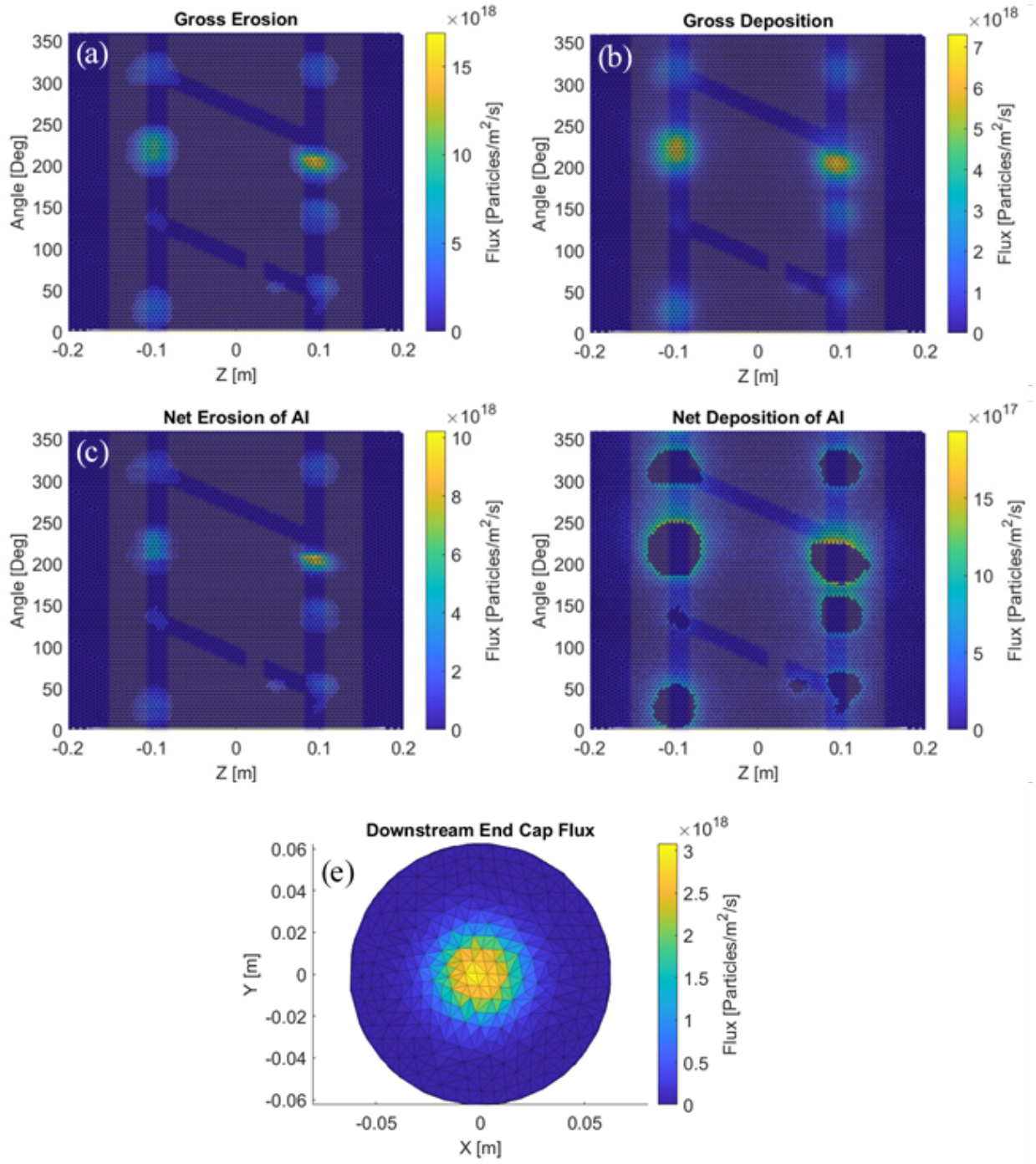


Figure 5.31: The GITR results on the AlN window for the high-density unmagnetized sheath case for (a) the gross Al erosion flux, (b) the Al gross deposition flux, (c) the Al net erosion flux, (d) the Al net deposition flux, and (e) the ionized Al impurity flux at the target at Z=4.14m. The helicon antenna overlay is present on a-d for reference.

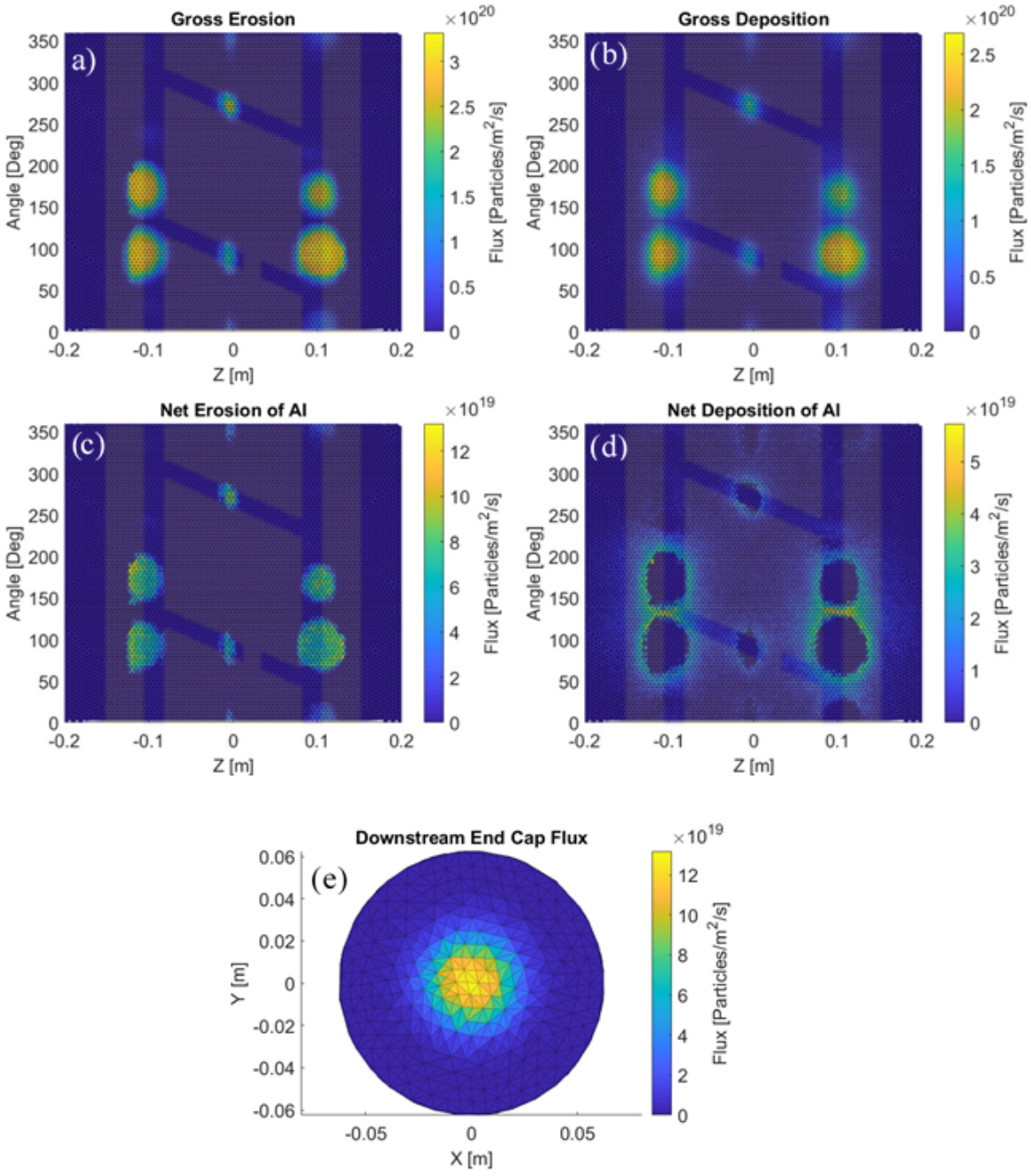


Figure 5.32: The GITR results on the AlN window for the high-density magnetized sheath case for (a) the gross Al erosion flux, (b) the Al gross deposition flux, (c) the Al net erosion flux, (d) the Al net deposition flux, and (e) the ionized Al impurity flux at the target at Z=4.14m. The helicon antenna overlay is present on a-d for reference.

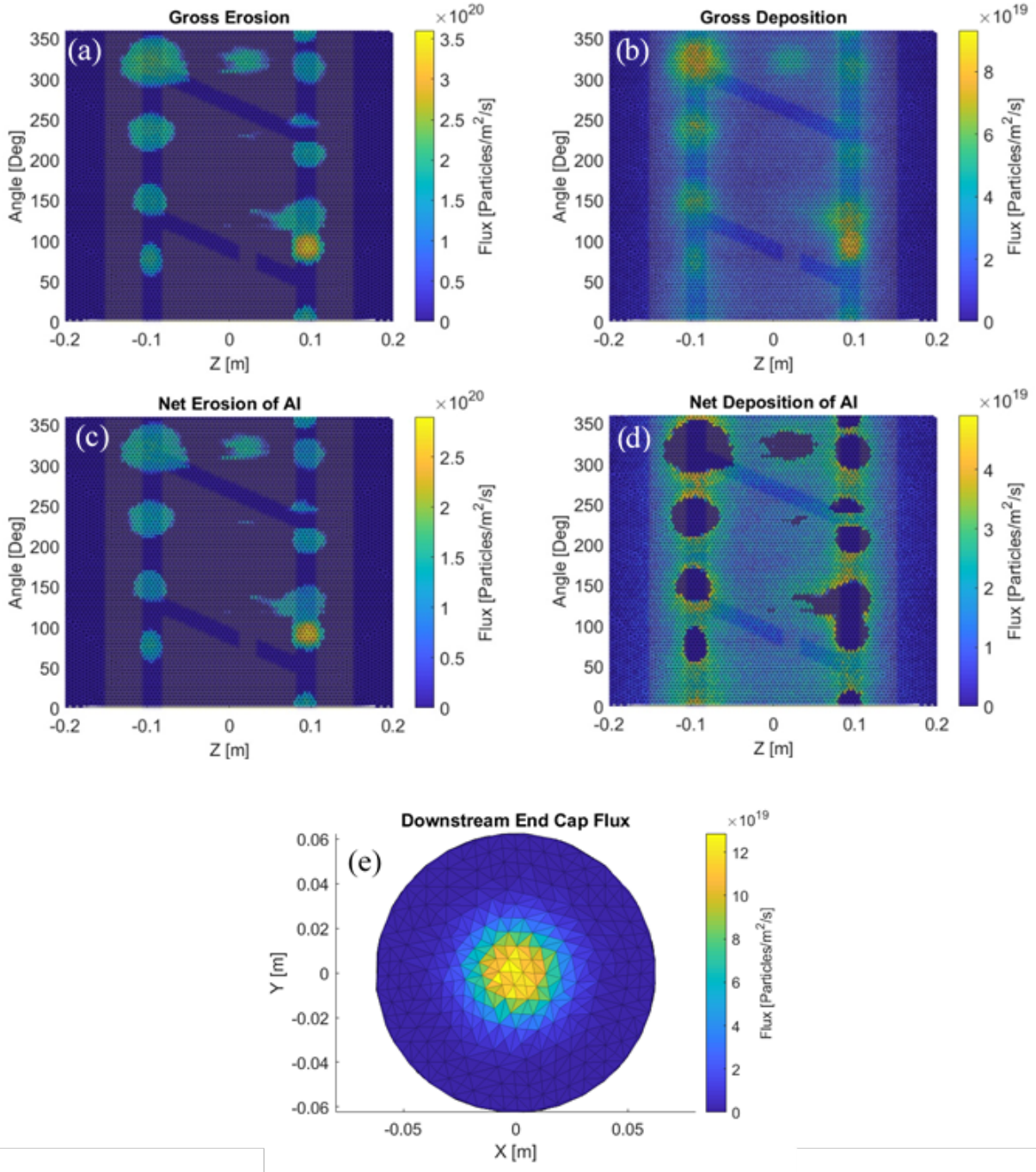


Figure 5.33: The GITR results on the AlN window for the low-density unmagnetized sheath case with O as the sputtering gas for (a) the gross Al erosion flux, (b) the Al gross deposition flux, (c) the Al net erosion flux, (d) the Al net deposition flux, and (e) the ionized Al impurity flux at the target at Z=4.14m. The sputtered Al is transported in background D plasma. The helicon antenna overlay is present on a-d for reference.

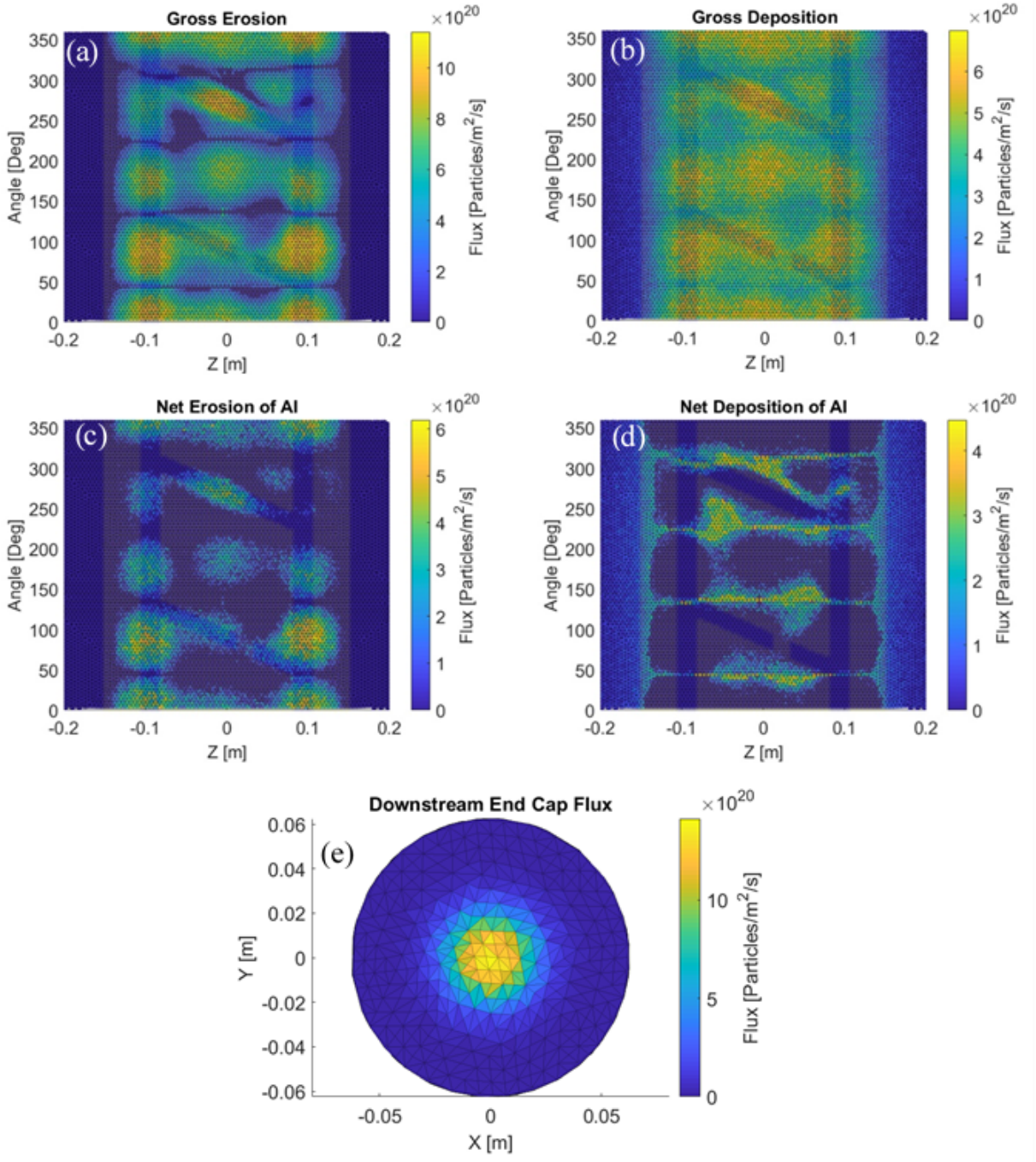


Figure 5.34: The GITR results on the AlN window for the low-density magnetized sheath case with O as the sputtering species for (a) the gross Al erosion flux, (b) the Al gross deposition flux, (c) the Al net erosion flux, (d) the Al net deposition flux, and (e) the ionized Al impurity flux at the target at Z=4.14m. The sputtered Al is transported in background D plasma. The helicon antenna overlay is present on a-d for reference.

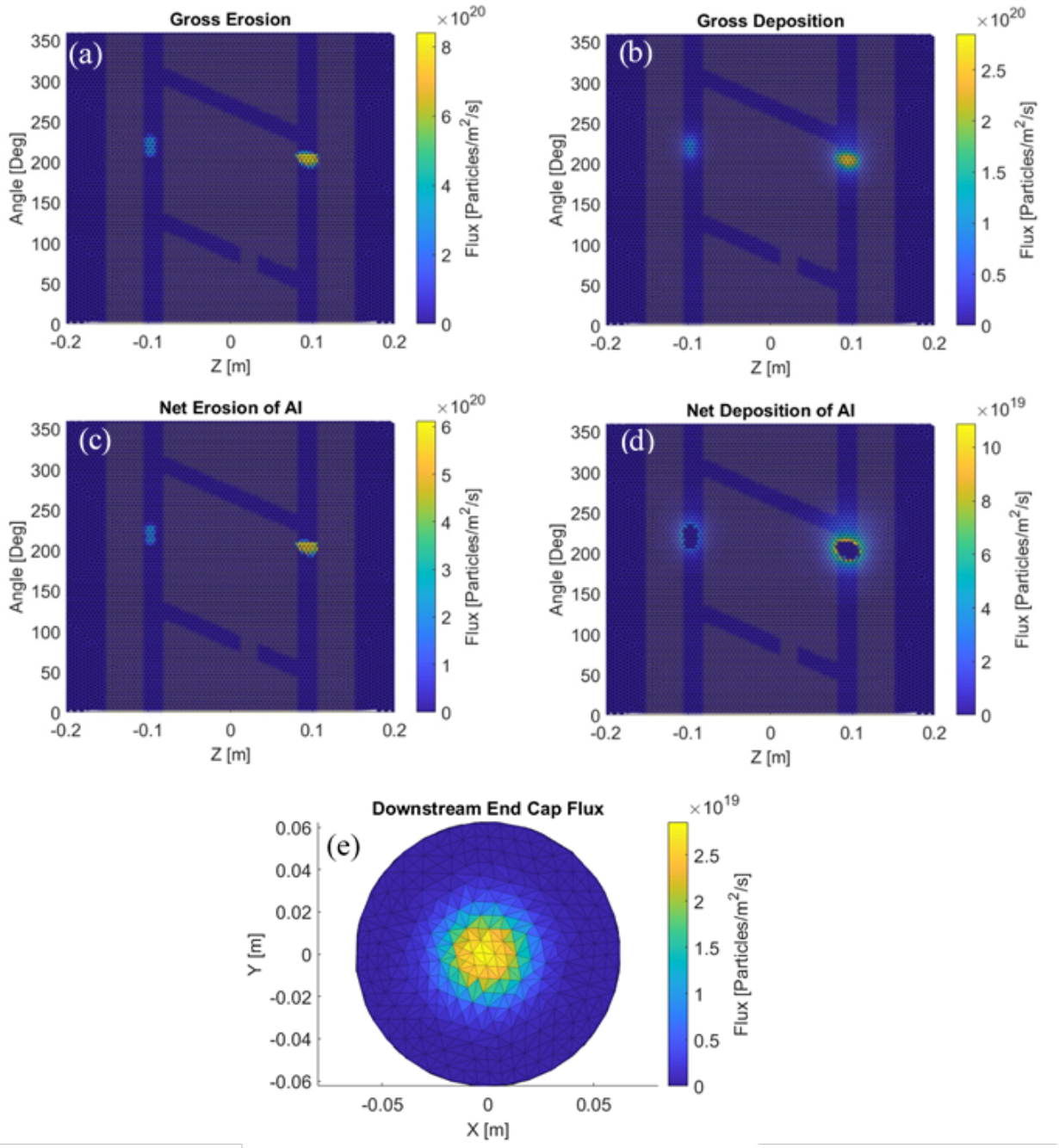


Figure 5.35: The GITR results on the AlN window for the high-density unmagnetized sheath case with O as the sputtering gas for (a) the gross Al erosion flux, (b) the Al gross deposition flux, (c) the Al net erosion flux, (d) the Al net deposition flux, and (e) the ionized Al impurity flux at the target at Z=4.14m. The sputtered Al is transported in background D plasma. The helicon antenna overlay is present on a-d for reference.

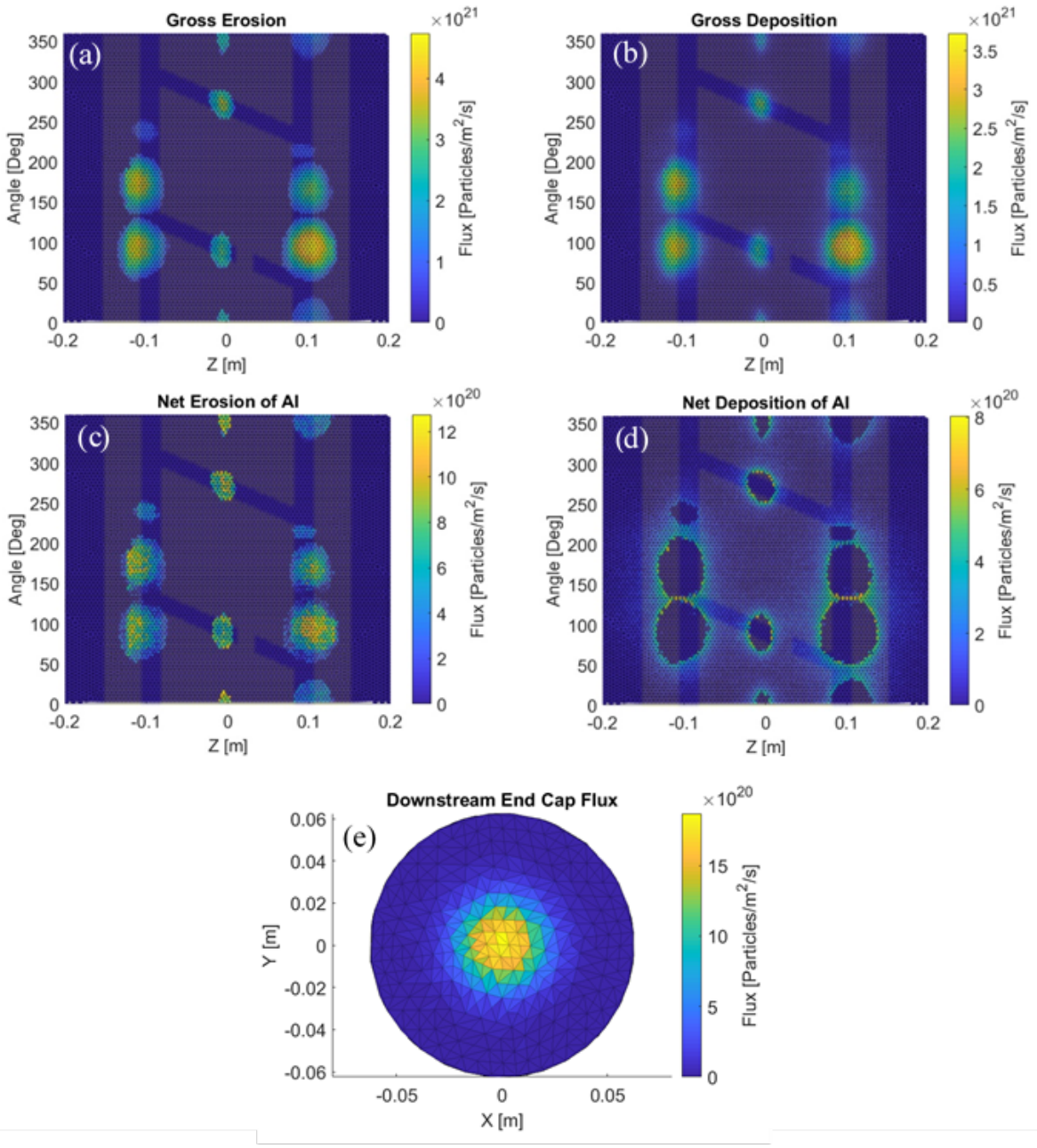


Figure 5.36: The GITR results on the AlN window for the high-density magnetized sheath case with O as the sputtering gas for (a) the gross Al erosion flux, (b) the Al gross deposition flux, (c) the Al net erosion flux, (d) the Al net deposition flux, and (e) the ionized Al impurity flux at the target at Z=4.14m. The sputtered Al is transported in background D plasma. The helicon antenna overlay is present on a-d for reference.

Chapter 6

Discussion and Conclusions

Reproduced from C. J. Beers, C. Lau, J. Rapp, T. Younkin, T. M. Biewer, T. Bigelow, J. F. Caneses, J. B. O. Caughman, D. L. Green, H Meyer III, J. Myra, and S. J. Zinkle, "RF sheath induced sputtering on Proto-MPEX part 2: Impurity transport modeling and experimental comparison," Submitted to Phys. Plasmas

C. J. Beers contribution was the literature review, COMSOL, and GITR modeling, COMSOL and sheath model coupling, sensitivity studies/parameter scans, GITR geometry extension, data collection, data analysis, and manuscript preparation. **C. Lau** advised on the COMSOL and sheath model physics. **J. Rapp** advised on the experimental setup and conditions that were performed for the model input data. **T. Younkin** created the GITR code, the GITR geometry, and advised on GITR operations. **T. M. Biewer** performed the Kr gas mixing and exposures of W targets. **T. Bigelow** operated the ECH. **J. B. O. Caughman** operated Proto-MPEX for several W exposures. **J. F. Caneses** operated Proto-MPEX for several W exposures. **D. L. Green** advised on the modeling approach. **H. Meyer III** collected and analyzed the XPS data. **J. Myra** created the sheath model and wrote the template code used for iterating the coupled solution. **S. J. Zinkle** advised on the manuscript preparation and problem statement.

6.1 Impurity Characterization

6.1.1 Helicon Window Material

The helicon window material (AlN or Si_3N_4) was seen to play a direct role on the impurities that are seen on the MAPP W targets. The AlN had mainly O and Al on the surface while the Si_3N_4 window had predominantly O and Si. This confirmed that the helicon window was the primary source for the impurity production. This was further confirmed from the upstream limiting case where the magnetic field was moved to limit on the stainless-steel vacuum chamber and an increase in Fe was seen on the MAPP target. The stainless-steel components (Fe and Cr) seen on the targets while the AlN helicon window was in and on the AlN helicon window itself come from the stainless-steel flanges that hold the helicon window in place and F comes from the Teflon O-ring that forms the seal between the window and the flanges. The flange design with the Si_3N_4 helicon window had the O-rings recessed further so that they were not exposed to the plasma which resulted in no observed F on the target(s). The N from the window has a low concentration on the targets and is assumed to be lost to the vacuum. The Gibbs free energy of formation at room temperature, $\Delta_f G^\circ$, for NH_3 is $-16.4 kJ/mol$, while NO is $86.6 kJ/mol$ and NO_2 is $51.3 kJ/mol$ [108]. The more negative the value, the more likely the reaction is to occur while a positive value will yield more reactants. The formation of volatile NH_3 is the most likely compound to form with N and is expected to be lost to the vacuum. The Gibbs free energy of formation at room temperature for Al_2O_3 is $-1582.3 kJ/mol$, while AlO_2 is $-91.7 kJ/mol$, and AlH is $231.3 kJ/mol$. This indicates that Al_2O_3 is the most likely to occur compound with Al and NH_3 will form with the N as the O is going to the Al. The ratio of O to Al from the XPS profiles matches the compounds expected to form from the formation energies indicating that Al_2O_3 is the predominant species. Again, here the O is initially likely from the water vapor within the device but after plasma operations, it is oxides on the surfaces within the device. This also matches with the Si compounds. The Gibbs free energy of formation at room temperature for SiO is $-127.3 kJ/mol$, while SiO_2 is $-853.6 kJ/mol$, and $Si3N_4$ is $-647.3 kJ/mol$. SiO_2 will be the most likely to form on the targets and the N will form with H to again form NH_3.

6.1.2 Pulsed Operations

The low-density start-up phase of the plasma pulse is a Trivelpiece-Gould (TG) mode plasma [109] which has a higher power loss at the plasma edge near the helicon [99]. The steady state period has more power absorption in the plasma core which reduces the RF potential on the helicon window. During the pulsed operations for the MPEX-like limiting operations the magnetic field is ramped from the helicon window limiting location to the MPEX-like limiter location. The capacitive probe measurements also corroborate this by showing a high RF potential at the start of the pulse. The steady state time period of the plasma pulse, however, still contributed to a non-negligible RF potential. Experiments to investigate if a shutter that shielded the target from the plasma start-up would result in reduced impurities showed that impurities were not eliminated and the impurity deposition rate was similar to the exposures without the shutter present. A scan of fluence by using single pulse exposures also showed a shift in the slope between the start-up of the pulse and the steady state time period. These data don't show a large offset for the first fluence point compared to the rest of the scan which indicates that the start of the plasma pulse does not contribute significantly to the impurity production; unless a two-step process in the transport is occurring and impurities are transported to the MPEX-like limiter before then moving to the target. This would result in a lag-time in the impurity accumulation at the target. The second point in the fluence scan contributing to the majority of the impurity thickness matches this delayed impurity transport.

Looking at the MAPP target exposures with the AlN helicon window in place a ripple can be seen in the Al impurity concentration. This ripple is more pronounced closer to the surface and the number of ripples matches with the number of plasma pulses. The samples also show a spike in C concentration at the surface which would be deposited on the target after the plasma pulse. Heat flux during a plasma pulse causes the carbon that is deposited between plasma pulses to diffuse in the layers that are deeper in the accumulated impurity layer. The O signal which follows the opposite trend of the C is brought to the target during the plasma pulse and covers the carbon that is deposited between plasma pulses which reduces its concentration. The oxide growth for room temperature W after one hour

is 1 nm [110] which is much thinner than the measured O variation which also indicates the O is brought to the target from the plasma pulse.

The MAPP tungsten targets were not heated for the exposures which also increases the sticking coefficient leading to a higher accumulation of impurities on the target as the target cools between plasma pulses. The targets are grounded which increases the electric field and plasma density and temperature in front of the target [111] which is desired for MPEX as it is to operate in the conduction-limited regime [73]. The higher density and temperature will lead to higher target temperatures, (without cooling) which will lead to a decrease in the impurity accumulation on the target.

6.1.3 Density and Temperature Sensitivity

The modeled case with the higher density showed a reduction in the magnitude of the RF sheath potential on the helicon window. This can be attributed to a higher current density going to the helicon window and a reduction in the sheath impedance. The lower impedance reduces the sheath potential on the helicon window.

The temperature plays a role in the location where the sputtered material is ionized. For a high edge electron temperature, the ionization mean free path is shorter and the material is likely to redeposit on the window. The steady state part of the plasma will allow for a lower electron temperature in the helicon region. The reduced electron temperatures will cause more of the sputtered material to not be ionized and to travel to either the opposite locations of the helicon window to be lost to the vacuum chamber.

Auxiliary heating (ECH and ICH) within Proto-MPEX will alter the electron and ion density and the electron and ion temperature profiles but when the auxiliary heating is absorbed in the plasma core additional impurities will not be created. The experiments with ICH that did not show Al on the target from the Al_2O_3 ICH window confirm this. If the ICH auxiliary power is absorbed in the plasma edge near the ICH window, increasing the density and flux to the ICH window, then some sputtering of the window is plausible. The ECH O-X-EBW wave conversion also depends on being absorbed in the core and not near the launcher, otherwise, sputtering of the launcher is plausible.

6.1.4 Limiter Operations

The introduction of the stainless-steel limiter was done to reduce the heat flux on the helicon window and to reduce the plasma flux limiting on the helicon window while providing a higher-Z material with a higher sputtering yield for reducing the overall impurities within the device. Looking at the deposition thickness for the two helicon window operations in the MPEX-like limiting configuration, the AlN helicon window had a deposition thickness of 381 nm and the Si_3N_4 helicon window was 440 nm for a fluence of $1 * 10^{24}\ m^{-2}$. The limiter operations were a reduction from the 497 nm layer thickness for a fluence of $1 * 10^{24}\ m^{-2}$ in the AlN helicon window limiting case. Both window exposures with the MPEX-like limiter still showed Al and Si for the AlN and Si_3N_4 windows, respectively.

6.1.5 Role of Oxygen Content

Oxygen is seen throughout the deposition thickness from the XPS results, and the role of O within the device has not been explored yet. Some oxidation of the target's surface will always occur and is typically within the first 10 nm. The layer thickness is much thicker than this, indicating that O is present throughout the pulse. The helicon window also showed O throughout the several micron thick layer which may indicate that the helicon window could be the source of the O. As shown from the Gibbs free energy of formation Al does like to form oxides so the helicon window is likely a location of preferential O accumulation. The initial source of O is from water vapor as measured with residual gas energy analyzer on Proto-MPEX near Z=0.5 m which has a partial pressure of 30% of the $6.67 * 10^{-4}$ Pa base pressure. Proto-MPEX does not employ a full device baking operation of the vacuum vessel to outgas the surfaces. Oxygen being heavier than deuterium will increase the sputtering yield and lead to an increase in impurity generation. The oxides on the helicon window may lead to additional self-sputtering which were not considered with the GITR model.

6.1.6 Baking Operations

The hypothesis that reducing the O content within Proto-MPEX in the device would lead to a reduced impurity accumulation on the target was tested by a baking operation on

Proto-MPEX. A fluence scan after the baking was compared to pre-baking and resulted in no reduction in the rate of impurities to the target. The base vacuum level didn't decrease much after the baking operation but from RGA measurements the O fraction was the same or slightly higher (30-40%). This leads to the same overall O levels in the device and no observable change at the target. The heating tapes were not able to heat the whole machine uniformly and the temperature limit for the O-rings on the helicon window is 100°C which is lower than needed for a successful baking operation within a time limit of a couple of weeks. Thus, the baking likely didn't reduce the oxygen on the helicon window and could even make the O that is released from the vacuum vessel move to the colder helicon window and condense there. A higher bakeout temperature and/or longer baking operation across the whole device is advised for MPEX to keep the O levels lower. The O concentration on the helicon window should also be kept low by heat treatment of the window and monitoring the O concentration in the gas inlet lines.

6.2 Target Impurity Flux

To compare to the experimental deposition on the target the flux to the target needs to be converted to a fluence. The time taken for the start-up of the plasma pulse is 0.07 s, and the remainder of the 0.5 s pulse is assumed to be at a steady state. This puts the exposure at 0.568 s of starting density and 3.432 s of steady state density. The density of the amorphous layer is assumed to be 2.35 g/cm^3, and the monolayer thickness is assumed to be $1.15 * 10^{-10}$ m [112, 113]. This gives a total impurity fluence of $1.7 * 10^{22}$ $atoms/m^2$. From the XPS profiles, Al accounted for 35 % bringing the Al impurity flux to the target to $5.8 * 10^{21}$ $atoms/m^2$. The accuracy of this value is also dependant on the assumed layer thickness. SiO_2 is the calibration material used to get the depth for a given sputtering time and Ar ion energy. A difference between the sputtering rate of Al_2O_3 and SiO_2 can also lead to the difference in the number of monolayers on the target. The sputtering rate differences of these two have been reported to be up to 53% smaller for Al_2O_3 than for SiO_2 [114] which will reduce the thickness of the impurity layer from experiments with the AlN window in place. The initial layer thickness will be used here to compare to the impurity flux from the

GITR model at the target. The flux is taken at the center 0.012 m diameter of the simulation geometry. The fluxes and fluences (using the starting density timing and the steady state density timing) from the four modeled cases are given in Table 6.1. Using a combination of the four modeled cases gives a difference from the experimental range of a factor of 172 to a factor of 13 lower where the unmagnetized electron sheath limit gives the lower bounds and the magnetized electron sheath gives the upper bounds. To further investigate the cause for the remaining difference, the role of O was investigated.

Additional full device GITR simulations were run for the four modeling cases to get the erosion, deposition, and impurity flux profiles while using pure O as the gas species that induce sputtering. The flux and fluence for Al ion impurities at the target due to sputtering by O are given in Table 6.2. Oxygen as the only sputtering element gives a difference of a factor of 38 to a factor of 0.9 lower than the experiment. Pure O is not a physical result, however, but up to 10% could be possible within a Proto-MPEX due to poor vacuum quality. This 10% change in plasma background species can alter the transport of the Al but is beyond the scope of work performed here. The simulation results using a combination of 90% D and 10% O yields a range of a factor of 127 to 5.6 lower than the experiment. The magnetized cases provide the upper bounds which are closest to the experiment and Proto-MPEX is assumed to be operating with a magnetized electron sheath condition based on this.

The discrepancy from the model to the experiment could come from the measured electron density and temperature profiles near the helicon being extrapolated to the target. The exact density and temperature underneath the helicon cannot be known based on the optical view ports on Proto-MPEX and physical probes disturbing the helicon mode transition to achieve the high-density plasma pulse. A higher density underneath the helicon antenna would lead to a lower sheath potential but the higher density would be a higher ion flux resulting in a net reduction in sputtering yield due to the large reduction of RF sheath potential. The higher edge density of $1 * 10^{19}\ m^{-2}s^{-1}$ reduced the sheath potential on the helicon window by a factor of 33 while increasing the ion flux by a factor of 10. A flatter radial density profile would also flatten the impurity profiles based on the density gradient term in the classical impurity convection velocity. A higher electron temperature would lead to a decrease in the

Table 6.1: The Al ion impurity flux and fluence at the target for the modeled conditions.

Condition	**Al Ion Impurity Flux** $[m^{-2}s^{-1}]$	**Al Ion Impurity Fluence** $[m^{-2}]$
Low-density unmagnetized case	$5.1 * 10^{18}$	$2.9 * 10^{18}$
Low-density magnetized case	$9.0 * 10^{19}$	$5.1 * 10^{19}$
High-density unmagnetized case	$9.0 * 10^{18}$	$3.1 * 10^{19}$
High-density magnetized case	$1.1 * 10^{20}$	$3.9 * 10^{20}$

Table 6.2: The Al ion impurity flux and fluence at the target with O as the sputtering species for the modeled conditions.

Condition	**Al Ion Impurity Flux** $[m^{-2}s^{-1}]$	**Al Ion Impurity Fluence** $[m^{-2}]$
Low-density unmagnetized case	$1.1 * 10^{20}$	$6.5 * 10^{19}$
Low-density magnetized case	$1.2 * 10^{21}$	$7.0 * 10^{20}$
High-density unmagnetized case	$2.54 * 10^{19}$	$8.7 * 10^{19}$
High-density magnetized case	$1.7 * 10^{21}$	$5.7 * 10^{21}$

ionization mean free path and an increase in the ionization states of the impurities. The higher ionization states cause the impurities to drift faster than the singularly ionized D. A higher core electron temperature would lead to a temperature screening and a reduction of the impurities on the target. The axial profiles within Proto-MPEX are ignored within this work but the ECH and ICH on MPEX will alter the profiles which can lead to impurity screening both radially and axially. The pure crystalline Al surface assumption for the sputtering yields is also not correct based on the composition seen on the helicon window. Due to the years of operation and erosion/re-deposition of the helicon window led to a change in surface composition and displacement energy thresholds. Patino et al. [41], saw an Al enrichment on plasmas exposures of AlN which would match the sputtering rates used on the areas with a high RF sheath potential but where deposition is higher than the erosion the Al_2O_3 layer would have a 50% reduction in sputtering yield over pure Al [115]. The assumptions in the density of the impurity layer thickness also do not consider the trace impurities which could lead to a difference in impurity flux needed to achieve the measured thickness. The XPS technique does not measure H/D within the sample which can reduce the concentration at.% for the other detected elements if present in the layer and would reduce the Al ion impurity flux to the target that is compared to the modeling. The sputtering rates used for SiO_2 on the predominantly Al_2O_3 will also reduce the monolayers by up to 50% due to the differences in sputtering rate [114]. The trace impurities on the target are also higher-Z elements which will increase the sputtering rates of the helicon window leading to an increase in impurity production. Additionally, the modeled GITR geometry has a fixed radius of 0.06 m which is not true for Proto-MPEX, and some of the particles were lost to the wall at points where the field flairs out. However, this simple geometry case still matched the expected classical radial impurity transport.

6.2.1 Helicon Window Deposition Profile

The experimental deposition profile on the helicon window matches well to the modeling profile for the magnetized electron sheath cases. Figure 6.1 shows the helicon window pattern, the low-density magnetized, and the high-density magnetized case. Point X on the window shows a deposition location, point Y shows the circular clean region under the helicon

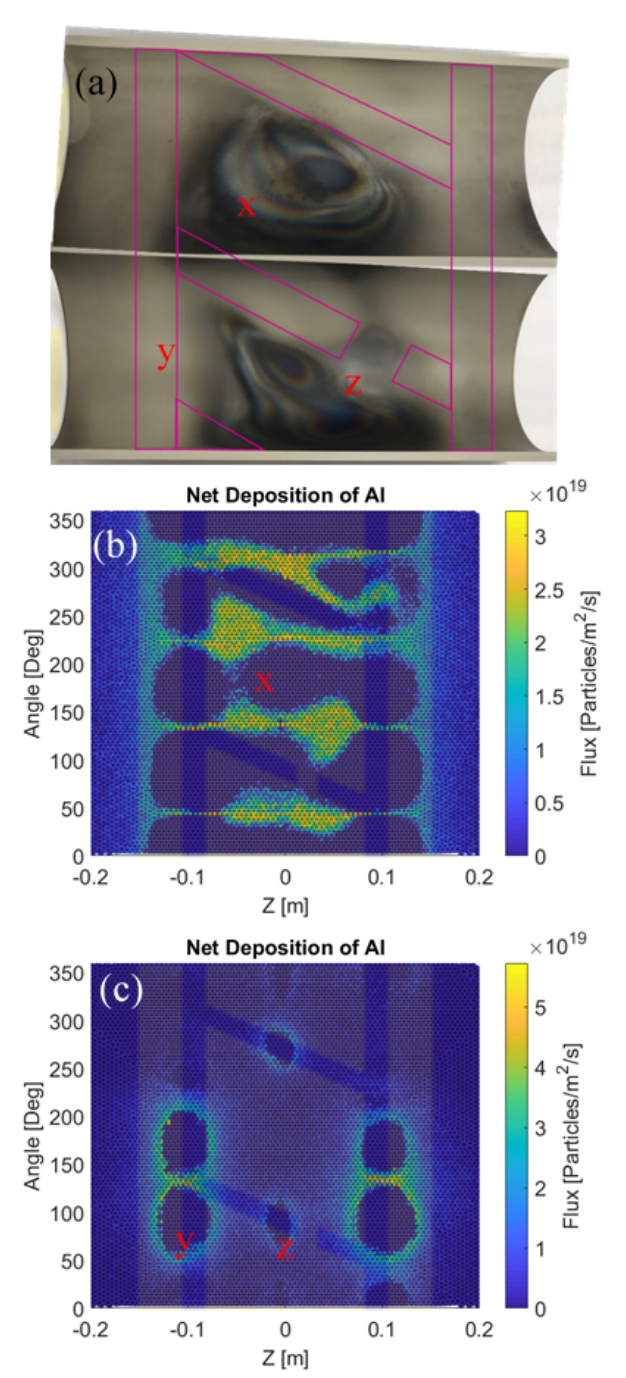


Figure 6.1: (a) The helicon window deposition pattern with helicon overlay in magenta, (b) the low-density magnetized case's net deposition with helicon pattern shown in dark blue, and (c) the high-density magnetized case's net deposition with helicon pattern shown in dark blue. The points X (deposition), Y (no deposition), and Z (location between the feed and ground connections on the helicon antenna) indicate regions from the model that match the pattern on the helicon window.

antenna, and point Z shows the break in the antenna with a circular deposition pattern on the edge. These points indicate that the model is accurately capturing the erosion and redeposition happening on the helicon window. The AlN helicon window has been used on Proto-MPEX for 3+ years under several different heating scenarios and varied magnetic field profiles which are the likely cause for any differences seen. As the helicon window was sputtered initially and redeposits back on the window, the material properties change, i.e., the sputtering yield, surface composition, and the sheath impedance as the thickness of individual locations changes. The modeling does not reflect some of these changes and assumptions were used about them, i.e., the pure Al surface for sputtering yields and uniform window wall thickness.

6.2.2 Radial Scan

A radial scan was performed with the MAPP W targets while the Si_3N_4 helicon window was installed to collect exposures at the on-axis, 1 cm off-axis, and 2 cm off-axis locations to experimentally investigate the radial ion locations. Figure 6.2 gives the normalized experimental results for the 3 axial locations along with the normalized GITR axial Al impurity profile for the high-density magnetized case at 1 cm in front of the target. The profile shows good agreement in the fall-off length and indicates that the extended GITR geometry accurately captures the radial impurity ion convection velocity. The Al and Si are comparable in mass (27 versus 28 amu) and ionization energies (6 versus 8 eV), so they are compared here because they will be transported similarly. The inward radial impurity drift will be similar for Al and Si due to their similar mass, charge states, and the plasma conditions being similar.

Due to the size of the geometry, namely the 0.06 m radius, used in the GITR simulations some of the particles hit the wall whereas, in Proto-MPEX, the radius in locations between the helicon window and the target is larger than 0.06. Particles that hit the boundary and stick will not be transported to the end of the target to be counted in the Al ion impurity flux. This leads to a lower impurity flux from the simulation than experimentally seen.

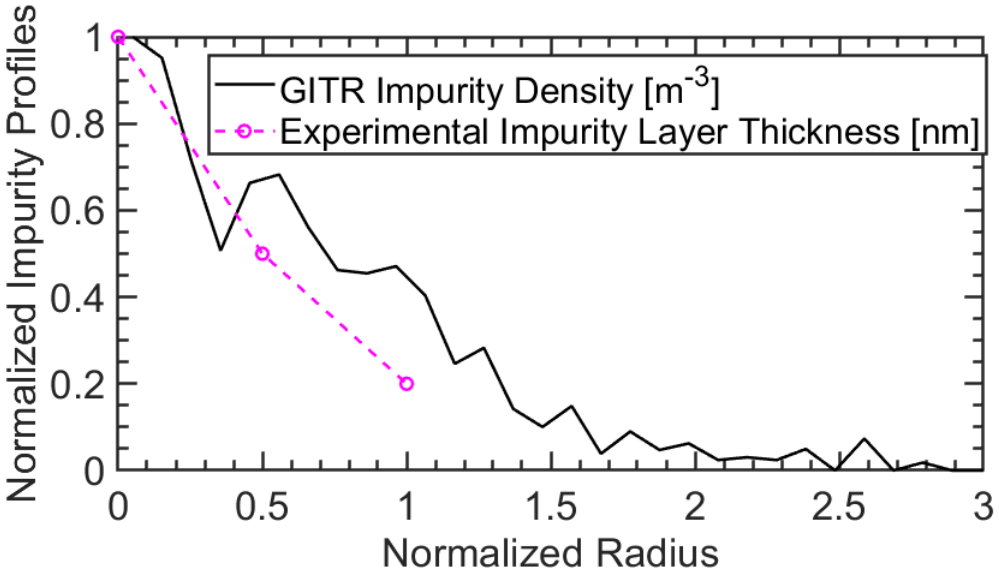


Figure 6.2: The normalized impurity layer thickness with the Si_3N_4 helicon window at the normalized locations for the plasma center, one cm off-axis, and two cm off-axis along with the normalized GITR radial ionized Al impurity density 1 cm in front of the target location.

6.2.3 Role of Temperature Screening

Seeing that the ECH and ICH have both reduced the impurities seen on the target it is likely that the impurities are being screened via the classical impurity drift velocity from Equation 2.50. The classical drift velocity for a typical high-density helicon plasma at the helicon region without ECH or ICH present (no thermal gradient) is shown in Figure 6.3. The data shows that the impurities should move inward to the plasma core which will occur as the plasma flows along the axis of the machine from the helicon region to the target. The presence of ECH and ICH will modify the thermal gradient and reverse the drift velocity causing impurities to move radially outward.

6.2.4 Exposures with Kr

The depth profiles show a reduction in impurity layer thickness when ECH is introduced, and the Kr addition further reduces the impurities on the surface. The ECH enhances the temperature gradient leading to impurities being screened from getting to the plasma core. A 44% reduction in the impurities on the target for the 100 ms ECH pulse can be increased by increasing the pulse length and the input power. The higher power will also lead to additional sputtering of impurities that do make their way to the target. Kr with ECH reduces the impurity thickness to 7% of the original thickness which comes from the heavier Kr atoms sputtering the deposited material that is on the target. This heavier element will sputter more of the helicon window but the ECH being closer to the target gives the Kr more energy to sputtering the target than the window.

6.3 Conclusions

The linear plasma device Proto-MPEX has demonstrated high-density helicon D plasma pulses with evidence of plasma heating using auxiliary ion and electron heating towards its plasma source R&D for MPEX. During the first PMI studies on Proto-MPEX, impurity deposition has been observed on the helicon window and the exposed sample targets. Al and Si at the target were shown when using an AlN or Si_3N_4, respectively, along with a large

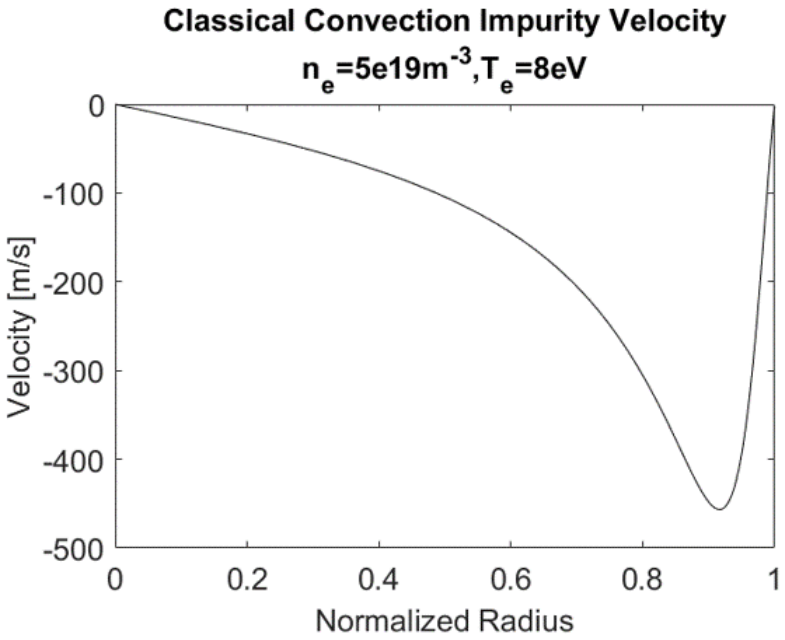


Figure 6.3: The classical impurity convection velocity calculated for the Proto-MPEX's conditions near the helicon window.

O concentration, and trace F, Fe, Cr, and N concentrations. These results indicate that the helicon window was the source of the Al or Si impurities. The O is thought to come from background water vapor within the device. Analysis of the formation energy for the elements seen on the helicon window and target showed that Al_2O_3 or SiO_2 will likely form which matches the ratios seen at the target and that N is likely lost to the vacuum as NH_3. Capacitive probe measurements at the plasma edge confirmed the hypothesis that the RF sheath potential was the cause for impurity generation due to physical sputtering of the helicon window. The RF potential was also found to spike at the beginning of the pulse during the low-density TG mode plasma, which would lead to more sputtering. Modeling of the RF sheath potential in the two-density regimes to further understand the impurity generation was performed with the COMSOL FEA Multiphysics simulation software coupled with a sheath impedance matching iterative routine to provide the DC rectified RF sheath potential imposed on the helicon window as a function of the electric field normal to the window. This novel technique uses a thin dielectric layer that simulates the sheath impedance which can be meshed in the global device geometry. This technique yields 3D mapping of the sheath potential over a larger device relevant geometry. Hot spots on the helicon window that are underneath the helicon antenna were found that were up to 1000V. Proto-MPEX's plasma conditions near the helicon window are in a regime between the unmagnetized and magnetized electron boundary which prompted additional studies which indicated that the magnetized electron boundary limit is correct for Proto-MPEX. The highest potentials were found for the low-density magnetized regime while the high-density case maximum potential was up to 500V. The RF sheath potentials showed a trend of increasing with increasing helicon power and decreasing with increasing electron density near the helicon window. The sheath potentials coupled to the F-TRIDYN BCA code were used to obtain the window sputtering rates for D onto Al. The window was assumed to be clean pure Al due to limitations in the current codes and the trace N concentration observed on the targets. The sputtering rate was coupled to the GITR code to yield self-sputtering (Al onto Al), deposition, and impurity fluxes on the helicon window and at the target. The deposition pattern on the helicon window matched those of experiments with agreement on discolored areas being deposition regions and erosion areas that were "clean" regions. To match the

impurity rates to the target within a factor of 2 to 3, sputtering due to O was needed to be included indicating that O and likely the other trace impurities are contributing to a significant portion of the impurity generation. The simulation impurity rates to the target also indicated that the low-density and high-density plasma times each significantly contributed to the impurity rates to the target. To understand the low-density and high-density contributions to the target impurity rate experiments with a shutter placed in front of the target that only allowed plasma to reach the target during the high-density part of the plasma pulse. No reduction in the impurity rate to the target was measured for the plasma pulses with the shutter when compared to pulses without the shutter. The high-density part of the plasma pulse is not negligible for impurity production and accumulation on the target which matches the modeling results. The radial impurity transport is consistent with classical transport and experiments measuring the radial impurity profiles also agree. The radial impurity deposition is peaked in the plasma core and falls off over a few cm. Experiments to move the plasma limiting location off the helicon window and onto a stainless-steel limiter were performed and showed that a reduction in the target impurity rate by a factor of 2 occurs when limiting on a clean higher-Z material. Baking of Proto-MPEX to reduce the O background concentration did not result in a reduction of the impurity rate to the target which indicates that the O that is already on the helicon window surface is the likely source of O target impurities within the device. Experiments with ECH present and an additional experiment with ECH and a 3% Kr gas seeding showed a reduction in the impurity accumulation on the target by a factor of 2 and 5.7, respectively. The increase in electron temperature leads to additional sputtering Increasing the length of the ECH pulse will likely further decrease the total accumulation at the target.

6.4 Implications for MPEX

Based upon the target exposures, impurity characterization, and modeling performed on the helicon region of Proto-MPEX some key observations and recommendations can be given for MPEX and other devices that make use of RF. The O and other trace impurities around RF sources should be kept to a minimum and a more extensive bakeout process on MPEX

should be used than what was performed on Proto-MPEX to further reduce the O levels. The helicon window should be heat treated to reduce the residual O within the window before first plasma operations to reduce the oxides that can form on the helicon window. The limiting location should still be off the helicon window and be placed upon a clean higher-Z material to reduce sputtering from the fueling gas which can occur due to the high sheath potentials on the helicon window. The higher operating helicon power with MPEX will also lead to a higher RF sheath potential on the helicon window which will increase the sputtering yield. The higher power will increase the core-density, but the low-density edge plasmas will still be present which had the highest sheath potentials from the Proto-MPEX models. No flux lines map from the ICH window to the target which is likely why no additional impurities were observed on the target during ICH operations. The ICH window is also not a limiting surface, which will reduce the plasma flux and ultimately the sputtering occurring, but additional simulations of the ICH antenna operations are recommended. A target shield is not needed for operations because the high-density part of the plasma pulse contributes significantly to impurity accumulation at the target based on the shutter experiments and the modeling. The radial profiles followed classical impurity transport which can lead to radial temperature screening of impurities by creating a core peak electron temperature in MPEX when the ECH and/or ICH are present. The core peaked temperature will reduce the impurities that are transported to the core of the plasma.

6.5 Future Work

Additional analysis of the target's depth and composition would be beneficial for a better comparison of the experiments to the modeling. Further analysis of the thickness of the layer should be performed with an additional technique to better know the impurity accumulation rate at the target. Ellipsometry of the Ar milled location and across the fringe bands could be performed to measure the thickness of the deposition layers over a wider area. Additional measurements on the composition should be done which can detect H/D within the sample. The impurity concentrations on the targets would reduce if the amount of H/D present in

the layers is significant. Glow discharge optical emission spectroscopy (GD-OES) could be used to analyze all the impurities present on the sample simultaneously.

Future modeling work for MPEX should include auxiliary heating density and temperature profiles. Experimental DLP (or Thomson scattering) data should be taken for creating additional axial and radial profiles for the modeling to bound the parameter space. The impurity transport modeling with auxiliary heating will determine if the temperature screening effect can be used to eliminate impurities from making their way to the target. The use of an updated binary collision approximation code that can handle multi-component surfaces for calculation of the sputtering yields would provide more accurate sputtering rates to use within the GITR simulations. the use of true to size simulation geometry with GITR would also allow for more particles to reach the target for better statistics on the impurity flux. Modeling of the Si_3N_4 helicon window with an MPEX-like limiter in place should also be performed to understand how the chosen helicon setup for MPEX will perform.

Future PMI studies on MPEX should include exposure of neutron irradiated samples to D plasma, He plasma, and mixed D/He plasma. These studies should be for retention studies to understand how bulk damage affects the amount of D and He retained during exposure as ion irradiations in previous studies only damage the near surface layer. An increased D retention may lead to evidence in certain cases which exceed the allowable T inventory of a fusion device. If the bulk neutron damage allows for He to migrate deeper into the bulk, then fewer near surface bubbles will be present for creation of W fuzz. If the neutrons only lead to increased He retention at the near surface due to the combined H/D exposure, then the rate of W fuzz formation may increase. The effect on He/D retention from transmutation elements can also be studied by comparing neutron irradiated samples to non-n-irradiated samples created with the transmutation elements added to the material. This would allow for the separation of the contributions from neutron bulk damage and transmutation elements.

Bibliography

[1] British Petroleum. BP Statistical Review of World Energy. Technical report, BP, 2018.

[2] U.S. Energy Information Administration. International Energy Outlook 2017. Technical report, EIA, 2017.

[3] R. Lindsey. Climate Change: Atmospheric Carbon Dioxide, aug 2017.

[4] T. J. Dolan. *Magnetic Fusion Technology*. Springer, 2013.

[5] ITER.org. ITER Assembly, 2018.

[6] J. M. Linke, T. Hirai, M. Rödig, and L. A. Singheiser. Performance of Plasma-Facing Materials Under Intense Thermal Loads in Tokamaks and Stellarators. *Fusion Science and Technology*, 46(1):142–151, 2004.

[7] F. Porz, G. Grathwohl, and F. Thummler. SiC as a Structural Material in the Plasma Chamber of Nuclear Fusion Reactors*. *Materials Science and Engineering*, 71:273–282, 1985.

[8] M. Shimada, D. J. Campbell, V. Mukhovatov, M. Fujiwara, N. Kirneva, K. Lackner, M. Nagami, V. D. Pustovito, N. Uckan, and J. Wesley. Chapter 1: Overview and summary. *Nucl. Fusion*, 47:S1–S17, 2007.

[9] P. C. Stangeby. *The Plasma Boundary of Magnetic Fusion Devices*. IOP Publishing, 2000.

[10] R. Behrisch, G. Federici, A. Kukushkin, and D. Reiter. Material erosion at the vessel walls of future fusion devices. *Journal of Nuclear Materials*, 313-316:388–392, 2003.

[11] Y. Ueda, K. Schmid, M. Balden, J. W. Coenen, T. Loewenholf, A. Ito, A. Hasegawa, C. Hardie, M. Porton, and M. Gilbert. Baseline high heat flux and plasma facing materials for fusion. *Nuclear Fusion*, 2017.

[12] H. Anand, J. A. Snipes, R. A. Pitts, P. C. De Vries, L. Zabeo, Y. Gribov, C. Galperti, and S. Coda. Model-based real-time power flux estimator for the ITER first wall. *Fusion Engineering and Design*, 137(July):143–151, 2018.

[13] R. A. Pitts, S. Carpentier, F. Escourbiac, T. Hirai, V. Komarov, A. S. Kukushkin, S. Lisgo, A. Loarte, M. Merola, R. Mitteau, A. R. Raffray, M. Shimada, and P. C. Stangeby. Physics Basis and Design of the ITER Plasma-Facing Components. *Journal of Nuclear Materials*, 415:S957–S964, 2011.

[14] R. A. Pitts, S. Carpentier, F. Escourbiac, T. Hirai, V. Komarov, S. Lisgo, A.S. Kukushkin, A. Loarte, M. Merola, A. Sashala Naik, R. Mitteau, M. Sugihara, B. Bazylev, and P.C. Stangeby. A Full Tungsten Divertor for ITER: Physics Issues and Design Status. *Journal of Nuclear Materials*, 438, 2013.

[15] R. A. Pitts, S. Bardin, B. Bazylev, M. A. van den Berg, P. Bunting, S. Carpentier-Chouchana, J. W. Coenen, Y. Corre, R. Dejarnac, F. Escourbiac, J. Gaspar, J. P. Gunn, T. Hirai, S. H. Hong, J. Horacek, D. Iglesias, M. Komm, K. Krieger, C. Lasnier, G. F. Matthews, T. W. Morgan, S. Panayotis, S. Pestchanyi, A. Podolnik, R. E. Nygren, D. L. Rudakov, G. De Temmerman, P. Vondracek, and J. G. Watkins. Physics conclusions in support of ITER W divertor monoblock shaping. *Nuclear Materials and Energy*, 12:60–74, 2017.

[16] G. Pintsuk, W. Kühnlein, J. Linke, and M. Rödig. Investigation of tungsten and beryllium behaviour under short transient events. *Fusion Engineering and Design*, 82:1720–1729, 2007.

[17] S. Robertson. Sheaths in laboratory and space plasmas. *Plasma Physics and Controlled Fusion*, 55(9):093001, 2013.

[18] B. Scheiner, S. D. Baalrud, B. T. Yee, M. M. Hopkins, and E. V. Barnat. Theory of the electron sheath and presheath. *Physics of Plasmas*, 22(12):123520, 2015.

[19] F. F Chen. *Introduction to plasma physics and controlled fusion*. Springer, New York, edition 3 edition, 2015.

[20] G. S Was. *Fundamentals of Radiation Materials Science*. Springer, Ann Arbor, 2nd edition, 2017.

[21] M. J. Baldwin, T. C. Lynch, R. P. Doerner, and J. H. Yu. Nanostructure formation on tungsten exposed to low-pressure rf helium plasmas: A study of ion energy threshold and early stage growth. *Journal of Nuclear Materials*, 415(1 SUPPL):104–107, 2011.

[22] P. Sigmund. Theory of Sputtering. 1. Sputtering Yields of Amorphous and Polycrystalline Targets. *Phys. Rev.*, 184(2):383–416, 1969.

[23] N. Matsunami, Y. Yamamura, Y. Itikawa, N. Itoh, Y. Kazumata, S. Miyagawa, K. Morita, R. Shimizu, and H. Tawara. Energy dependence of the ion-induced sputtering yields of monatomic solids. *Atomic Data and Nuclear Data Tables*, 31(1):1–80, 1984.

[24] H. L. Bay and J. Bohdansky. Sputtering yields for light ions as a function of angle of incidence. *Applied Physics*, 19(4):421–426, 1979.

[25] R. Behrisch and W. Eckstein. *Sputtering by Particle Bombardment*. Springer, Verlag Berlin Heidelberg, 2007.

[26] G. M. McCracken. The behaviour of surfaces under ion bombardment. *Reports on Progress in Physics*, 38(2):241–327, 1975.

[27] V. Philipps, P. Wienhold, A. Kirschner, and M. Rubel. Erosion and redeposition of wall material in controlled fusion devices. *Vacuum*, 67:399–408, 2002.

[28] N. Mellet, J. P. Gunn, B. Pégourié, Y. Marandet, C. Martin, and P. Roubin. Tungsten erosion by impurities and redeposition: focus on the magnetised sheath. *Plasma Physics and Controlled Fusion*, 59:035006–035020, 2017.

[29] M. Balden and J. Roth. Comparison of the chemical erosion of Si, C and SiC under deuterium ion bombardment. *Journal of Nuclear Materials*, 279:351–355, 2000.

[30] M. Balden and J. Roth. New weight-loss measurements of the chemical erosion yields of carbon materials under hydrogen ion bombardment. *Journal of Nuclear Materials*, 280:39–44, 2000.

[31] B. V. Mech, A. A. Haasz, and J. W. Davis. Model for the chemical erosion of graphite due to low-energy H+ and D+ impact. *Journal of Applied Physics*, 84:1655, 1998.

[32] B. V. Mech, A. A. Haasz, and J. W. Davis. Isotopic effects in hydrocarbon formation due to low-energy H +/D+ impact on graphite. *Journal of Nuclear Materials*, 255:153–164, 1998.

[33] J. Roth, A. Kirschner, W. Bohmeyer, S. Brezinsek, A. Cambe, E. Casarotto, R. Doerner, E. Gauthier, G. Federici, S. Higashijima, J. Hogan, A. Kallenbach, H. Kubo, J. M. Layet, T. Nakano, V. Philipps, A. Pospieszczyk, R. Preuss, R. Pugno, R. Ruggiéri, B. Schweer, G. Sergienko, and M. Stamp. Flux dependence of carbon erosion and implication for ITER. *Journal of Nuclear Materials*, 337-339:970–974, 2005.

[34] J. Roth, R. Preuss, W. Bohmeyer, S. Brezinsek, A. Cambe, E. Casarotto, R. Doerner, E. Gauthier, G. Federici, S. Higashijima, J. Hogan, A. Kallenbach, A. Kirschner, H. Kubo, J. M. Layet, T. Nakano, V. Philipps, A. Pospieszczyk, R. Pugno, R. Ruggiéri, B. Schweer, G. Sergienko, and M. Stamp. Flux dependence of carbon chemical erosion by deuterium ions. *Nucl. Fusion*, 44:L21–L25, 2004.

[35] J. Roth, E. Vietzke, and A. A. Haasz. Erosion of Graphite Due to Particle Impact. *Atomic and Plasma-Material Interaction Data for Fusion*, 1:65–80, 1991.

[36] E. Vietzke. Isotope Dependence of the Chemical Erosion of Graphite by Hydrogen/Deuterium Implantation. *Nuclear Science and Technology*, 39(4):363–366, 2002.

[37] R. P. H. Chang, C. C. Chang, and S. Darack. Hydrogen Plasma Etching of Semiconductors and Their Oxides. *Journal of vacuum science & technology*, 20(1):45–50, 1982.

[38] P. C. Zalm and L. J. Beckers. Sputtering of silicon nitride with hydrogen ions. *Journal of Vacuum Science & Technology B: Microelectronics and Nanometer Structures*, 2(1):84–85, 1984.

[39] J. Abrefah and D. R. Olander. Reaction of Atomic Hydrogen with Crystalline Silicon. *Surface Science*, 209:291–313, 1989.

[40] B. E. E. Kastenmeier, P. J. Matsuo, J. J. Beulens, and G. S. Oehrlein. Chemical dry etching of silicon nitride and silicon dioxide using CF 4 /O 2 /N 2 gas mixtures . *Journal of Vacuum Science & Technology A: Vacuum, Surfaces, and Films*, 14(5):2802–2813, 1996.

[41] M. I. Patino, R. P. Doerner, and G. R. Tynan. Exposure of AlN and Al2O3 to low energy D and He plasmas. *Nuclear Materials and Energy*, 23(May):100753, 2020.

[42] S. J. Ling, J. Sanny, and W. Moebs. *University Physics Volume 2*. Rice University, Houston, Texas, 2017.

[43] R. Fitzpatrick. Lecture Notes in Plasma Physics: Collision Times. https://farside.ph.utexas.edu/teaching/plasma/Plasma/node41.html, 2016.

[44] H. Frey and H. R. Khan. *Handbook of Thin-Film Technology*. Springer-Verlag, Berlin Heidelberg, 2015.

[45] R. Dux. *Impurity Transport in Tokamak Plasmas*. habilitation, University of Augsburg, 2004.

[46] B. Zohuri. *Plasma Physics and Controlled Thermonuclear Reactions Driven Fusion Energy*. Springer international, Cham, Switzerland, 2016.

[47] W. Stacey. *Fusion Plasma Physics*. Wiley- VCH, 2013.

[48] S. P. Hirshman and D. J. Sigmar. Neoclassical transport of impurities in tokamak plasmas. *Nucl. Fusion*, 21:1079, 1981.

[49] J. Rapp, L. W. Owen, J. Canik, J. D. Lore, J. F. Caneses, N. Kafle, H. Ray, and M. Showers. Radial transport modeling of high density deuterium plasmas in proto-MPEX with the B2.5-Eirene code. *Physics of Plasmas*, 26(4), 2019.

[50] J. Rapp, T. M. Biewer, T. S. Bigelow, J. B. O. Caughman, R. C. Duckworth, R. J. Ellis, D. R. Giuliano, R. H. Goulding, D. L. Hillis, R. H. Howard, T L Lessard, J.D. Lore, A. Lumsdaine, E. J. Martin, W. D. McGinnis, S. J. Meitner, L. W. Owen, H. B. Ray, and V. K. Varma. The Development of the Material Plasma Exposure Experiment. *IEEE Transactions on Plasma Science*, 44(12):3456–3464, 2016.

[51] J. Rapp, T. M. Biewer, J. Canik, J. B. O. Caughman, R. H. Goulding, D. L. Hillis, J. D. Lore, and L. W. Owen. The Development of Plasma-Material Interaction Facilities for the Future of Fusion Technology. *Fusion Science and Technology*, 64:237–244, 2013.

[52] J. Rapp, A. Lumsdaine, C. J. Beers, T. M. Biewer, T. S. Bigelow, T Boyd, J. F. Caneses, J. B. O. Caughman, R. Duckworth, R. H. Goulding, W. Hicks, C. Lau, P. Piotrowicz, D. West, and D. Youchison. The Material Plasma Exposure eXperiment: Mission and conceptual design. *Fusion Engineering and Design*, 156(February):111586, 2020.

[53] J. B. O. Caughman, R. H. Goulding, T. M. Biewer, T. S. Bigelow, I. H. Campbell, J. F. Caneses, S. J. Diem, A. Fadnek, D. T. Fehling, R. C. Isler, E. H. Martin, C. M. Parish, J. Rapp, K. Wang, C. J. Beers, D. C. Donovan, N. Kafle, H. B. Ray, G. C. Shaw, and M. A. Showers. Plasma Source Development for Fusion-Relevant Material Testing. *Journal of Vacuum Science & Technology A: Vacuum, Surfaces, and Films*, 35:03E114, 2017.

[54] J. Rapp, L. W. Owen, X. Bonnin, J. F. Caneses, J. M. Canik, C. Corr, and J. D. Lore. Transport Simulations of Linear Plasma Generators with the B2.5-Eirene and EMC3-Eirene Codes. *Journal of Nuclear Materials*, 463:510–514, 2015.

[55] J. Rapp, A. Lumsdaine, C. J. Beers, T. M. Biewer, T. S. Bigelow, J. F. Caneses, J. B.O. Caughman, R. H. Goulding, N. Kafle, C. H. Lau, E. Lindquist, P. A. Piotrowicz, H. Ray, and M. Showers. Latest Results from Proto-MPEX and the Future Plans for MPEX. *Fusion Science and Technology*, 75(7):654–663, 2019.

[56] J. F. Caneses, B. D. Blackwell, and P. Piotrowicz. Helicon antenna radiation patterns in a high-density hydrogen linear plasma device. *Physics of Plasmas*, 24:113513, 2017.

[57] Sairem. Microwave and radio-frequency professional solution. https://www.sairem.com/, 2019.

[58] T. M. Biewer and T. S. Bigelow. Observations of electron heating during 28 GHz microwave power application in proto- MPEX. *Physics of Plasmas*, 25:024501, 2018.

[59] S. J. Diem, D. L. Green, R. W. Harvey, and Y. V. Petrov. An electron Bernstein wave heating scheme for the Proto-MPEX linear device. *Physics of Plasmas*, 25:072124, 2018.

[60] T. M. Biewer, C. Lau, T. S. Bigelow, J. F. Caneses, J. B. O. Caughman, R. H. Goulding, N. Kafle, M. C. Kaufman, and J. Rapp. Utilization of O-X-B mode conversion of 28 GHz microwaves to heat core electrons in the upgraded Proto-MPEX. *Phys. Plasmas*, 26:053508, 2019.

[61] C. J. Beers, E. G. Lindquist, T. M. Biewer, J. F. Caneses, J. B. O. Caughman, R. H. Goulding, N. Kafle, H. Ray, M. A. Showers, S. J. Zinkle, and J. Rapp. Characterization of the helicon plasma flux to the target of Proto-MPEX. *Fusion Engineering and Design*, 138:282–288, 2019.

[62] C. J. Beers, R. H. Goulding, R. C. Isler, E. H. Martin, T. M. Biewer, J. F. Caneses, J. B. O. Caughman, N. Kafle, and J. Rapp. Helicon plasma ion temperature measurements and observed ion cyclotron heating in proto-MPEX. *Physics of Plasmas*, 25:013526, 2018.

[63] Lesker. Lesker/uhvd multicentre analytical stage. https://www.lesker.com/newweb/sample_manipulation/multicentre-analytical-stages-overview.cfm, 2019.

[64] Nor-Cal. Nor-cal products. https://www.n-c.com/Home.aspx, 2019.

[65] F. Bedoya, J. P. Allain, R. Kaita, C. H. Skinner, L. Buzi, and B. E. Koel. Unraveling Wall Conditioning Effects on Plasma Facing Components in NSTX-U with the Materials Analysis Particle Probe (MAPP). *Review of Scientific Instruments*, 87:11D403, 2016.

[66] C. J. Beers, C. Jaramillo, N. C. Reid, H. Schamis, J. P. Allain, J. B. O. Caughman, S. J. Meitner, J. Rapp, and S. J. Zinkle. Development of the materials analysis and particle probe for Proto-MPEX. *Review of Scientific Instruments*, 92(April):045108, 2021.

[67] J. F. Caneses and B. D. Blackwell. RF compensation of double Langmuir probes: modelling and experiment. *Plasma Sources Science and Technology*, 24(3):35024, 2015.

[68] B. Beal, L. Johnson, D. Brown, J. Blakely, and D. Bromaghim. Improved analysis techniques for cylindrical and spherical double probes. *Review of Scientific Instruments*, 83(7):073506–073510, 2012.

[69] N. Kafle. *A transport study of high density helicon plasma discharges in the Prototype Material Plasma Exposure eXperiment*. PhD thesis, University of Tennessee, 2019.

[70] N. Benjamin. High-impedance capacitive divider probe for potential measurements in plasmas. *Rev. Sci. Instrum*, 53(10):1541–1543, 1982.

[71] S. E. Savas and K. G. Donohoe. Capacitive probes for rf process plasmas. *Review of Scientific Instruments*, 60(11):3391–3395, 1989.

[72] T. M. Biewer, S. Meitner, J. Rapp, H. Ray, and G. Shaw. First results from the Thomson scattering diagnostic on proto-MPEX. *Review of Scientific Instruments*, 87:11E518, 2016.

[73] N. Kafle, T. M. Biewer, and D. C. Donovan. Dual-pass upgrade to the Thomson scattering diagnostic on the Prototype-Material Plasma Exposure eXperiment (Proto-MPEX). *Rev. Sci. Instrum*, 89:10C107, 2018.

[74] Edgertonic. Edgertronic cameras. https://edgertronic.com, 2020.

[75] M. Showers, T. M. Biewer, J. B O Caughman, D. C. Donovan, R. H. Goulding, and J. Rapp. Heat flux estimates of power balance on Proto-MPEX with IR imaging. *Review of Scientific Instruments*, 87(11):11D412, 2016.

[76] M. Showers, P. A. Piotrowicz, C. J. Beers, T. M. Biewer, J. F. Caneses, J. Canik, J. B. O. Caughman, D. C. Donovan, R. H. Goulding, A. Lumsdaine, N. Kafle, L. W. Owen, J. Rapp, and H. Ray. Power accounting of plasma discharges in the linear device Proto-MPEX. *Plasma Physics and Controlled Fusion*, 60:065001, 2018.

[77] MathWorks. Mathworks matlab. https://www.mathworks.com/products/matlab.html, 2020.

[78] J. Rapp, C. J. Beers, T. M. Biewer, T. S. Bigelow, J. F. Caneses, J. B. O. Caughman, S. J. Diem, R. H. Goulding, R. C. Isler, N. Kafle, L. W. Owen, and M. A. Showers. Operational domain of Proto-MPEX. *Fusion Engineering and Design*, 136:712–716, 2018.

[79] T. Fujimoto, S. Miyachi, and K. Sawada. New Density Diagnostic Method Based on Emission Line Intensity Ratio of Neutral Hydrogen in an Ionizing Phase Plasma. *Nucl. Fusion*, 28:1255, 1988.

[80] H. B. Ray, T. M. Biewer, D. T. Fehling, R. C. Isler, and E. A. Unterberg. Spectral survey of helium lines in a linear plasma device for use in HELIOS imaging. *Review of Scientific Instruments*, 87:11E711, 2016.

[81] A. Hermann, W. Junker, K. Gunther, S. Bosch, M. Kaufmann, J. Neuhauser, G. Pautasso, Th. Richter, and R. Schneider. Energy flux to the ASDEX-Upgrade divertor plates determined by therography and calorimetry. *Plasma Phys. Control. Fusion*, 37:17, 1995.

[82] M. A. Showers. *A Power Accounting Analysis of the Proto-MPEX Linear Device and Target Heat Flux Extrapolations to MPEX-based on Proto-MPEX discharges.* PhD thesis, University of Tenneessee, 2019.

[83] COMSOL Multiphysics® v. 5.3. www.comsol.com. COMSOL AB, Stockholm, Sweden.

[84] Mitutoyo. SJ-310 Surface Roughness Tester. https://www.mitutoyo.com, 2021.

[85] Hitachi-HighTech. Hitachi S-4800. https://www.hitachi-hightech.com/us/products/, 2021.

[86] C. D. Wagner. Sensitivity factors for XPS analysis of surface atoms. *Journal of Electron Spectroscopy and Related Phenomena*, 32(2):99–102, 1983.

[87] ThermoFisher Scientific. K-Alpha X-ray Photoelectron Spectrometer System. https://www.thermofisher.com/order/catalog/product/IQLAADGAAFFACVMAHV#/IQLAADGAAFFACVMAHV, 2021.

[88] J. R. Myra and D. A. D'Ippolito. Radio frequency sheaths in an oblique magnetic field. *Physics of Plasmas*, 22(6):062507, 2015.

[89] J. R. Myra. Physics-based parametrization of the surface impedance for radio frequency sheaths. *Physics of Plasmas*, 24:072507, 2017.

[90] H. Kohno and J. R. Myra. A finite element procedure for radio-frequency sheath-plasma interactions based on a sheath impedance model. *Computer Physics Communications*, 220:129–142, 2017.

[91] J. R. Myra and H. Kohno. Calculation of RF sheath properties from surface wave-fields: A post-processing method. *Plasma Physics and Controlled Fusion*, 61(9):95003, 2019.

[92] J. Drobny, A. Hayes, D. Curreli, and D. N. Ruzic. F-TRIDYN: A Binary Collision Approximation code for simulating ion interactions with rough surfaces. *Journal of Nuclear Materials*, 494:278–283, 2017.

[93] T. R. Younkin. *Fusion Machine Scale Wall Material Erosion and Redeposition Modeled with GITR as a Part of an Integrated Simulation to Evaluate Tungsten Plasma Facing Component Lifetimes and Feedback on Fusion Plasmas.* PhD thesis, University of Tenneessee, 2019.

[94] T. R. Younkin, D. L. Green, A. B. Simpson, and B. D. Wirth. GITR : An Accelerated Global Scale Particle Tracking Code For Wall Material Erosion and Redistribution

In Fusion Relevant Plasma-Material Interactions. *Accepted by: Computer Physics Communications*, 2021.

[95] GITR Github repository. https://github.com/ORNL-Fusion/GITR. Accessed: 2021-02-17.

[96] P. A. Piotrowicz, R. H. Goulding, J. F. Caneses, D. L. Green, J. B. O. Caughman, C. Lau, J. Rapp, and D. N. Ruzic. Computational investigation of ion cyclotron heating on Proto-MPEX. *Physics of Plasmas*, 26:33511, 2019.

[97] P. A. Piotrowicz. *Physics of the helicon antenna on the Prototye Materials Exposure eXperiment*. PhD thesis, University of Illinois at Urbana-Champaign, 2018.

[98] N. Sharma, M. Chakraborty, N. K. Neog, and M. Bandyopadhyay. Development and characterization of a helicon plasma source. *Review of Scientific Instruments*, 89:83508, 2018.

[99] P. A. Piotrowicz, J. F. Caneses, D. L. Green, R. H. Goulding, C. Lau, J. B. O. Caughman, J. Rapp, and D. N. Ruzic. Helicon normal modes in Proto-MPEX. *Plasma Sources Sci. Technol.*, 27:055016, 2018.

[100] P. A. Piotrowicz, J. F. Caneses, M. A. Showers, D. L. Green, R. H. Goulding, J. B. O. Caughman, T. M. Biewer, J. Rapp, and D. N. Ruzic. Direct measurement of the transition from edge to core power coupling in a light-ion helicon source. *Physics of Plasmas*, 25:052101, 2018.

[101] H. Kohno, J. R. Myra, and D. A. D'Ippolito. Numerical analysis of radio-frequency sheath-plasma interactions in the ion cyclotron range of frequencies. *Physics of Plasmas*, 19(1), 2012.

[102] H. Kohno, J. R. Myra, and D. A. D'Ippolito. Radio-frequency sheath-plasma interactions with magnetic field tangency points along the sheath surface. *Physics of Plasmas*, 20(8):082514, 2013.

[103] J. R. Myra, D. A. D'Ippolito, and M. J. Gerver. Faraday screen sheaths and impurity production during ion cyclotron heating. *Nucl. Fusion*, 30(5):845–858, 1990.

[104] T. R. Younkin, K. Sargsyan, T. Casey, H. Najm, J. Canik, D. L. Green, R. Doerner, D. Nishijima, M. Baldwin, J. Drobny, D. Curreli, and B. D. Wirth. Quantification of the Effect of Uncertainty On Impurity Migration in PISCES-A Simulated with GITR. *Submitted to Nucl. Fusion*, 2021.

[105] J. N. Brooks. Near-surface sputtered particle transport for an oblique incidence magnetic field plasma. *Physics of Fluids B*, 2(8):1858–1863, 1990.

[106] J. N. Brooks. Modeling of sputtering erosion/redeposition - Status and implications for fusion design. *Fusion Engineering and Design*, 60(4):515–526, 2002.

[107] R. Ding, P. C. Stangeby, D. L. Rudakov, J. D. Elder, D. Tskhakaya, W. R. Wampler, A. Kirschner, A. G. Mclean, H. Y. Guo, V. S. Chan, and P. B. Snyder. Simulation of gross and net erosion of high- Z materials in the DIII-D divertor. *Nucl. Fusion*, 56:016021, 2016.

[108] M. W. Chase Jr. Nist-janaf thermochemical tables-fourth editions, parts 1 and 2, 1998.

[109] A. W. Trivelpiece and R. W. Gould. Space charge waves in cylindrical plasma columns. *Journal of Applied Physics*, 30(11):1784–1793, 1959.

[110] A. Warren, A. Nylund, and I. Olefjord. Oxidation of Tungsten and Tungsten Carbide in Dry and Humid Atmospheres. *Int. J. of Refractory Metals & Hard Materials*, 14:345–353, 1996.

[111] P. Viegas, M. Hofmans, O. Van Rooij, A. Obrusník, B. L. M. Klarenaar, Z. Bonaventura, O. Guaitella, A. Sobota, and A. Bourdon. Interaction of an atmospheric pressure plasma jet with grounded and floating metallic targets: Simulations and experiments. *Plasma Sources Science and Technology*, 29(9), 2020.

[112] C Århammar, Annette Pietzsch, Nicolas Bock, Erik Holmström, C Moyses Araujo, Johan Gråsjö, Shuxi Zhao, Sara Green, T. Peery, Franz Hennies, Shahrad Amerioun,

Alexander Föhlish, Justine Schlappa, Thorsten Schmitt, Vladimir N. Strocov, Gunnar A. Niklasson, Duana C. Wallace, Jan-Erik Rubensson, Börje Johansson, and Rajeev Ahuja. Unveiling the complex electronic structure of amorphous metal oxides. *PNAS*, 108(16):6355–6360, 2011.

[113] M. D. Groner, F. H. Fabreguette, J. W. Elam, and S. M. George. Low-Temperature Al2O3 Atomic Layer Deposition. *Chem. Mater.*, (16):639–645, 2004.

[114] C. L. Nguyen and J. B. Metson. Differential sputtering and the formation of repeating fragments in ToF-SIMS spectra of light metal alloy surfaces. *Surf. Interface Anal.*, 45:449–452, 2013.

[115] R. Kelly and N. Q Lam. The sputtering of oxides part i: a survey of the experimental results. *Radiation Effects*, 19(1):39–48, 1973.

Appendix

A McPherson Spectrometer Calibrations

The McPherson 2051 Czerny-Turner style 1-m spectrometer uses a drop-in grating to set the resolution. To control the amount of light that enters the spectrometer and interacts with the internal gratings a tunable slit is used to maximize the collected signal while minimizing the instrument function. The slit width of 30 μm is used for all experiments. Either a 300 or an 1800 grooves/mm grating is typically used to get a viewing range of 28 nm or 3.84 nm, respectively. The resolution of the 300 grooves/mm grating is 0.055 nm while the 1800 grooves/mm grating is 0.0075 nm. The light from Proto-MPEX is collected via any 5 fiber optic lines of sight that run from Proto-MPEX to a patch panel where the 5 lines on the spectrometer can be connected. This collected light is passed via a bounce off of the gratings to spread the light into "bins" that is collected by a Princeton Instruments PhotonMAX 512b EMCCD camera. The CCD camera has a pixel array of 512x512 which has the five fibers shined across them. The horizontal pixels on the CCD represent where the light from the fibers is sent and the vertical pixels are the nm viewing location. The viewing location is selected via the Labview program McPher which controls the gears that move the grating. The horizontal pixels are binned in 5 groups of 75 pixels that are mapped over the location where the light from the grating contacts the CCD. This binning is controlled via the Princeton Instruments software WinSpec. The spectrometer with both gratings has blazing angle at 500 nm which leads to a sharp drop in signal collection at $< 400\ nm$ and $> 800\ nm$. The binned locations should be changed if looking at 400-500, 500-600, or 600-800 nm because the light on the CCD can move to overlap within a single bin. The timing for the light collection is also controlled via the WinSpec software but a timing box that sends triggers to the diagnostics on Proto-MPEX is used to synch timings. Both the timing box, which is controlled via its own Labview program, and the WinSpec need to be set up with the exposure timing and number of frames to record. The difference in their settings comes from the 2.8 ms that the CCD camera needs per frame to output data. The exposure time is set on the WinSpec software to be then 3 ms less than what is put on the timing box to account for the data read time. The frame number collected is usually for 1 second worth of data that starts before the plasma pulse and ends slightly after the pulse. The

frames are set to line up with important events within the pulse, i.e. auxiliary heating. The data is saved in a .SPE format which contains a matrix of data with a size of 5 by 512 by the number of frames. This data is stored on the Proto-MPEX server at ONRL to either be processed on the central Proto-MPEX Calcutron computer for post processing and pushing to the MDSplus tree or for individual post-processing analysis. The post-processing pushed to MDSplus is the raw data, setup conditions, the calibrated intensities, and when using Ar the ion temperatures.

The absolute calibration was performed with a Gooch and Housego white light OL455 integrating sphere calibration standard. This source comes with a calibration report for one to know the spectral radiance $[(W/(sr * cm^2 * nm))]$ versus wavelength. Scanning along the range of the McPherson with all fibers allows for the absolute calibration to be done by taking the number of counts to equal the calibration standard. The number of counts at the patch panel *vs*. at the machine can also give the transmission loss of each fiber. Most optic locations on Proto-MPEX have a polarizing film that cuts transmission by 50% but removes the sigma component of light leaving only the pi component to be collected. This method of light collecting makes fitting peaks easier.

The calibration code named MultiSpectrumAnalyzer is used in MATLAB that sets the channels to be saved as the same order of the physicals fibers that are connected to the patch panel, incorporates if the location on Proto-MPEX is using a polarizing film, performs the fiber transmission loss calculations, and converts the measured photons into their respective energies. The calibration code is on its third version with the first version being a basic wavelength vs. counts output, the second version being a rewrite of the script to include the code for ion temperature fitting, and the third version including the absolute calibrations.

B Fiber Optic Periscope Alignment

The fiber optic periscope was aligned by back-lighting the fiber with a high intensity high light. This light shines off of the fiber into Proto-MPEX. On the inner diameter of the target spool piece is a mirror that is used to bounce photons that emanate from the target into the fiber periscope. The light from back-lighting bounces off of this mirror and onto the target face. The fiber periscope can be rotated to move the light emitted to bounce off the mirror in a way that it hits the location of where the target is. This was verified first by putting a piece of paper in the vacuum vessel and seeing the light in the location where the target is. Secondly, while under vacuum the MAPP target was put into position and the light was observed again to be on the target face. The vertical alignment was done by moving the target until the light was no longer seen on the target face and then moved until the light will be on the middle of the target face. The horizontal alignment was done by moving the MAPP target inwards and first observing the light on the edge and then moving it in until the light is seen to "fall" into the target shield cut out. When this occurs the fiber periscope is aligned to look right on the target face.

C MAPP Scope of Work

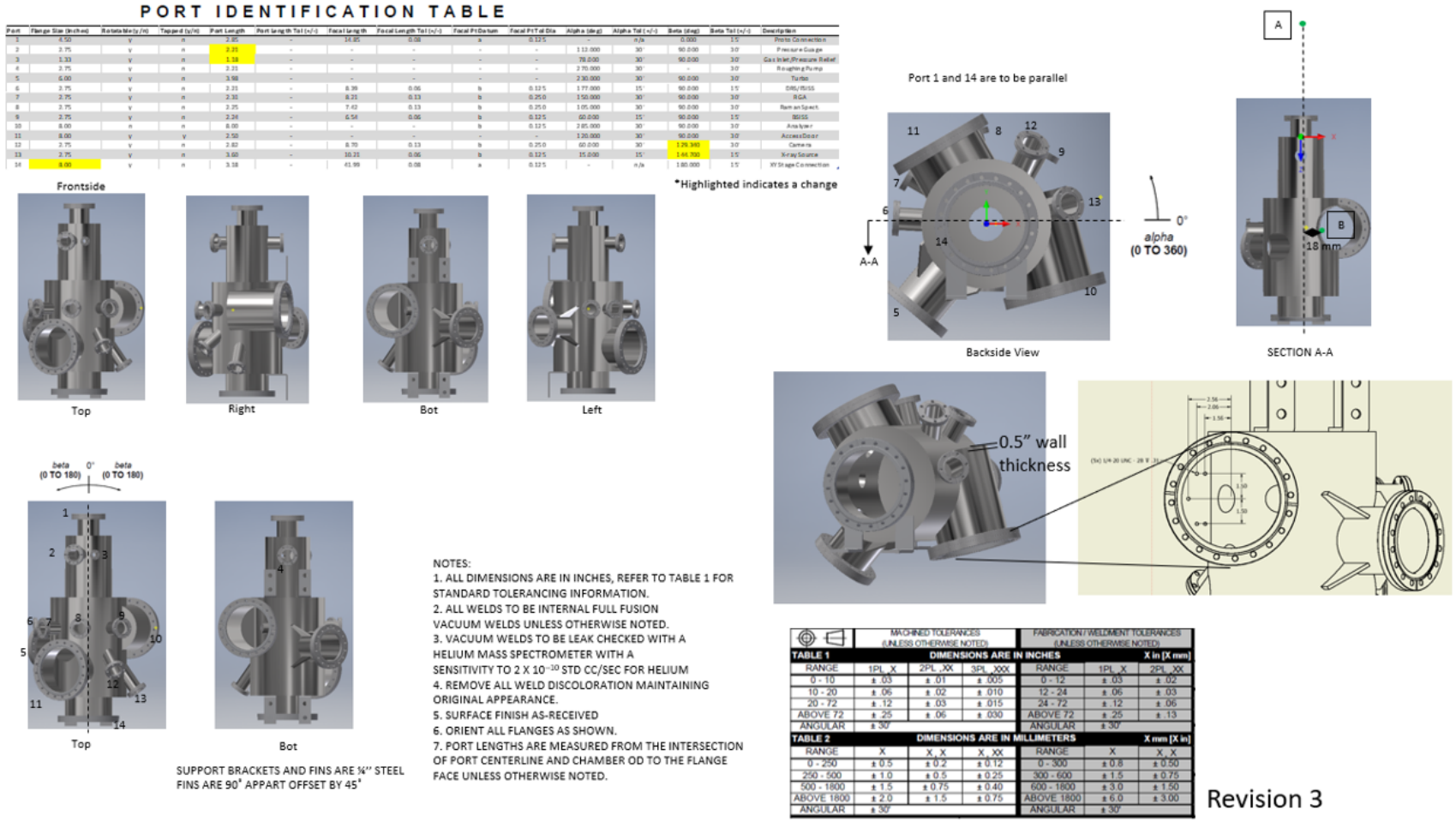


Figure 4: MAPP scope of work document designating all the angles, tolerances, and thicknesses of material to be used to construct the vacuum chamber.

D COMSOL and Sheath Model Validation

A 2D validation case from Ref. 90 Section 5.2 (referred to as Kohno 2017) has been created in COMSOL with a 0.0002 m thick dielectric layer for modeling the sheath. The domain size is x=1.2m and y=0.2m with an antenna at x=1m that is 0.05m long centered at y=0.1m. The electron density is $2x10^{18}$, the electron temperature is 15 eV, the frequency is 80 MHz, the wave vector in Z component is $k_z = 320m^{-1}$, and the antenna's surface current is a function of Kmax defined in Eq. 28 of Kohno 2017. Two values of Kmax were tested in COMSOL, $1000A/m$ and $3000A/m$. No absorbing region was implemented in this case, periodic boundary conditions were at the top and bottom of the simulation volume, a perfect electrical conductor boundary condition was applied to the left side and behind the sheath layer on the right side. The sheath layer was started at the insulating condition having $\epsilon = 1$ and $\sigma = 0$. The general boundary condition fits were used along with the fits used in this paper from Ref. 89 (referred to as Myra 2017). Note, the Kohno 2017 fits use the peak-to-peak voltage while the Myra 2017 fits use the 0-to-peak voltage. The imaginary part of the $E_{\|}$ within the simulation geometry from the Kohno 2017 work and the COMSOL results are given in Figure 5 which show good agreement in the wave absorption within the plasma. The results for the maximum $|V_{rf}|$ within the sheath equivalent layer are shown in Fig. 6 for the $1000A/m$ case while the $3000A/m$ case is shown in Fig. 7. The results from the Kohno fit show agreement, within 2%, to the Kohno 2017 data, and the Myra 2017 fits are also within 2%. The real and imaginary components of the maximum sheath impedance, $\hat{z}_{sh}$, are shown in Fig. 8 for the $1000A/m$ case and in Fig. 9 for the $3000A/m$ case. The Kohno 2017 fits match well to the Kohno 2017 data and the Myra 2017 fits are also in agreement.

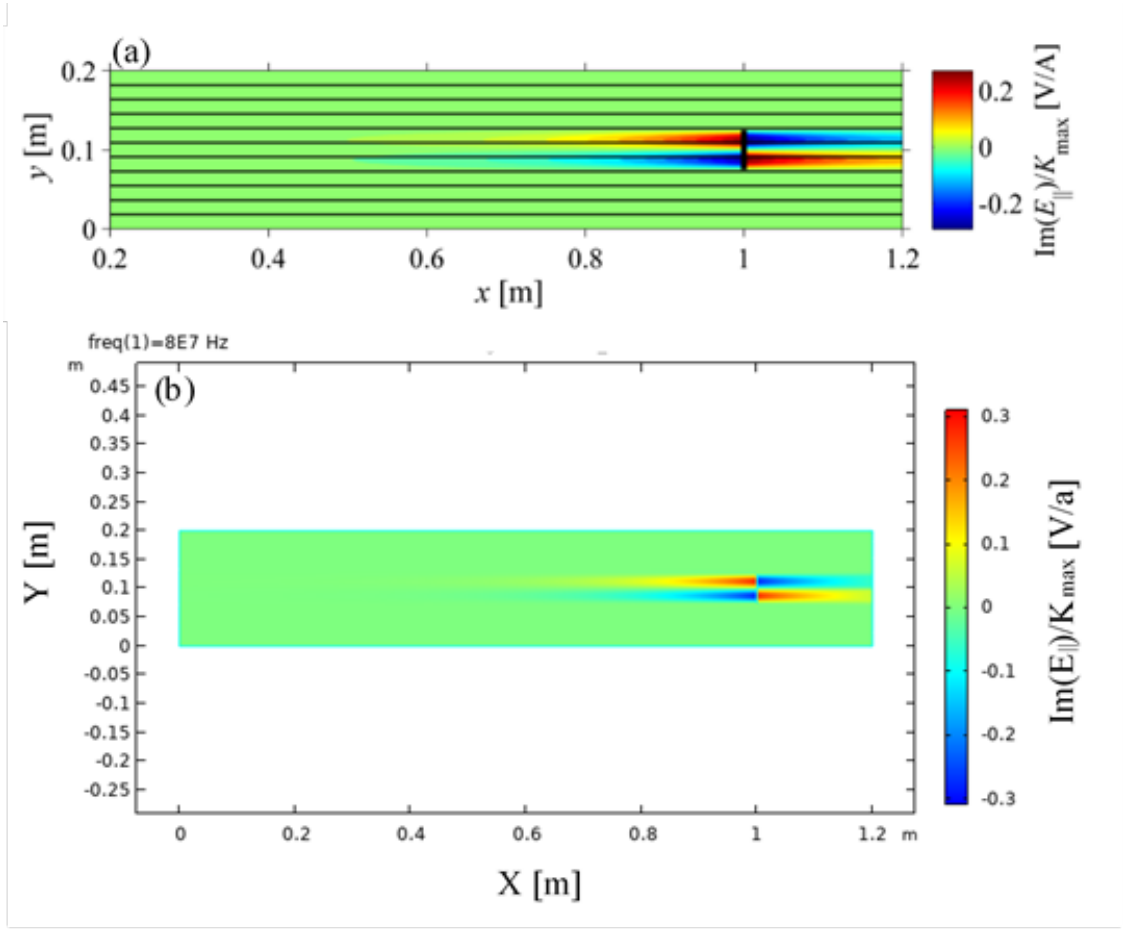


Figure 5: The $Im(E_{\|}$ plots for (a) the Kohno 2017 paper data (reproduced from [90]) and (b) the COMSOL simulation within this work.

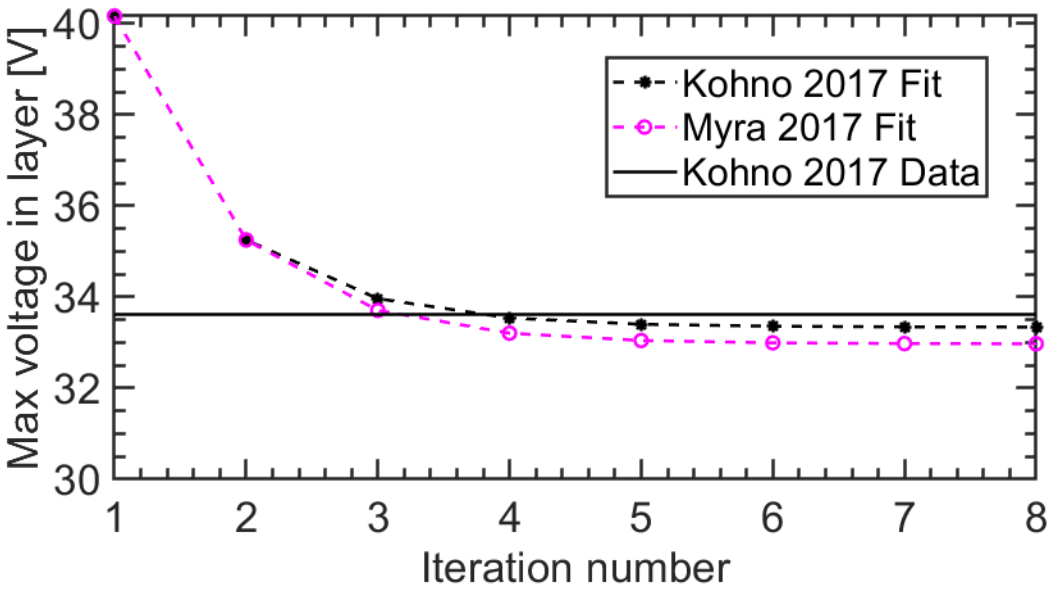


Figure 6: The maximum voltage in the layer for the $1kA/m$ case for the Kohno 2017 Fits, the Myra 2017 Fits, and the data from the Kohno 2017 work.

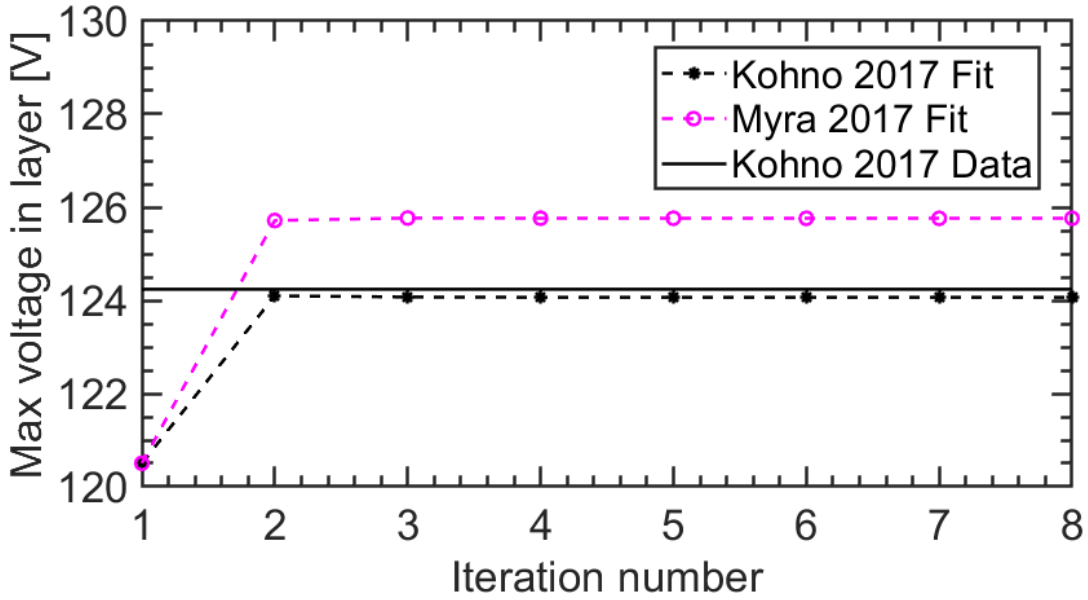


Figure 7: The maximum voltage in the layer for the $3kA/m$ case for the Kohno 2017 Fits, the Myra 2017 Fits, and the data from the Kohno 2017 work.

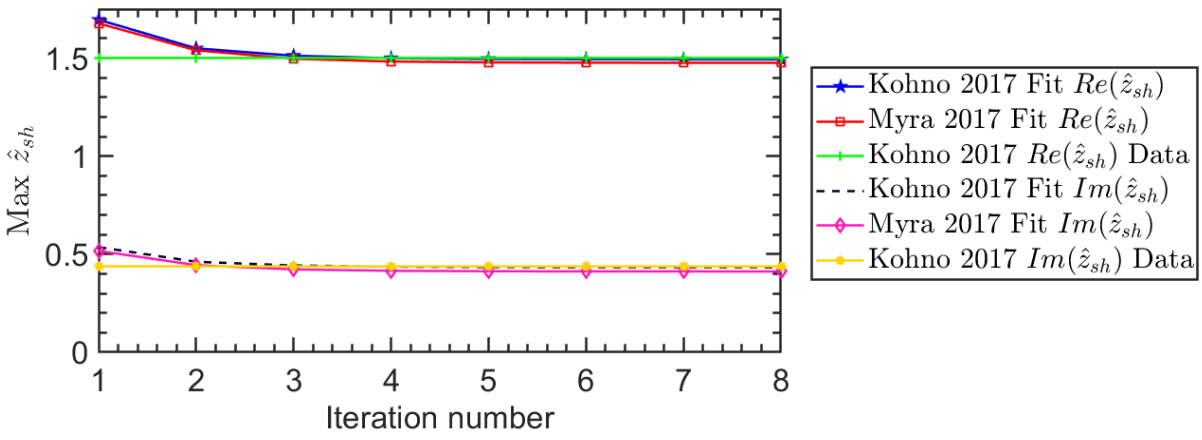


Figure 8: The maximum real and imaginary components of the sheath impedance, $\hat{z}$, in the layer for $1kA/m$ case for the Kohno 2017 Fits, the Myra 2017 Fits, and the data from the Kohno 2017 work.

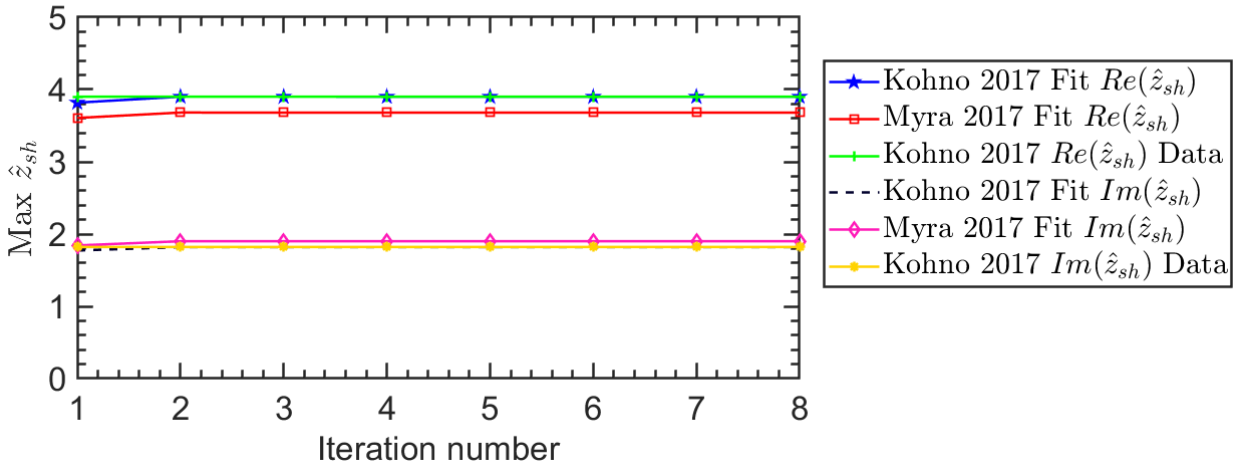


Figure 9: The maximum real and imaginary components of the sheath impedance, $\hat{z}$, in the layer for $3kA/m$ case for the Kohno 2017 Fits, the Myra 2017 Fits, and the data from the Kohno 2017 work.

Vita

Clyde Joshua Beers was born in Quincy, IL to Clyde and Sue but lived in Hannibal, Mo since he was two years old. He is the older brother to Matthew. Joshua graduated from Hannibal High School in 2010 with an interest in pursuing the nuclear science field. He went on to attend Missouri University of Science and Technology where he graduated with a Bachelors in Nuclear Engineering in 2014. He took an internship position at Idaho National Laboratory working on modeling liquid melt reactors for radioactive waste vitrification. Joshua then attended the University of Michigan where he received his Masters in Nuclear Engineering and Radiological Science in 2016 where he focused on nuclear materials. He then joined the Bredesen Center for Interdisciplinary Research and Graduate Education at the University of Tennessee for a Ph.D. in Energy Science and Engineering. Joshua has presented his work on characterization of the plasma at the target on the linear plasma device Proto-MPEX at three conferences: APS-DPP-'16, PSI-'18, and HTPD-'20. He has published papers on this topic: C. J. Beers, Phys. Plasmas. 25 (2018) 013526., C. J. Beers, Fusion Eng. Des. 138 (2019) 282–288., C. J. Beers, Rev. Sci. Instrum. 92, 045108 (2021), and C. J. Beers, Accepted by Phys. Plasmas. (2021). His dissertation work has focused on plasma material interactions and plasma impurity transport.